Development of a beam position monitor for co-propagating electron and proton beams

Eugenio Senes

Jesus College, Oxford

Thesis submitted in fulfillment of the requirements for the degree of Doctor of Philosophy at the University of Oxford

Trinity Term 2020

Abstract

Novel acceleration technologies promise a large improvement in particle accelerator performance, but pose a number of technical challenges due to the use of several beams and the beam parameters involved. To exploit these new technologies, these technical challenges need to be addressed. Innovative beam instrumentation is to be devised, to allow these acceleration experiments to become operational accelerators.

The AWAKE experiment at CERN aims to develop proton beam-driven plasma wakefield acceleration, with the aim of producing high brightness and high energy particle beams for particle physics research. At AWAKE, plasma wakefields are excited by means of a 400 GeV proton beam driver, and used to accelerate an electron witness beam. The plasma is formed by ionising a Rubidium gas with a terawatt laser pulse. The laser, electron and proton beams co-propagate in the same beampipe for metres before entering the plasma. The electron beam diagnostic is obfuscated by the presence of the more intense proton beam. Consequently, the electron beam position cannot be measured in the presence of the proton beam. To drive the acceleration efficiently, a precise positioning of the three beams is crucial. Therefore, a technique to measure the electron beam position in the presence of the stronger proton beam has to be studied.

This work addresses the beam position measurement when more than one beam is present in the beampipe. For the case of AWAKE, a technique to measure the electron-beam position exploiting the bunch-length difference with the proton beam is described. It is shown that the electron-position measurement can be carried out, provided that the detection frequency is sufficiently high. In the second part, a novel beam-position-measurement device, capable of working in the required frequency regime, is developed. Such a device is based on the emission of Cherenkov Diffraction Radiation from dielectric inserts in the beampipe. Electromagnetic simulations of the device are shown, together with the results of experimental tests on a prototype. Further developments to produce an operational instrument are discussed. The potential applications of this technology are not only in plasma-acceleration schemes, but also in any accelerator that uses short bunches, e.g. Free Electron Lasers.

Misura ciò che è misurabile,
e rendi misurabile ciò che non lo è.[1]

Galileo Galilei

Considerate la vostra semenza:
fatti non foste a viver come bruti,
ma per seguir virtute e canoscenza.[2]

Dante, *La Divina Commedia*
Canto XXVI

[1] Measure what is measurable, and make measurable what is not so.

[2] Call to mind from whence ye sprang:
Ye were not form'd to live the life of brutes,
But virtue to pursue and knowledge high.
(translation by The Rev. Henry Francis Cary, Taylor and Hessey, 1819.)

Acknowledgements

First and foremost, I would like to acknowledge Prof. Philip Burrows, for his supervision and advice during the complicated journey that culminated in this thesis work. I am also would like to thank CERN and the John Adams Institute for allowing me to work with two of the most prestigious academic institutions in the world.

During my time at CERN I had the extraordinary possibility to work on different projects learning on the field different aspects of the accelerator physics world. I had the privilege to meet and work alongside some great scientists, while being encouraged to follow and satisfy my scientific curiosity. My deepest gratitude goes to all of you.

I want to particularly thank Michal Krupa for his constant support. His guidance and supervision was vital for the development and completion of this work with its tight timeline. I also want to thank Manfred Wendt for the supervision and for transmitting his passion for the radio frequency engineering.

My gratitude goes to the Thibaut Lefevre, Stefano Mazzoni and Michele Bergamaschi, and to the colleagues of the AWAKE experiment Anna-Maria Bachmann and Patric Muggli for the discussions and support on the field work. The collaboration of the staff of the CLEAR facility was crucial for a large part of the experimental work, in particular from Antonio Gilardi, Wilfrid Farabolini and Alessandro Curcio.

I also have to thank Dr. Frank Tecker for supervising me during the first half of my doctoral studies, allowing me to study and practice beam dynamics on the field.

Last, I am grateful to my family and my friends, that sustained me and walked with me a part of this journey.

Contents

List of Figures **xiv**

List of Tables **xvi**

1 Introduction **1**

1.1 Recent developments in High Energy Physics 1
1.2 Particle colliders 3
1.3 Limitations for future colliders 4
1.4 Two-beam acceleration technologies 7
1.5 The AWAKE experiment 11
1.5.1 Particle-beam instrumentation for AWAKE 15
1.6 Motivation for this work 16

2 Detection of copropagating beams **17**

2.1 Electromagnetic field of relativistic charged particles 17
2.2 Signal generation in a capacitive BPM 19
2.2.1 Wall currents 19
2.2.2 Response of an ideal electrostatic BPM 21
2.2.3 Effect of multiple beams 23
2.3 Design parameter constraints 25
2.4 Proton beam spectrum measurement 27
2.4.1 Longitudinal beam profile measurement 28
2.4.2 Implications for the system performance 34

3 A BPM working in the quasi-optical regime **38**

3.1 Vavilov-Cherenkov Diffraction Radiation 39
3.2 A BPM prototype for in-air testing 43
3.3 Electromagnetic simulations 45
3.3.1 Simulation of a slice 47

3.3.2 3D Simulation of a single radiator 49
3.3.3 Position sensitivity 52
3.3.4 Improvements to the simulation capabilities 52
3.4 Test in air 57
3.4.1 Experimental setup 57
3.4.2 RF Schottky-diode detectors 60
3.4.3 Beam position response for single bunch beam 63
3.4.4 Response to beam position, for bunch trains 70
3.4.5 Limitations of the present setup 74
3.4.6 Directivity 78
3.5 Tests with narrow-band diagnostics 81
3.5.1 Experimental setup 81
3.5.2 RF diode linearity 83
3.5.3 Response to beam charge 84
3.5.4 Response to beam position 86
3.6 Lessons learned 87

4 Proposal for an improved design **91**
4.1 Coupling to the proton beam 91
4.2 Lower-energy beams 93
4.3 The design of a vacuum compatible radiator 94
4.4 Radiator oriented at the Cherenkov angle 97
4.5 Radiator orthogonal to the beampipe 98
4.5.1 Simulation 99
4.5.2 Experience with orthogonal waveguide coupling 102
4.6 Future developments for ChDR BPMs 103
4.7 The AWAKE ChDR BPM system 104

5 Conclusions **108**

Bibliography **110**

List of Figures

1.1 Dimension comparison of the CLIC and FCC project with the existing LHC accelerator in the Geneva area [33]. 6
1.2 ILC accelerator schematic layout [28]. 7
1.3 CLIC accelerator schematic layout [29]. 7
1.4 Schematic representation of the plasma wakefield formation by an electron driver bunch. Adapted from [48]. 9
1.5 The longitudinal and radial electric fields in a plasma bubble from the approximated solutions for linear waves in a 3D plasma. Only one quarter of the phase is useful for accelerating a particle beam without increasing its transverse size. 10
1.6 The CERN accelerator complex layout. The AWAKE proton beam is produced in the SPS (light blue ring in the centre) and extracted through the CNGS transfer line (drawn in red) to the AWAKE experiment. Adapted from [58]. 12
1.7 Layout of the AWAKE experiment [51]. The bottom left plot shows the laser, proton and electron beam at the plasma cell entrance. The adjacent plot shows the laser beam, the self-modulated proton beam and the electron beam captured by the generated wakefields. The top plot shows an example of the spectrometer images. 13

2.1 Schematic representation of the reference frames. The laboratory frame Σ and the particle rest frame Σ' are shown. 18
2.2 Schematic representation of the spatial field distribution for a charge q at rest ($\beta = 0$) and at increasing velocities. 19

2.3 Charge distribution on the beampipe walls for an ultra-relativistic beam. On the left, the case for a centred beam, while on the right the beam is displaced. The induced image charges are schematically indicated with a + sign. 20
2.4 Schematic representation of the beam interaction with a button BPM. 21
2.5 Time (on the left) and frequency domain (on the right) comparison of the parameters of the proton and electron bunches reported in Tab. 2.1. 24
2.6 Beam spectral power as function of frequency for AWAKE experiment assuming Gaussian beams. 27
2.7 Schematic representation of the setup for longitudinal profile measurement. 29
2.8 Schematic representation of the streak camera principle of operation [83]. 30
2.9 A streak camera image of the OTR light for an AWAKE proton bunch of 2.1×10^{11} protons. The vertical axis is time with one pixel being 2.2 ps. The horizontal axis is one of the transverse dimensions of the OTR light beam. The dashed yellow rectangle indicates the region of interest for beam profile calculation. . . . 31
2.10 Three examples of longitudinal proton bunch profiles measured with the streak camera together with Gaussian fits (orange lines). The plots to the left are in time domain while those to the right are their Fourier transforms. The spectrum is calculated for the raw camera image (black dots) and after increasing the frequency resolution (blue line). 32
2.11 Average beam profile (blue) in time domain (left) and its Fourier transform (right). The envelope of all recorded pulse spectra is shaded. Fits with the Gaussian and water-bag function are reported for comparison. The fit parameters are indicated in Table 2.3. 33

2.12 AWAKE electron bunch length (1 sigma) for different bunch-charge values. The measurement was carried out using the OTR screen light with the streak camera. The measurement error is its standard deviation obtained with three different processing methods. The dashed line on the left is a linear fit for charges smaller than 400 pC. The dashed line on the right indicates the mean value of the three measured points at charge larger than 500 pC [86]. 35
2.13 Comparison of spectra of the measured average proton bunch and electron bunch with different parameters. The electron bunch is assumed to follow a Gaussian longitudinal-charge distribution. 36
2.14 Ratios between the measured average proton-bunch and the electron-bunch spectra for different electron-beam parameters. The red area marks the region where the proton signal is more intense than the electron one. 36

3.1 Schematic representation of a particle passing in proximity to a flat dielectric radiator. 41
3.2 Spectrum of ChDR emission for a 100 pC 2 ps-long electron beam passing in proximity to a PTFE flat target. On the left, the emission of a 10 mm long radiator was computed at various impact parameters. On the right, the impact parameter is kept constant at 30 mm and the length of the radiator is varied. . . . 43
3.3 A longitudinal section of the test device. The beam moves in the right-to-left direction. The two components oriented at 45° and filled with the denser ruling are the PTFE inserts. 44
3.4 The test device with the extension tube installed. The beam direction is left-to-right. The white disks on the faces cut at 45° are the radiator output surfaces. Above the radiator, the fixing bolt is visible. The part of the device downstream from the radiators has a square external shape and was fitted with threaded holes to support the detection system. 44
3.5 The PTFE inserts and the RF detectors of the test device. . . . 45

3.6 Comparison of the beam electric field in vacuum close to the edge of the simulation domain for (a) the wakefield solver and (b) the PIC solver. The beam propagates left to right and the absolute value of the electric field is plotted. An electron bunch of 100 pC charge and 1 ps length is shown. In the wakefield simulation (a) the beam enters the simulation domain smoothly and the electric field is realistic already at the simulation domain boundary. The displayed frame shows the field density 20 ps into the simulation. Conversely, for the PIC simulation (b), there is some necessary time for the field to assume a realistic distribution. Picture (b) shows the field expansion process for the bunch at 2, 20, 100 and 200 ps into the simulation. A uniform meshing is used, assuring 100 GHz simulation bandwidth with 20 mesh cells per wavelength. The disturbance trailing the beam field in (b) is caused by the noise in the simulation, and can be controlled by decreasing the mesh cell size. The colour bar for the field intensity is valid for both plots. 47

3.7 Boundary conditions of the slice model. The blue ground symbol represents the magnetic boundary condition ($H_t = 0$), which is applied at both edges of the simulation domain in the y direction. The violet symbol with the four pyramids represents the open boundary condition, used in all the other boundaries. . . . 48

3.8 Electric field in the slice model at different time steps. In (a) the beam is propagating in the beampipe and has not yet interacted with the radiator. In (b) the beam is interacting with the radiator, producing the ChDR front that propagates at 45° inside the radiator. Furthermore, the DR produced by the interaction with the upstream radiator edge is visible inside the beampipe with a circular wave-front. In (c) the propagation continues after the beam passed the radiator and the ChDR front advances. After exiting the radiator (d), the field expands in vacuum as a circular wave. The formation of additional circular DR fronts due to the interaction with the radiator edges visible in (b), (c) and (d) is described later for the 3D simulation. The simulation parameters are: a simulation bandwidth of 50 GHz, 20 mesh cells per wavelength, 100 pC and 5 ps long electron beam. . . . 48

3.9 Longitudinal section of the 3D model used for the electromagnetic simulations. On the left the model is displayed including the vacuum parts and indicating the different meshing regions, on the right the vacuum volumes are hidden. Light blue volumes are made of vacuum, light green volume is the PTFE radiator, and volumes in grey are metal. The orange and blue arrows indicate the propagation path and direction of the beam. 49
3.10 3D simulation of the electric field produced by the beam passing next to a PTFE radiator with the same geometry as the one used for the tests at CLEAR. The grey and white areas represent the metal pipe. The ChDR and DR front formations are visible and are described in detail in the text. 51
3.11 On the left, the simulated 3D model is shown, including the probe point of the electric field (in red). On the right, the absolute value of the electric field at the probe point is shown for three different beam positions. Zero is the beampipe centre and the positive positions correspond to the beam getting closer to the radiator. The field is sampled in a single point, 10 mm above the centre of the radiator output surface. 53
3.12 On the left, the RMS electric field emitted from the radiator measured at the test point shown in Fig. 3.11 (a). The signal from the second radiator is deduced by geometry. On the right, the Δ/Σ quantity calculated from the simulation results for a beam displacement of ± 15 mm. The linear fit in the region of ± 3 mm displacement is also reported. 53
3.13 Flowchart of an LTI system simulation. The beam current input (left) is used to compute the electric field at a probe position (right) via the system impulse response. The passage between time and frequency domain is possible using the direct Fourier transform $\mathcal{F}$ and its inverse form. 55
3.14 Electric field components in a point of the space calculated by means of a 3D simulation (CST) and using the convolution method (LTI). In both cases, the same 100 pC 2 ps Gaussian beam profile was used to run the full CST simulation and as input of the convolution method. 56

3.15 The test device installed in the CLEAR in-air test stand. The beam exits the vacuum chamber on the left and passes through the white Integrating Current Transformer. It passes through the test device and reaches the lead and concrete beam dump on the right after hitting the small white screen. The blue cables connect the RF detectors to the signal acquisition chain. In the centre, the translation stage is visible. 58
3.16 Schematic representation of the ChDR signal detection used for the experiments. The Ka-band acquisition system used for the horizontal plane is represented on the top. The V-band acquisition for the vertical plane is drawn on the bottom. 60
3.17 An RF diode installed on the synthesizer for calibration (left) and a typical diode output signal during calibration (right). Only the region between the dashed lines is taken into account to evaluate the average voltage output. The rise and fall of the pulse are discarded, as it is not possible to assess to which extent these are determined by the diode or the synthesizer. Additional details on the response of Schottky diodes to fast transients are given in Section 3.4.5. 61
3.18 Diode response to the CW RF input produced by the synthesizer. The vertical dashed line indicates the linearity limit of 0.1 W indicated by the manufacturer. The response at different input frequencies is shown. The left plot shows the full tested range. The dashed box shows the reduced data range shown in the right plot. 62
3.19 Tested Schottky-diode average response to CW RF input from the synthesizer. The vertical dashed line delimits the linear region. The left plot shows the full tested range, while the right plot zooms on the low input power range indicated by the dashed box. The bars represent the standard error of the mean output voltage at each input power. 63
3.20 Comparison of the translation stage position range for different datasets. The ‘coarse scan’ dataset spans over the whole translation stage range of 25 mm. The displayed data were processed with method 2 (presented later). 64

3.21 The output signal of the Ka band diode detectors installed for the horizontal plane. The amplifier gain and baseline were removed. Some minor reflections due to the cable connections are visible, e.g. on channel 2 after 2.5 ns. The solid dots mark the oscilloscope sampling points. 66
3.22 Comparison of the different processing methods together with the linear fit for the 'fine scan' dataset. The fitting parameters are reported in Table 3.5. The error bars represent the standard error of the mean of the response measured at each position. . . 67
3.23 Each dataset processed with method 2 69
3.24 Comparison of the Δ/Σ sensitivity calculated for the '$100\mu m$ scan' dataset (left) and the 'fine scan' and 'fine scan low charge' (right) for the same translation stage position range. The error on the data in the 'fine scan' dataset is visibly larger than in the others due to the reduced statistics. The fit parameters are reported in Table 3.6. 69
3.25 The signal produced by the Ka band diode detectors for a train of 5 bunches. After the five peaks corresponding to the bunches spaced by 0.66 ns, a sixth smaller peak is visible at 3.8 ns. This is a smaller less intense bunch that is occasionally produced due to an imperfect setting of the CLEAR injector laser system. . . 70
3.26 'Fine scan' dataset processed by the three methods. 72
3.27 'Finest scan' dataset processed by the three methods. 72
3.28 ChDR signal from the diode detectors in the horizontal plane (top) compared to the Wall Current Monitor signal (bottom). The plots on the left show the measurements of a train of three bunches, while the plots on the right show the measurements of a train of 20 bunches. The signal level difference between both monitors is due to their design, attenuators and cables. The diode-detector signals show the emission in the Ka-band of the two PTFE radiators installed in the horizontal plane (H+ and H-). The amplifier baseline was not subtracted, and the gain is compensated. 73

3.29 Response of one of the Ka band diode detectors to a single bunch. The RF periods of 666 ps are marked. In this acquisition, a shoulder is visible after one RF period. It is generated by the second, less populated bunch trailing the first one occurring due to an imperfect setting of the laser pulse picker system. The second bunch is not always present. 74
3.30 Successive iterations of the signal leakage compensation algorithm for a five bunch train. The blue trace shows the measured signal, the red one shows the negative exponential fit and the orange one shows the signal after subtracting the fit. The dashed horizontal lines delimit the fitted region, in this case between 90% and 60% of the peak voltage. At iteration 0 (top left), the blue and orange traces are overlapped, and the first peak is used for fitting the exponential decay. In iteration 1, the exponential decay fitted on the peak of the first bunch is subtracted from the signal, allowing to measure the correct height of the second peak (orange curve). The exponential decay is then fitted again onto the second peak after the correction, and it is used to move to the next iteration. 76
3.31 Recorded signal of a Ka band RF diode generated by a beam of 80 bunches. On the left the full signal is shown, while the region in the dashed box is presented on the right. 77
3.32 On the left, the beam position sensitivity measured for the first two and 20 bunches is shown. On the right, the slope of the linear fit and the Pearson r coefficient are presented as a function of the number of bunches considered. 77
3.33 To test the directivity, the device was reversed as shown in (a). The beam is moving from left to right. The shielding copper foil connects the radiator output surfaces to the waveguide input of the detection system. Only one RF detector per plane was installed due to space constraints. The output signal of one of the RF detectors is shown in (b). The amplifier gain and baseline are compensated. 78

3.34 The absolute value of the electric field generated as the beam passes through the test device with reversed orientation. The ChDR front is generated when the beam arrives (a), but then it collides with the edge of the radiator and the metal that surrounds it (b). This results in a series of internal reflections on the metal walls, visible in (c), (d), (e). The various DR and ChDR fronts eventually exit the radiator surface with the strongest front clearly visible in (f). The results are generated with the single slice model, using the parameters: a simulation bandwidth of 50 GHz, 20 mesh cells per wavelength, 100 pC and 5 ps long electron beam. 80
3.35 The test device reinstalled in the in-air test stand on movers visible in the centre. The beam exits the accelerator, going though the white Integrating Current Transformer on the left, traversing the test device and hitting the beam dump on the right. The radiator emission is captured by a horn antenna, and sent to the detection system through a waveguide network. 82
3.36 The detection setup in the service gallery. The electromagnetic radiation arrives via the waveguide exiting the rack, then it proceeds to the rotary attenuator, finally reaching the RF diode. The signal is digitised with an oscilloscope after being amplified, if necessary. 82
3.37 Diode output voltage as a function of the input power generated from ChDR (on the left), and from the CW synthesizer (on the right). The number of bunches is indicated in the legend. . . . 83
3.38 Diode output voltage for different levels of input power. The input power for bunched beam operation was deduced by cross-calibration with the CW source in the linear operation region. . 84
3.39 Left, measured emitted power depending on the single bunch charge. The fit with the quadratic curve is shown, representing the expected dependence for coherent radiation. The emitted power is measured by attenuating the input signal on the diode by a known factor, in order to keep a constant output voltage of 1.5 mV. This procedure ensures that the diode does not change the operation regime. The measured diode output voltage (in blue) and the manual attenuation settings (in red) are reported in the plot on the right-hand side. 85

3.40 Left, measured radiated power as function of the beam position. The distance from the radiator is also reported on the top axis. An exponential fit is shown. Right, the experiment parameter for each data point. For each position, the charge (in blue), the diode output voltage (in black) and the attenuator settings (red solid line) are reported. 86
3.41 Δ/Σ response as function of the beam position, assuming that another radiator with identical response to the measured one is present on the opposite side of the device. The fit from the data in the left plot of Fig. 3.40 was used to calculate the response. The linear fit is performed on the curve in a range of ± 5 mm from the device centre. 87
3.42 Comparison of the measured beam-position sensitivity with the CST simulations. The black data points ("Data double detection") show the measured data from the 'fine' dataset processed with Method 2 (see Section 3.4.3). The 0 mm beam position corresponds to the 13 mm position setting of the translation stages. The orange line is the extrapolated sensitivity from the measurements with the narrow-band detection ("Data single detection"). The blue line is the result of the CST simulations. . . 89

4.1 Electric field computed at a probe placed 1 cm above the radiator output surface. Spectra of various beams, as reported in Table 4.1, are shown. The vertical dashed line is the cutoff frequency of an 18-mm-diameter waveguide loaded with PTFE. 92
4.2 Comparison of the electric field spectrum emitted by 1 ps- and 2 ps-long electron bunch with a charge of 100 pC. 93
4.3 Comparison of the electric field vs frequency, measured 1 cm away from the centre of the radiator output surface produced with different radiator radii in a PTFE radiator (model described in Section 3.3.2). The coloured vertical dashed lines represent the fundamental mode cutoff frequency of an equivalent PTFE-loaded waveguide of the same diameter (the numerical values are reported in Table 4.4). 95
4.4 Longitudinal section of the BPM vacuum chamber (on the left) and of the dielectric button (on the right). The beam direction is right to left. The design is preliminary. 96

4.5 (a) Simulated model overview and (b) meshing regions. The vacuum volumes in (a) are not shown. Coarse mesh size is used for the metal (3), and the vacuum regions (2 and 4). The finely meshed regions are the initial part of the beampipe (1), the radiator (6) and the vacuum above the radiator (5). For reference see Section 3.4.3. 98
4.6 Electric field 1 cm away from the radiator output surface versus frequency. The results for a radiator orientation at $71 \pm 1°$ are shown. The dashed black line marks the theoretical cutoff frequency of 19.1 GHz. 99
4.7 (a) Simulated model with the meshing regions indicated and (b) the absolute value of the electric field in the transverse plane. Minimum resolution is used for the metal (3), and the vacuum regions (2 and 4). The high quality meshing regions are the initial part of the beampipe (1), the radiator (6) and the vacuum above the radiator (5). See for reference Section 3.4.3. The simulation was produced with a bandwidth of 100 GHz, and a 100 pC and 2 ps-long electron beam. 100
4.8 Absolute value of the electric field in the radiator and in the vacuum outside the vacuum pipe (on top). The field is displayed at different times. The internal reflection of the wavefronts can be seen in (b) and (c). At the exit of the radiator, two fronts propagating in different directions are visible in (d). Due to the medium change, a part of the radiation is also sent backwards to the beampipe as shown in (f). 101
4.9 Comparison of the beam position sensitivity of radiators oriented at 71 and 90 degrees. The green line shows the linear fit, which exhibit the same response for both the orientations. . . . 101
4.10 Diode detector installed on a BPRW port. In order from the beampipe: the alumina window assembly is the grey metallic part, then a copper waveguide straight section, a green 30 dB waveguide attenuator and the Schottky diode detector. 103
4.11 Diode detector output voltage for a BPRW and a ChDR radiator. The signals are arbitrarily scaled. The figure shows the different length of the two signals. 103
4.12 A preliminary design of a vacuum-tight dielectric insert for a ChDR BPM. 104

4.13 Layout of the present AWAKE BPM systems and the proposed modifications. The proton BPMs (pBPM) are electrostatic buttons, the electron BPMs (eBPM) are shorted striplines. The proposed modifications are: ①: convert the pBPM into a ChDR BPM, ②: use the eBPM to measure also the proton position by splitting its signal, ③: install a new ChDR BPM in a drift space, ④: install a ChDR BPM in the proton beamline to measure the proton beam power in the ChDR BPM detection band. 107

List of Tables

1.1 Particles composing the fermion family. 1
1.2 Particles comprising the boson family. 2

2.1 Beam parameters used in AWAKE. 25
2.2 AWAKE parameters for this study. 26
2.3 Fit parameters for the Gaussian and water bag functions. The bunch length is estimated as σ for the Gaussian and t_b for the water-bag function. It has to be noted that the two lengths are defined differently and, therefore, are not directly comparable. . 33
2.4 Bunch-lengths obtained from measurements. 35

3.1 Parameters of the different meshing regions used in the simulations. The calculations are performed for a simulation bandwidth of 100 GHz which corresponds to a wavelength of 3 mm. . 50
3.2 Beam parameters achievable at the CLEAR facility [113]. 57
3.3 RF diode detectors specifications. 59
3.4 Parameters of the tests with a single bunch beam. The charge for the dataset '100μm low charge' was not recorded, but the settings of the preceding dataset were retained. It can therefore be assumed that the charge was between 10 and 15 pC per bunch. 64
3.5 Linear fit parameters for the three processing methods for most of the datasets. 68
3.6 Linear fit parameters for three datasets in the position range 10.5-13 mm. 70
3.7 Parameters of the tests using trains of five bunches. The error on the train charge is the standard deviation. 71
3.8 Linear fit parameters for the three processing methods applied to both datasets. 73

3.9 Linear fit parameters for Fig. 3.38. The slope is RF diode sensitivity under various test parameters. 85

4.1 Beam parameters used as baseline parameters for this study. See Table 2.2 for comparison with the AWAKE operational parameters. 92
4.2 Relativistic electron beam parameters for AWAKE and CLEAR beams. 94
4.3 Relative permittivity of the materials considered for the radiator. The different Cherenkov angles and the fundamental-mode cutoff frequency are reported. The cutoff frequency is normalised to an equivalent evacuated circular waveguide. . . . 94
4.4 Fundamental-mode cutoff frequencies for PTFE-loaded waveguides of different diameters. 95

Chapter 1

Introduction

1.1 Recent developments in High Energy Physics

The Standard Model (SM) of Particle Physics [1] is the most successful theory for describing our universe at the smallest scales. It describes natural phenomena such as interactions of particles that constitute building blocks of matter as we know it.

The subatomic particles can be organised in two families. The first is composed of fermions, particles with half-integer spin that constitute matter (Table 1.1). Two types of fermions exist: quarks (bearing a charge $+2/3$ e or $-1/3$ e, where e is the elementary charge unit), and leptons, featuring a charge of -1 e (charged leptons) or 0 (neutrinos). Furthermore fermions are also grouped in three generations with increasing mass. The second family of particles is composed of bosons, particles of integer spin that mediate the interactions between fermions (Table 1.2). The Standard Model assigns to each fermion a corresponding anti-particle, identical but featuring the opposite charge.

Matter is normally formed of first generation fermions, e.g. electrons, and compounds of quarks, e.g. protons and neutrons. The aggregates of particles

Generation	I	II	III
Quarks	Up	Charm	Top
	Down	Strange	Bottom
Leptons	Electron	Muon	Tau
	Electron neutrino	Muon neutrino	Tau neutrino

Table 1.1: Particles composing the fermion family.

Boson	Function
Photon	Electromagnetic interaction
$W^{\pm}$ and Z^0 bosons	Weak interaction
Gluon	Strong interaction
Higgs boson H^0	Higgs field mediator

Table 1.2: Particles comprising the boson family.

can be mesons (pairs of one quark and one anti-quark) or baryons (a triplet of quarks). For example, a proton is a baryon formed of two up quarks and one down quark, while a neutron is a baryon formed of one up quark up and two down quarks. More exotic combinations have been observed in recent years, e.g. at the LHCb experiment at CERN [2]–[4]. Interactions between subatomic particles are mediated by the exchange of bosons, particles of integer spin. Quarks forming baryons are held together by the strong force, mediated by gluons. They also interact via the weak force, mediated by the $W^{\pm}$ and Z^0 bosons and the electromagnetic force, mediated by photons. Charged leptons interact only via the weak and electromagnetic forces. The electromagnetic force binds nuclei and electrons, forming atoms and then molecules, shaping matter as we perceive it. Neutrinos interact only via the weak force. The final component is the Higgs field, mediated by the Higgs boson, which gives mass to all the other particles [5]. A particle associated with the Higgs field was observed in 2012 at the Large Hadron Collider (LHC) [6] by the ATLAS and CMS experiments [7], [8].

Although the Standard Model is a remarkable achievement of humanity in the understanding of particle physics, a number of questions remain unaddressed and cannot be explained with the present theory, even after the observation of the Higgs boson, e.g. a phenomenon known as neutrino oscillation, leading to the change of flavour of such a particle [9]. Furthermore, the SM does not include the gravitational force, and it does not include the dark matter and dark energy that were proposed to explain some cosmological observations [10]. Moreover, the SM does not explain why the universe is observed as predominantly made of matter, while the creation of equal amounts of matter and antimatter in the Big Bang would be expected, as the forces of nature are predominantly symmetrical between them.

To answer these and other questions, a number of theories have been developed, some of which propose new particles that have not yet been observed

in particle colliders. The search for these new particles, together with the study of the properties of the recently discovered Higgs boson, calls for a new generation of high energy particle colliders.

1.2 Particle colliders

The vast majority of the discoveries in particle physics were produced using particle beam colliders. They allow physicists to perform experiments in controlled conditions, which is much harder to achieve when observing particles in nature, e.g. observing the interaction of cosmic rays with the atmosphere from space [11] or from the ground [12]. A particle collider consists of a particle accelerator in which two particle beams are accelerated and collided with each other head-on. The products of the collisions are recorded and studied, in order to obtain an insight into the physical processes that take place. The observation rate R of a given physical process X arising from the interaction between the colliding particles is

$$R(X) = \mathscr{L}\sigma(X) \tag{1.1}$$

where $\sigma(X)$ is the cross section representing the probability of the process X happening, which includes the collision energy dependence, and $\mathscr{L}$ is the luminosity, which depends on the particle beam parameters. The luminosity can be expressed as

$$\mathscr{L} = \frac{1}{4\pi}\frac{N_1 N_2 f n_b}{\sigma_x \sigma_y} H \tag{1.2}$$

where $N_{1,2}$ is the number of particles in one of the colliding bunches, f is the collision frequency, n_b is the number of colliding bunches per cycle, σ_x and σ_y are the transverse beam dimensions, and H is a correction factor for luminosity enhancement or depression, e.g. due to beam-beam effects, non-head-on collisions, such as bunch crossing at an angle or off-centre, or the hourglass effect [13].

For a given energy, the cross section is a constant number, while the luminosity depends on the beam parameters. In order to study rare processes, i.e. those with a low cross section, it is then necessary to increase the luminosity as much as possible. The luminosity and collision energy increase are ultimately limited by numerous technical factors, which vary for each accelerator type

and are outlined in the next section.

1.3 Limitations for future colliders

Pursuing the search for particles at higher collision energies requires a new generation of particle accelerators. Particle colliders have improved over the past 60 years, reaching unprecedented levels of technical development. Devising a new generation of accelerators requires many technical limitations [14], [15] to be overcome and the exploitation of refined engineering solutions. A number of accelerator types were studied to overcome these obstacles. They are presented below together with their main limitations:

- **Circular hadron colliders:** the development of high energy circular hadron colliders is mainly limited by the required size and the availability of strong magnets. In fact, the particle momentum in a circular collider is

$$p = e\rho B \tag{1.3}$$

  where e is the elementary charge, ρ is the accelerator radius, and B is the dipole magnetic field. Consequently, an increased beam momentum (and energy) requires a larger radius or a stronger magnetic field. Presently, the LHC dipoles reach a field of 8.33 T. Stronger magnets are being designed and tested for the LHC High Luminosity Upgrade (HL-LHC) [16]. However, they have not yet demonstrated a sufficient performance to be installed in an operational accelerator [17]. If the high-field magnet technology is successful, it has been proposed to double the LHC energy in the so called High Energy LHC (HE-LHC) [18]. Additionally, the Future Circular Collider (FCC) [19] project has been proposed to increase the accelerator circumference to 80-100 km while using high-field magnets, aiming for 100 TeV collision energy.

- **Circular lepton colliders:** circular lepton accelerators not only have to obey the limitation of Equation 1.3, but they are also principally limited by the emission of synchrotron radiation. The mean power radiated by bending a particle beam trajectory into a circle is given by

$$P \propto \frac{1}{\rho^2}\frac{E^4}{m_0^4} \tag{1.4}$$

where m_0 is the rest mass of the particle and E is the particle beam energy [20], [21]. The amount of radiated power has been a massive limitation in the past, e.g. the electron beam in the 27 km LEP2 ring [22] at the top energy of 104.5 GeV lost more than 3 GeV of energy per revolution. Any equipment installed in a circular lepton accelerator must sustain constant exposure to large amounts of radiation. The use of muons instead of electrons has been proposed due to their larger mass, however muon beams are limited by their short lifetime. The production of a sufficiently intense muon beam and its acceleration to the energy required for the experiments, within the time limitations imposed by the decay, is challenging [23]. Due to the additional complications, solutions to many of the technical problems are being researched in a number of institutions [24]–[26]. As an alternative, the FCC study has proposed to install an electron-positron collider in the 100 km tunnel (FCC-ee) [27], profiting from the large ring radius to reduce the radiated power.

- **Linear electron colliders:** the particle momentum in a linear collider is

$$p \propto L\, G_{\mathrm{acc}}$$

where L is the total accelerating length and G_{acc} is the accelerating gradient per unit length. Many designs have been proposed for linear electron-positron colliders, ranging from more traditional to the most exotic technologies. The International Linear Collider (ILC) [28] proposed an accelerator based on superconducting radiofrequency (RF) cavities. The Compact Linear Collider (CLIC) [29] is based on normal-conducting high-gradient RF technology and a novel two-beam acceleration scheme in order to reach a high beam energy while minimising the accelerator length. Ultimately, any acceleration technology relying on RF cavities is limited by the surface electrical breakdown [30]. To overcome this limitation, a number of innovative techniques relying on plasma are under study. So far none of them appear credible for an operational collider due to the required high beam brightness [31], even though record accelerating gradients were reached [32]. Innovative acceleration techniques are reviewed in Section 1.4.

The footprint of the CLIC and FCC projects compared to the existing LHC is shown in Fig. 1.1. LEP2 and the LHC were designed to fit in the same

27 km long tunnel, as well as the HL-LHC and HE-LHC projects. Regarding linear colliders, both the ILC (see Fig. 1.2) and CLIC project (see Fig. 1.3) foresee long footprints of the order of 50 km length for the top energy versions, although shorter designs are considered for the lower energy versions.

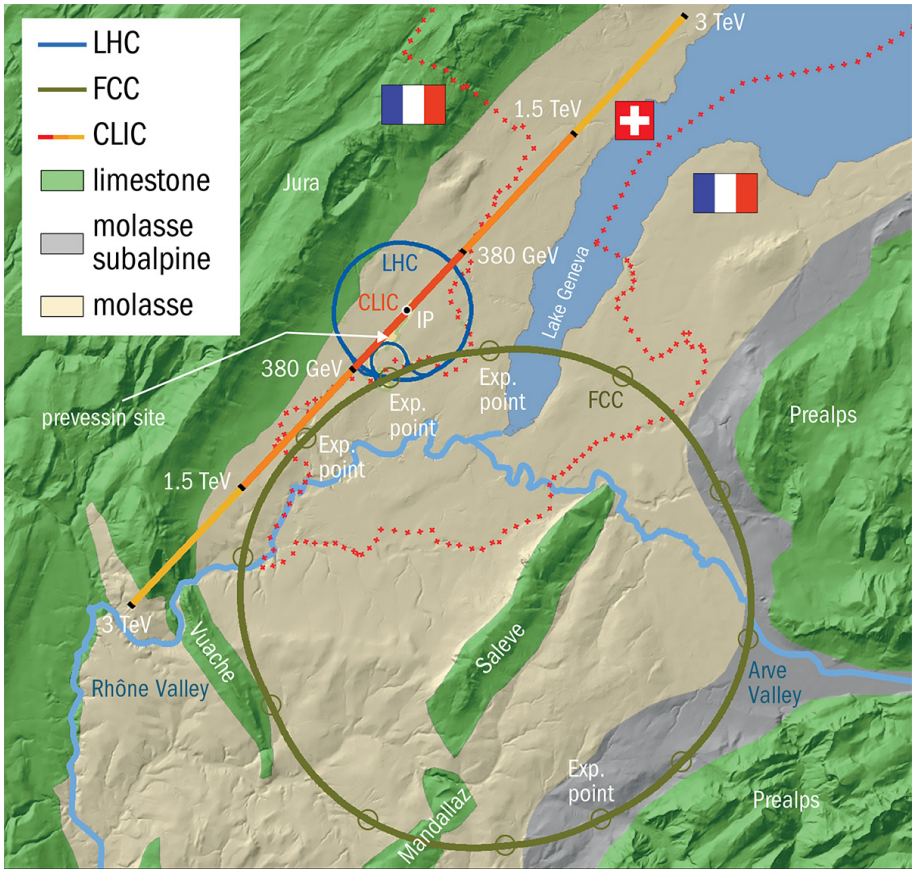

Figure 1.1: Dimension comparison of the CLIC and FCC project with the existing LHC accelerator in the Geneva area [33].

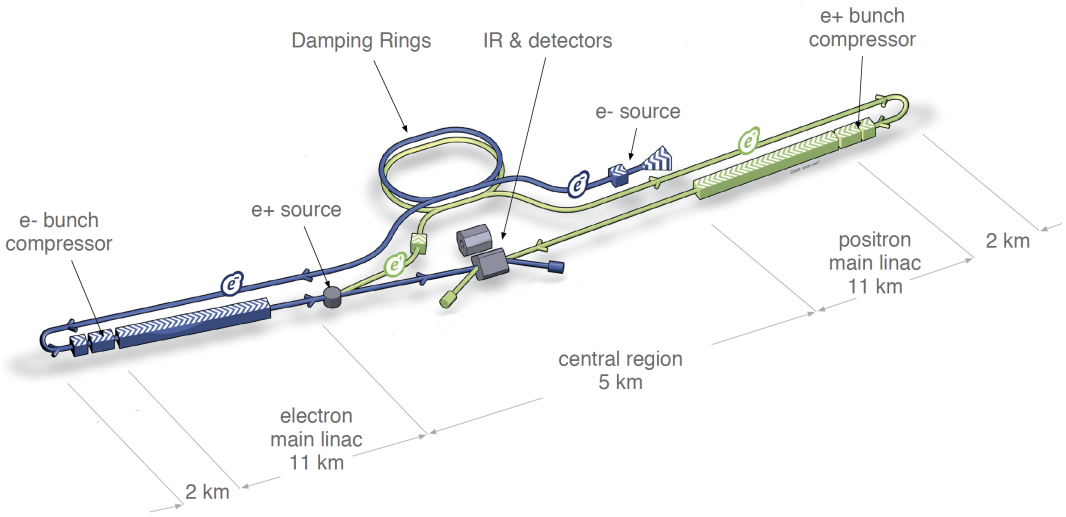

Figure 1.2: ILC accelerator schematic layout [28].

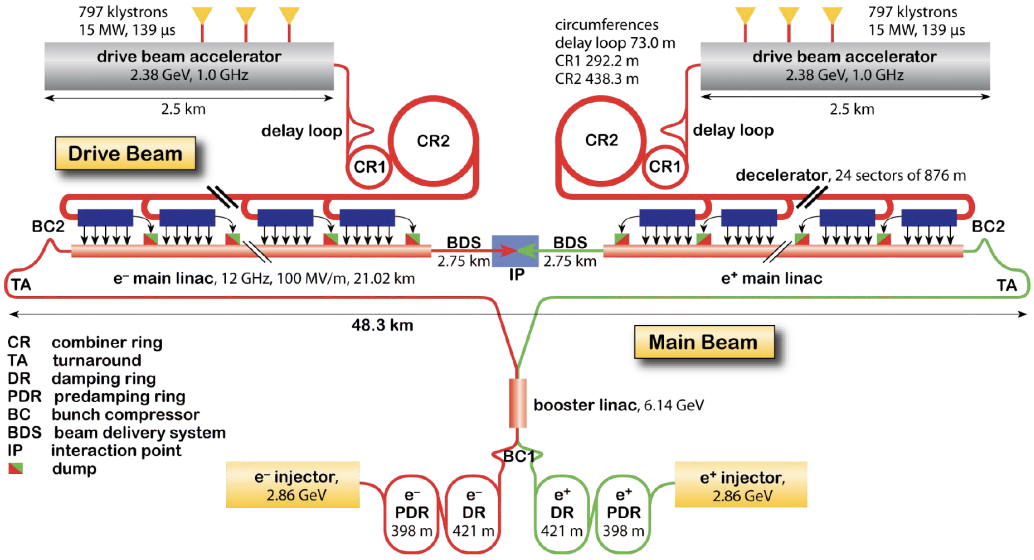

Figure 1.3: CLIC accelerator schematic layout [29].

1.4 Two-beam acceleration technologies

RF cavities have been the workhorse of modern accelerators. The RF power is traditionally produced starting from an electrical signal and amplified, usually in the final stage with klystrons. Then it is injected into resonant cavities with an appropriate phase to accelerate the beam once it passes through the cavity [34]. The use of RF-based technology is ultimately limited by breakdowns, due to the high surface electric field in the equipment [30]. In recent years, in an attempt to improve performance and energy efficiency, novel techniques have been studied to supply fast pulses of high power to the beam. Their common

denominator is abandoning the conventional RF production and instead feeding accelerating structures with energy extracted from another beam. The new schemes work like an electrical transformer, where a 'drive', high power, beam is depleted of energy, that is transferred to a 'witness' beam that is accelerated. An advantage of this approach is the possibility to store a large amount of energy in the drive beam before eventually transferring it to the witness. The drive beam can be either a photon beam (i.e. a high power laser) or a charged particle beam.

The two-beam acceleration concept for a linear collider was already proposed in the past by the CLIC study [35] with the drive beam power extracted in the form of RF and transferred to a second parallel accelerator to accelerate the witness 'main' beam. The proof of feasibility of two-beam acceleration has been demonstrated in the CTF3 facilty at CERN [36]. Nevertheless, CLIC remains limited by the breakdowns occurring in its normal-conducting accelerating cavities. This effect is limited with careful design and surface treatment to reduce the surface electric field, allowing accelerating gradients in excess of 100 MV/m to be achieved [37], [38].

To overcome the breakdown limitation of metals and further increase the accelerating gradients, two different approaches are being studied: dielectric accelerating structures, and acceleration in plasmas. Both work with an accelerating field frequency much higher than the typical RF, usually exceeding hundreds of GHz for dielectric structures and in the THz range for plasma acceleration.

The proposed accelerating structures made of dielectric materials can be both particle beam driven [39] and laser driven [40]. These technologies already demonstrated accelerating gradients 2-3 times larger than the most efficient metal cavities [41] ultimately exceeding GV/m [42].

Even higher accelerating gradients are possible when using an already 'broken-down' medium, e.g. plasma [43], [44] in a scheme known as Plasma Wakefield Acceleration (PWA), with the drive beam traversing a plasma column. The neutral plasma density is locally perturbed as the drive beam passage displaces some of the plasma electrons, generating regions with high electric field. This can be achieved by exploiting the ponderomotive force of a laser beam pulse on the plasma electrons (Laser Wakefield Acceleration, LWFA) [45], [46] or by using the space-charge force from a relativistic particle beam (Particle Wakefield Acceleration, PWFA) [32], [47]. This process is schematically shown in Fig. 1.4, where the electron drive bunch has generated a plasma

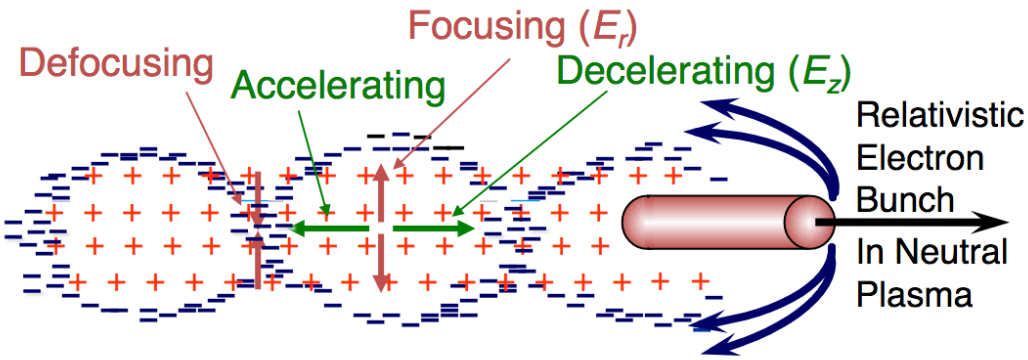

Figure 1.4: Schematic representation of the plasma wakefield formation by an electron driver bunch. Adapted from [48].

'bubble' in which the electron density is reduced.

The plasma density perturbation depends on the drive beam intensity, resulting in different plasma wave regimes. For small driver intensities, linear plasma density waves will occur, which is known as the linear regime. Nonlinear waves of growing amplitude arise with an increasing driver intensity, up to reaching the blow-out or 'bubbling' regime in which the plasma electrons trailing the driver are completely expelled from the bubble and form a sheath on the bubble edge. In order to characterise the plasma wave regime, two figures of merit are defined for LWFA and PWFA respectively:

$$a_0 = \frac{eE_0\lambda_0}{2\pi m_e c^2} \qquad \Lambda_0 = \frac{n_b}{n_0} k_p^2 \sigma_r^2 \tag{1.5}$$

where, a_0 is the normalised field strength, E_0 and λ_0 are the laser electric field intensity and wavelength, m_e is the electron mass and c is the speed of light in vacuum. For PWFA, Λ_0 is the normalised beam charge per unit length [49], n_b and n_0 are the driver bunch and plasma densities, σ_r is the driver transverse size and k_p is the plasma wave number. The latter is given by the relation $k_p = w_p/c$, where the plasma frequency is defined as $\omega_p = \sqrt{\frac{n_0 e^2}{m_e \epsilon_0}}$ and ϵ_0 is the vacuum permittivity. The linear regime occurs when the normalised intensity a_0 or Λ_0 are less than 1 (ideally $\ll 1$).

An analytical description of the electric field can be derived for a 3D non-relativistic plasma in the the linear regime [50]. The longitudinal and transverse electric field are given by:

$$E_z \simeq -A\left(1 - \frac{r^2}{a^2}\right) cos\left(k_p z - \omega_p t\right), \qquad r \ll a \tag{1.6}$$

$$E_r \simeq 2A\left(\frac{r}{k_p a^2}\right) sin\left(k_p z - \omega_p t\right) , \qquad r \ll a \tag{1.7}$$

where r and z are the radial and longitudinal coordinates, a is the driver radius, ω_p and k_p are the plasma frequency and wave number and t is the time variable. These expressions hold under the assumptions that $k_p a \gg 1$ and $r \ll a$. The A factor is defined for LWFA and PWFA as

$$A_{\text{LWFA}} = \frac{\omega_p r k_p e E_0^2}{8\omega^2 m_e} \quad , \qquad A_{\text{PWFA}} = \frac{8eN}{a^2} \tag{1.8}$$

where N is the number of particles in the PWFA driver, ω is the laser frequency and E_0 is the laser electrical field. Equations 1.6 and 1.7 show that there is a $\pi/2$ phase difference between the longitudinal (accelerating or decelerating) and the transverse (focusing or defocusing) electric fields. Therefore, only one quarter of the wake period can be used to accelerate the witness beam while simultaneously focusing it, as shown in Fig. 1.5.

An electron beam injected into a proper region of the plasma bubble will be therefore accelerated and focused respectively by the longitudinal and transverse electric field. Acceleration of externally-injected electron beams has been experimentally achieved driven by both electron [47] and proton beams [51].

The maximum achievable accelerating gradient in a plasma accelerator is

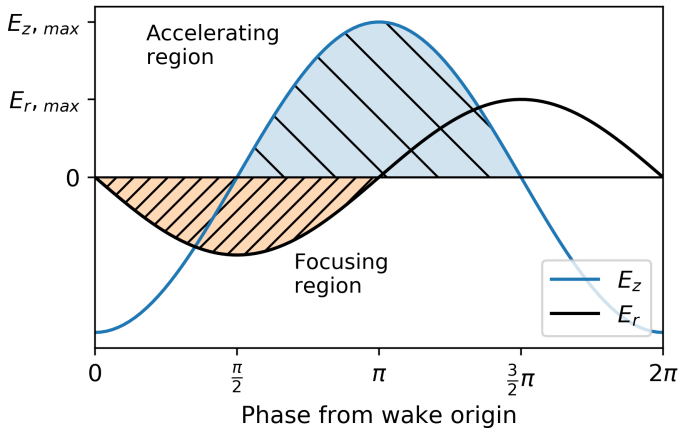

Figure 1.5: The longitudinal and radial electric fields in a plasma bubble from the approximated solutions for linear waves in a 3D plasma. Only one quarter of the phase is useful for accelerating a particle beam without increasing its transverse size.

given by the cold nonrelativistic wavebreaking field

$$E_z = \frac{m_e c^2}{\epsilon_0}\sqrt{n_e} \approx 96\sqrt{n_0} \tag{1.9}$$

where n_0 is the plasma density in cm^{-3} [44], [52]. As plasma densities of the order of 10^{18} cm^{-3} are achievable, accelerating gradients of 100's GV/m become within reach [32], [53], three orders of magnitude higher than the best RF cavities.

Plasma wakefield acceleration is particularly challenging not only due to the inherent complexity of the setup, but also because of the stringent beam parameters required. In fact, the bunch length σ_z [49] and the transverse size σ_r [54] must satisfy the following conditions to efficiently drive plasma wakefields while avoiding development of any instabilities:

$$k_p \sigma_z \sim \sqrt{2} \tag{1.10}$$

$$k_p \sigma_r \sim 1 \tag{1.11}$$

Considering a plasma density between 10^{14} and 10^{18} cm^{-3}, these conditions translate to a required transverse size range between 0.75 mm and 7.5 μm, respectively, and a bunch length between 0.5 mm and 5 μm. As high plasma densities are desirable due to the higher achievable accelerating gradient (see Equation 1.9), one can see how challenging beam focusing is and the required beam positioning accuracy needed for these experiments.

1.5 The AWAKE experiment

The Advanced Wakefield Experiment (AWAKE) at CERN studies plasma wakefield acceleration driven by a high energy proton beam, and demonstrated acceleration of an electron bunch in 2018 [51]. To achieve acceleration, a proton drive bunch is merged in a common beamline with a laser beam and an electron bunch [55]. They then propagate to a plasma cell, where the PWFA takes place. The experiment layout is presented in Fig. 1.7.

The 400 GeV proton driver bunch is produced in the CERN accelerator chain, shown in Fig. 1.6. The proton beam is initially produced in Linac 2 and accelerated up to an energy of 50 MeV. The beam is then transferred to

the Proton Synchtron Booster (PSB), and it is accelerated up to 1.4 GeV. At this point, it is extracted to the Proton Synchrotron (PS), and once the energy of 26 GeV is reached, the beam is sent to the Super Proton Synchrotron (SPS). In the SPS the beam is accelerated to 400 GeV. It is then extracted through the CNGS extraction line, that reaches the AWAKE experiment after $\sim$ 1 km [56]. Currently, a substantial upgrade of the CERN injector chain is being realised [57], affecting mostly Linac 2, PSB and PS. This upgrade does not impact the AWAKE proton beam production, as no modification in the proton beam parameters is expected at the moment. The proton bunch has a bunch length of 6-12 cm, with a bunch population that can be selected in the range $1 - 3 \times 10^{11}$ protons per bunch (ppb), and it is focused down to an r.m.s. transverse size of $\sim 200\,\mu$m at the plasma cell entrance [51].

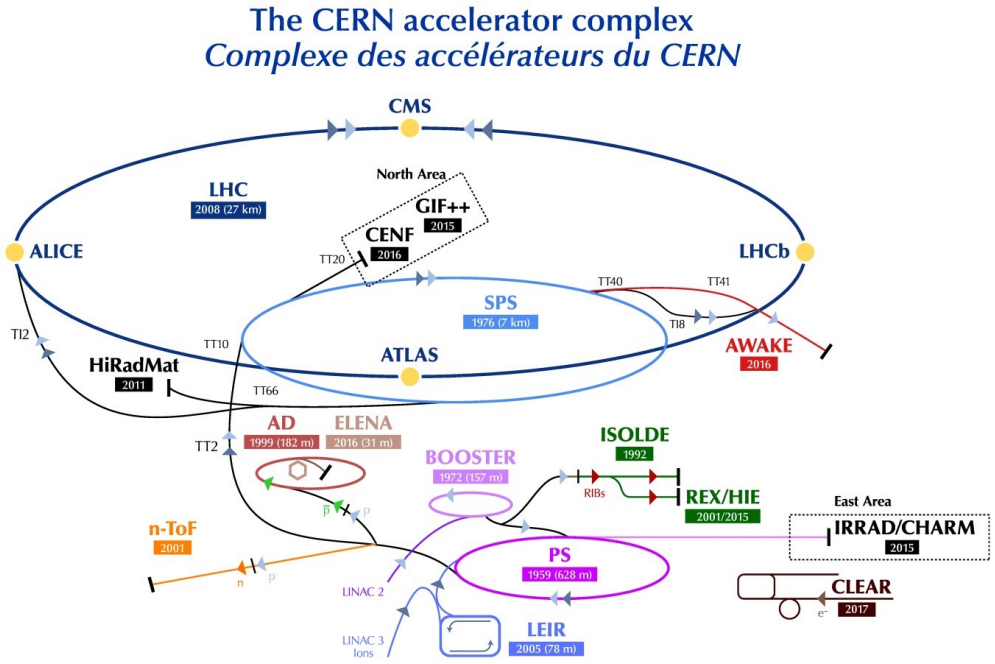

Figure 1.6: The CERN accelerator complex layout. The AWAKE proton beam is produced in the SPS (light blue ring in the centre) and extracted through the CNGS transfer line (drawn in red) to the AWAKE experiment. Adapted from [58].

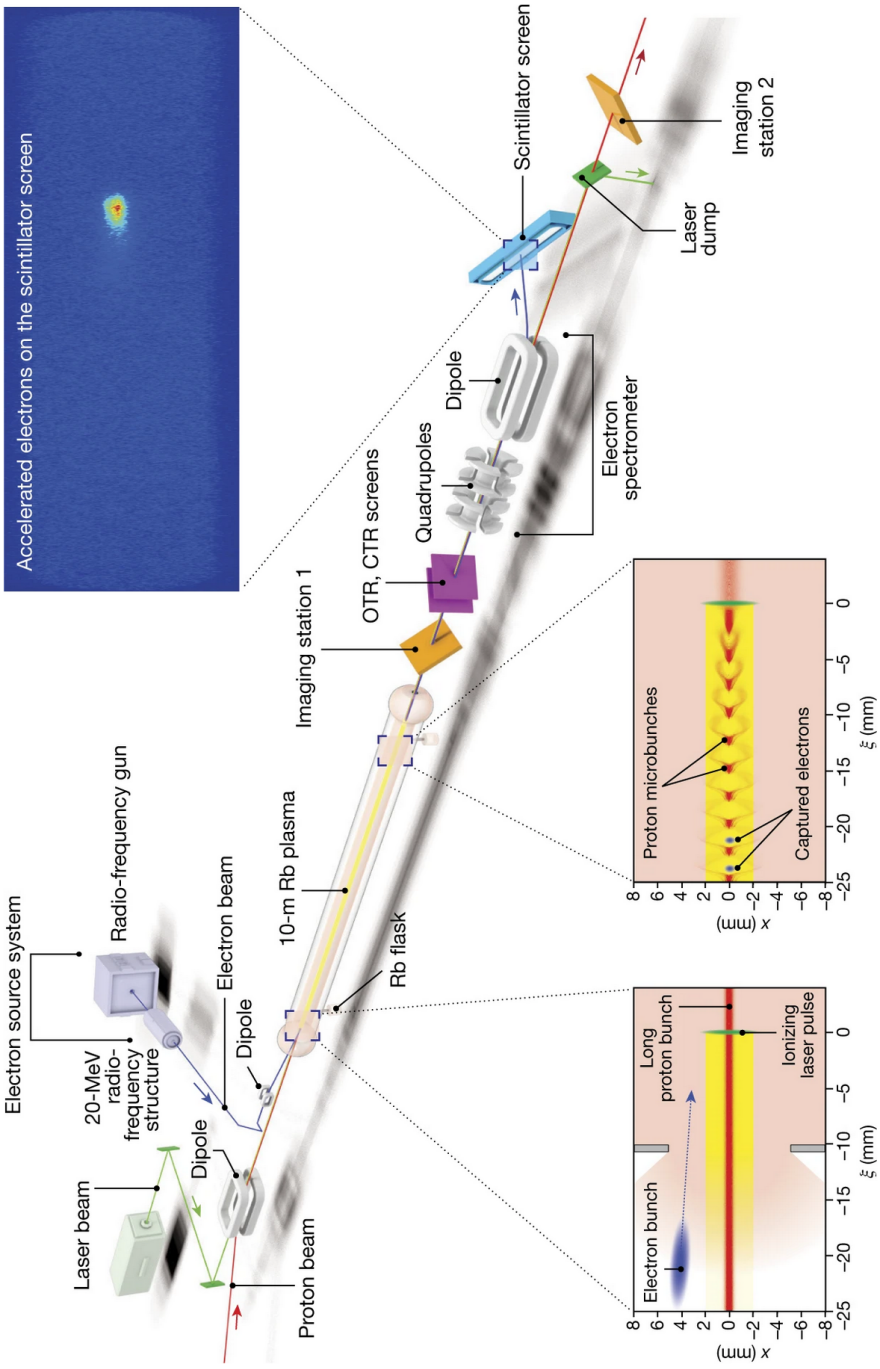

Figure 1.7: Layout of the AWAKE experiment [51]. The bottom left plot shows the laser, proton and electron beam at the plasma cell entrance. The adjacent plot shows the laser beam, the self-modulated proton beam and the electron beam captured by the generated wakefields. The top plot shows an example of the spectrometer images.

The laser beam is used to ionise the rubidium (Rb) gas present in the plasma cell, resulting in the formation of a plasma column. AWAKE uses a 120 fs-long laser pulse with a wavelength of 780 nm and pulse power up to 450 mJ [59]. The laser beam is transversely focused to 1 mm (full-width at half-maximum, FWHM) inside the plasma cell.

The electron witness beam is produced in a dedicated photoinjector close to the experiment. Its energy can be selected in the range of $10-20$ MeV with a $0.1-1$ nC charge and a bunch length of $1-4$ ps (1σ) [60], [61].

The plasma cell is 10 m long and has a 4 cm diameter. Two rubidium flasks are installed at each end and the Rb gas density is controlled in the range $10^{14}-10^{15}$ cm^{-3} by adjusting the cell temperature [62].

To successfully drive wakefields to accelerate electrons, a proton bunch shorter than that produced in the SPS is necessary. In fact, directly using the SPS proton beam as a driver would require the use of a low plasma density, that results in a modest accelerating gradient below 10 MV/m [63]. To overcome this problem, the experiment works in two steps: in the first part of the plasma cell, the proton bunch is fragmented into a train of shorter bunches by a process called Seeded Self Modulation (SSM) [64]. For a relativistic proton bunch [65] it is achieved by co-linear steering of the laser pulse and the proton bunch (see the inset in the bottom left of Fig. 1.7). The laser ionises the Rb vapour into plasma by creating a sharp ionisation front. The transverse wakefields induced in the plasma determine a periodic focusing and defocusing of the proton beam, where the period length is determined by the plasma parameters. The protons in the defocusing regions are consequently expelled, transforming the proton bunch in a train of micro-bunches serpared by one plasma wavelength (see the inset in the center bottom of Fig. 1.7). The micro-bunch train resonantly drives large amplitude wakefields in the plasma. The modulation of the proton bunch into more than 20 micro-bunches has been demonstrated at AWAKE [66]. The electron bunch is then inserted into the appropriate point in the train of micro-bunches and accelerated. It does not participate in the SSM process, as it is injected with a spatial offset and a temporal delay. The electron and proton beams are overlapped a few metres downstream from the plasma cell entrance, after the SSM process has taken place. The generated wakefields are suitable to accelerate the electron beam if it is placed at the correct longitudinal position in the wakefields. Selection of the relative delay between the beams and the beam trajectories is crucial for achieving acceleration. Boosting electrons from 18.8 MeV up to an energy of

2 GeV in a 10 m plasma cell has been demonstrated [51].

1.5.1 Particle-beam instrumentation for AWAKE

Given the remarkable complexity of the AWAKE facility, a large amount of particle-beam instrumentation is necessary to operate and diagnose the multiple beamlines. Various measurements are performed on the beams, including electron and proton beam positions, transverse profiles, temporal synchronisation between the beams, charge measurements, and an energy measurement of the electron beam. The systems most relevant for the work presented in this thesis are briefly described below, while a detailed description of the AWAKE particle-beam instrumentation can be found in [67], [68].

The transverse beam profile is measured with removable screens that can be inserted into the beamline. Two types of screens are used, based on scintillation [69] and Optical Transition Radiation (OTR) [70]. Chromox scintillating screens (Al_2O_3:CrO_2) are used for the profile measurements due to their high light yield, but feature a long decay time (>100 ms). Silver-coated Silicon OTR screens can also be used for the beam profile measurement, but they have a more modest light yield. The advantage of OTR screens is the instantaneous emission, that is used for beam synchronisation purposes. The two types of screens offer a comparable spatial resolution. A total of six screen imaging stations are present in AWAKE, two of them in the electron beamline, two in the common beamline upstream of the plasma cell, and two in the common beamline after the plasma cell. The beam profile in the common line can be measured with a resolution of 50μm.

The temporal synchronisation between the beams is measured using the OTR light emitted by one of the screens. The light is then sent through an optical line to a separate room where a streak camera with a temporal resolution of 200 fs is installed. This setup can also be used to measure the longitudinal profile of the beams. Such a measurement was performed during this thesis work, therefore the detailed description of the system is presented later in Section 2.4.1.

The transverse beam position is monitored with separate systems for the proton and electron beams upstream of the plasma cell. The proton Beam Position Monitors (BPMs) are placed along the whole transfer line starting from the SPS and extend beyond the plasma cell to the proton beam dump. The system is composed of 21 sensors formed of four electrostatic buttons.

Laboratory and beam-based tests showed a 40 μm resolution for high intensity beams $> 10^{11}$ ppb [71]. The electron BPM system is made of shorted stripline BPMs [72], [73]. Five of them are installed in the common beamline, while seven are installed in the electron beamline. In laboratory and beam-based tests they exhibited a resolution below 10 μm.

1.6 Motivation for this work

A number of novel techniques showed both theoretically and experimentally that unprecedented accelerating gradients can be achieved. To turn these experiments into future operational accelerators, development of novel beam instrumentation and diagnostic techniques is necessary. The existing technology is challenged by two major issues: novel acceleration schemes often involve more than one beam, and they require extremely precise and accurate instruments due to small beam sizes and short pulse lengths. These problems apply not only to plasma-based accelerators, whose strict requirements on the beam size are outlined in Equations 1.10 and 1.11, but also to more traditional designs. For example, the CLIC facility would require measurements of the transverse position of beams to the nanometre level in its final-focus system.

This thesis work contributes to the field of novel beam instrumentation for facilities using multiple particle beams. The presented research addresses the problem of detecting the position of a shorter and less intense electron witness bunch in AWAKE, when a longer and more intense proton driver bunch is co-propagating in the beam pipe. Currently, the electron BPM system is not capable of measuring the electron beam position when the proton beam is present. The developed techniques are also valid for all accelerators that use short bunches, of the order of ps-long or shorter, e.g. Free Electron Lasers (FELs).

Chapter 2

Detection of copropagating beams

2.1 Electromagnetic field of relativistic charged particles

Relativistic effects induce substantial modifications to the electromagnetic field radiated by charged particles. It is therefore necessary to understand how the field distribution is modified when it is observed in different reference frames.

Consider two inertial reference frames to study the field of a charged particle in uniform motion. In the rest frame Σ', the particle velocity is zero. The electric field of the particle is isotropic, and the field magnitude is expressed as

$$E(r) = \frac{1}{4\pi\epsilon_0}\frac{q}{r^2} \tag{2.1}$$

where q is the particle's electric charge, r is the distance between the observation point and the particle and ϵ_0 is the dielectric constant of vacuum.

The laboratory frame Σ sees the particle and the rest frame in motion with a relative velocity $v = \beta c$, where β is the particle speed in units of the speed of light in vacuum c. The Lorentz factor is defined as

$$\gamma = \frac{1}{\sqrt{1-\beta^2}} \tag{2.2}$$

where $\gamma = 1$ corresponds to zero velocity and $\gamma \to \infty$ as the velocity approaches the speed of light.

Figure 2.1 shows a schematic representation of the two reference frames. The charge q is placed in the origin O' of the rest reference frame Σ'. The distances between the field observation point P and the origins of rest and

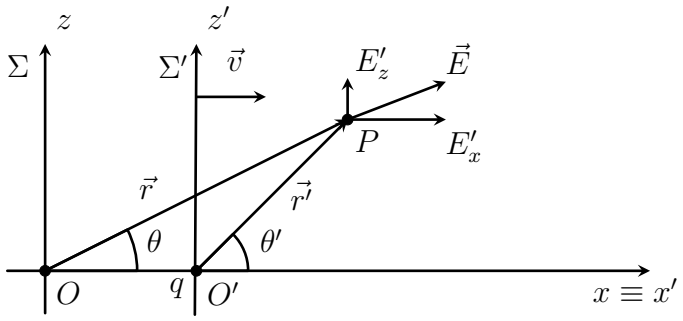

Figure 2.1: Schematic representation of the reference frames. The laboratory frame Σ and the particle rest frame Σ' are shown.

laboratory reference frames are indicated with $\vec{r}$ and $\vec{r'}$, respectively.

For a relativistic motion in the x direction, there is a time t_0 when the particle is at the origin O, and the origins of the reference frames Σ and Σ' coincide. The electric field in the observation point P, when observed from the origin of the laboratory frame Σ is expressed as [74]:

$$E\left(\theta\right) = \frac{q}{r^2\gamma^2}\frac{1}{\left(1-\beta^2 sin^2\left(\theta\right)\right)^{\frac{3}{2}}} \tag{2.3}$$

The two limit cases:

$$E\left(\theta = \frac{\pi}{2}\right) = \frac{q\gamma}{r^2} \tag{2.4}$$

$$E\left(\theta = 0\right) = \frac{q}{r^2\gamma^2} \tag{2.5}$$

are the electric fields in the direction of motion and in the normal direction. These expressions have some important implications. A static particle (or observed in its rest frame) presents the same electric field in the perpendicular and parallel direction of motion, as the field is isotropically distributed. As soon as the particle is in motion, the transverse field increases by a factor of γ^3 with the field in the direction of motion suppressed by $1/\gamma$. As the particle approaches the speed of light, its electric field is therefore almost only transverse. This effect is shown in Fig. 2.2 presenting the electric field spatial distribution for particles with increasing velocities. The field lines become denser in the direction perpendicular to the motion. In the ultra-relativistic limit, the angle of the field lines becomes very narrow, and the particle field is approximately transverse to the direction of motion.

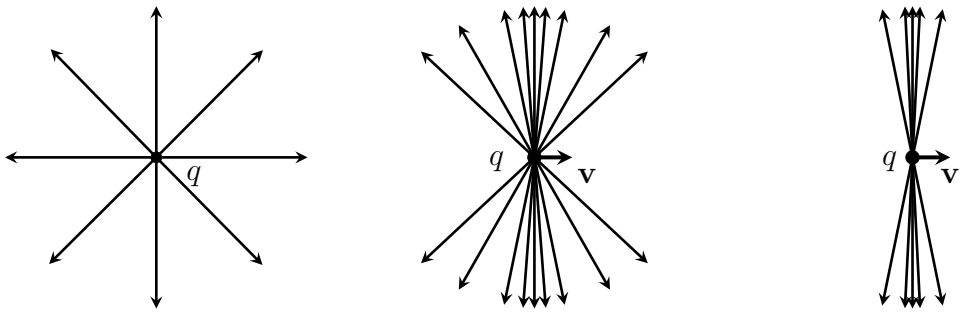

$\beta = 0$ $\quad 0 < \beta < 1$ $\quad \beta \sim 1$

Figure 2.2: Schematic representation of the spatial field distribution for a charge q at rest ($\beta = 0$) and at increasing velocities.

In general, the transformation of the electric and magnetic field from an arbitrary frame Σ to another Σ' in motion with a relative velocity $\mathbf{v}$ is expressed by the following relations [74]:

$$\mathbf{E}' = \gamma\left(\mathbf{E} + \beta \times \mathbf{B}\right) - \frac{\gamma^2}{\gamma + 1}\beta\left(\beta \cdot \mathbf{E}\right) \tag{2.6}$$

$$\mathbf{B}' = \gamma\left(\mathbf{B} + \beta \times \mathbf{E}\right) - \frac{\gamma^2}{\gamma + 1}\beta\left(\beta \cdot \mathbf{B}\right) \tag{2.7}$$

Therefore, a purely electric or magnetic field can exist only in the rest frame (where $\beta = 0$), but becomes a mixture of the two as soon as they are observed from a different frame.

2.2 Signal generation in a capacitive BPM

2.2.1 Wall currents

In particle accelerators, a beam of charged particles typically travels through a metal beampipe inducing an image charge on the conductive walls. In the ultra-relativistic limit, the particles' field is transverse to the motion direction. Therefore, the image charge on the beampipe walls will form a section of a cylinder that follows the beam particles. The total electric current induced on the beampipe walls, called the wall current, will be equal to the beam current but will have the opposite polarity. Assuming the beam is in the centre of a perfectly conducting cylindrical beampipe, the wall current distribution i_{wall}

along the circumference is

$$i_{\text{wall}}(t) = -\frac{I_{\text{beam}}(t)}{2\pi b} \tag{2.8}$$

where I_{beam} is the beam current and b is the beampipe radius.

On the other hand, an off-centred beam will cause a redistribution of the image charge density. In the regions closer to the beam, a larger part of the total charge is induced. The different image charge formation in a transverse section of the beampipe is shown in Fig. 2.3. The wall current distribution can be calculated using the image method [75]:

$$i_{\text{wall}}(r, \theta, \phi, b; t) = -\frac{I_{\text{beam}}(t)}{2\pi b}\left[\frac{b^2 - r^2}{b^2 + r^2 - 2brcos\,(\phi - \theta)}\right] \tag{2.9}$$

where b is the beampipe radius, r and θ are the polar coordinates that define the beam position and ϕ is the angular section of the wall considered in the calculation. For any fixed angle ϕ, a current I_{L} can be obtained by integrating Equation 2.9 (see Fig. 2.3). Similarly, if we consider the opposite section, i.e. $\phi - 180^\circ$ one can defined a current I_{R}.

The beam position along the horizontal axis can be found from the image currents as [75]:

$$\frac{I_{\text{L}} - I_{\text{R}}}{I_{\text{L}} + I_{\text{R}}} = \frac{4sin\,(\phi/2)}{\phi}\frac{x}{b} + \mathcal{O}\left(\frac{x^2}{b^2}\right) \tag{2.10}$$

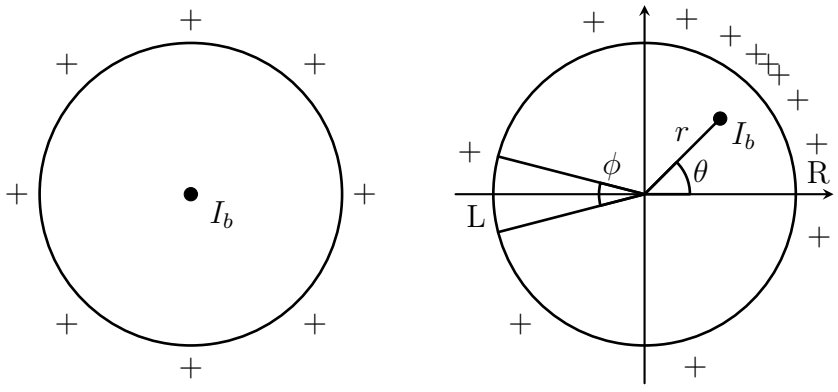

Figure 2.3: Charge distribution on the beampipe walls for an ultra-relativistic beam. On the left, the case for a centred beam, while on the right the beam is displaced. The induced image charges are schematically indicated with a + sign.

where ϕ is the angular region considered for calculations, $x = rcos(\theta)$ is the beam position along the horizontal axis and b is the beampipe radius. This expression shows that by sensing the image currents on two opposite sections of a beampipe, the response to the beam position is linear around the beampipe centre. For larger displacements, the higher-order terms start to play a significant role and the response becomes nonlinear.

2.2.2 Response of an ideal electrostatic BPM

Electrostatic BPMs measure the beam position within the beampipe by coupling the beam's electric field to metal antennas, so-called buttons, which are electrically isolated from the otherwise grounded beampipe. The wall current induced on them by the passing beam produces signals that are then used to compute the beam position. Figure 2.4 shows a diagram of a button BPM and its interaction with the beam. The button produces an output voltage $V_{\mathrm{out}}(t)$ that is sensed by read-out electronics. A particle beam with charge Q_{beam} and current $I_{\mathrm{beam}}(t)$ induces a current $I_{\mathrm{PU}}(t)$ on the button, causing a difference of potential V_{out} across the load impedance R_{L}.

Considering a button with an area A and at a distance a away from the beam, the induced current is [76]:

$$I_{\mathrm{PU}} \equiv -\frac{dQ_{\mathrm{PU}}}{dt} = \frac{A}{2\pi a l} I_{\mathrm{beam}}(t) = \frac{A}{2\pi a l} \frac{dQ_{\mathrm{beam}}(t)}{dt} \tag{2.11}$$

where l is the button length. The derivative of the beam charge can be rewrit-

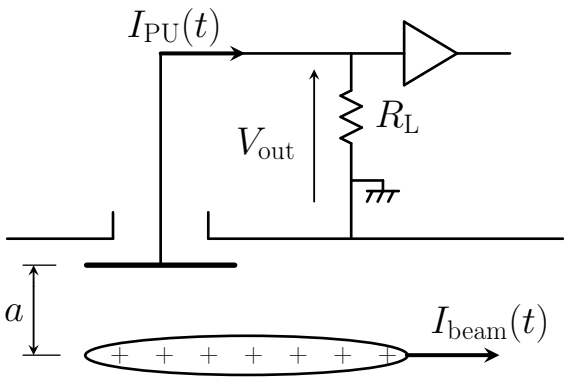

Figure 2.4: Schematic representation of the beam interaction with a button BPM.

ten as

$$\frac{dQ_{\mathrm{beam}}(t)}{dt} = \frac{l}{\beta c}\frac{dI_{\mathrm{beam}}(t)}{dt} = \frac{l}{\beta c} I_{\mathrm{beam}}(\omega), \tag{2.12}$$

where $I_{\mathrm{beam}}(\omega)$ is the Fourier transform of the beam current, β the relativistic velocity and c the speed of light. Finally, the output voltage can be written

$$V_{out}(\omega) = Z_t(\beta, \omega)\, I_{\mathrm{beam}}(\omega), \tag{2.13}$$

where Z_t is defined as the transverse impedance of the BPM. This expression indicates that the signal produced by a BPM is a convolution of its transverse impedance and the beam spectrum. It is fundamental to note that for relativistic beams the transverse impedance depends, to a first approximation, only on the BPM's electric and geometric characteristics. Conversely, the beam spectrum is purely related to the beam physics and it is virtually independent of the instrument design.

The equivalent circuit for an electrostatic button is a current source that produces a portion of $I_{\mathrm{beam}}(t)$ depending on the button area and the beam distance. The induced current is discharged through the shunt resistor R_{L} and the capacitance between the button and the vacuum pipe. Since the impedance is defiend as $Z^{-1} = R^{-1} + i\omega C$, the button voltage becomes

$$V_{\mathrm{out}}(\omega) = \frac{R_{\mathrm{L}}}{1 + i\omega R_{\mathrm{L}} C} I_{\mathrm{PU}}(\omega) = \frac{1}{\beta c}\frac{A}{2\pi a}\frac{R_{\mathrm{L}}}{1 + i\omega R_{\mathrm{L}} C} I_{\mathrm{beam}}(\omega) = \Gamma \frac{1}{a} I_{\mathrm{beam}}(\omega) \tag{2.14}$$

where Γ is a term that depends on the geometrical and electrical characteristics of the BPM. The magnituide of the generated signal is inversely proportional to the distance from the beam.

Let us now consider two identical buttons at opposite positions in the beampipe: the buttons R and L. The voltage induced by the beam is:

$$V_{R,im}(\omega) = \Gamma \frac{1}{a_R} I_{beam}(\omega) \tag{2.15}$$

$$V_{L,im}(\omega) = \Gamma \frac{1}{a_L} I_{beam}(\omega) \tag{2.16}$$

The two Γ factors are identical as they are calculated for identical geometries. The output signals of the two buttons will vary depending on the distances a_R and a_L from the beam. In order to reconstruct the beam position, the Δ

quantity is calculated, defined as the difference of the electrode signals

$$\Delta = V_{R,im} - V_{L,im}(\omega) = \left(\frac{1}{a_R} - \frac{1}{a_L}\right) \Gamma I_{beam}(\omega) \tag{2.17}$$

This can be made independent of the beam intensity I_{beam} and the Γ factor by dividing it by the sum of the electrode signals

$$\Sigma = V_{R,im} + V_{L,im}(\omega) = \left(\frac{1}{a_R} + \frac{1}{a_L}\right) \Gamma I_{beam}(\omega) \tag{2.18}$$

to obtain the Δ/Σ quantity, that is normally used to characterise a BPM response. This has the advantage of being independent of the beam intensity and the button geometry. In fact, the analytical expression is uniquely dependent on the beam position:

$$\frac{\Delta}{\Sigma} = \left(\frac{1}{a_R} - \frac{1}{a_L}\right) / \left(\frac{1}{a_R} + \frac{1}{a_L}\right) = \frac{a_L - a_R}{a_L + a_R} \tag{2.19}$$

2.2.3 Effect of multiple beams

The electrostatic BPM response is more complicated when it simultaneously measures two particle bunches with different lengths. Let us consider an electron beam (e) and a proton beam (p), each of them with Gaussian shape, composed of N_e and N_p particles and with 1-σ bunch length of σ_e and σ_p, respectively. The response of the R button is now determined by a superposition of two components:

$$V_R(\omega) = \Gamma \frac{1}{a_{R,e}} I_{beam,e}(\omega) + \Gamma \frac{1}{a_{R,p}} I_{beam,p}(\omega) \tag{2.20}$$

where the terms $a_{R,e}$ and $a_{R,p}$ denote the respective distances of each beam from the button.

Equation 2.19 becomes dependent not only on the position of both beams, but also on their relative intensities:

$$\frac{\Delta}{\Sigma} = \frac{\frac{I_{beam,e}(\omega)}{I_{beam,p}(\omega)} \left(\frac{a_{L,e} - a_{R,e}}{a_{L,e} a_{R,e}}\right) - \left(\frac{a_{L,p} - a_{R,p}}{a_{L,p} a_{R,p}}\right)}{\frac{I_{beam,e}(\omega)}{I_{beam,p}(\omega)} \left(\frac{a_{L,e} - a_{R,e}}{a_{L,e} a_{R,e}}\right) + \left(\frac{a_{L,p} - a_{R,p}}{a_{L,p} a_{R,p}}\right)} \tag{2.21}$$

Assuming that both bunches have a longitudinal Gaussian distribution, the

beam current can be expressed in the time and frequency domains as

$$I_{beam}(t) = \frac{eN}{\sqrt{2\pi}\sigma} \exp\left\{-\frac{1}{2}\frac{t^2}{\sigma^2}\right\} \tag{2.22}$$

$$I_{beam}(\omega) = \frac{eN}{\sqrt{2\pi}} \exp\left\{-\frac{1}{2}\sigma^2\omega^2\right\} \tag{2.23}$$

An interesting case for further development of this work is when one bunch is much longer and more intense than the other. This condition is expressed as $\sigma_e << \sigma_p$ and $N_e << N_p$. Therefore, the expression of the bunch spectra for the two bunches becomes:

$$I_{beam,p}(\omega) = \frac{eN_p}{\sqrt{2\pi}} \exp\left\{-\frac{1}{2}\sigma_p^2\omega^2\right\} \tag{2.24}$$

$$I_{beam,e}(\omega) = \frac{eN_e}{\sqrt{2\pi}} \exp\left\{-\frac{1}{2}\sigma_e^2\omega^2\right\} \approx \frac{eN_e}{\sqrt{2\pi}} \tag{2.25}$$

The approximation of the e beam spectrum holds if $\omega \ll 1/\sigma_e$, i.e. in a frequency region where the wavelength is considerably larger than the bunch length. In this frequency region, the e beam spectral power can be considered constant. Figure 2.5 presents the beam current in time and frequency domains, for beams with parameters as in Table 2.1.

The term $I_{beam,e}(\omega)/I_{beam,p}(\omega)$ in Equation 2.21 can now be rewritten by

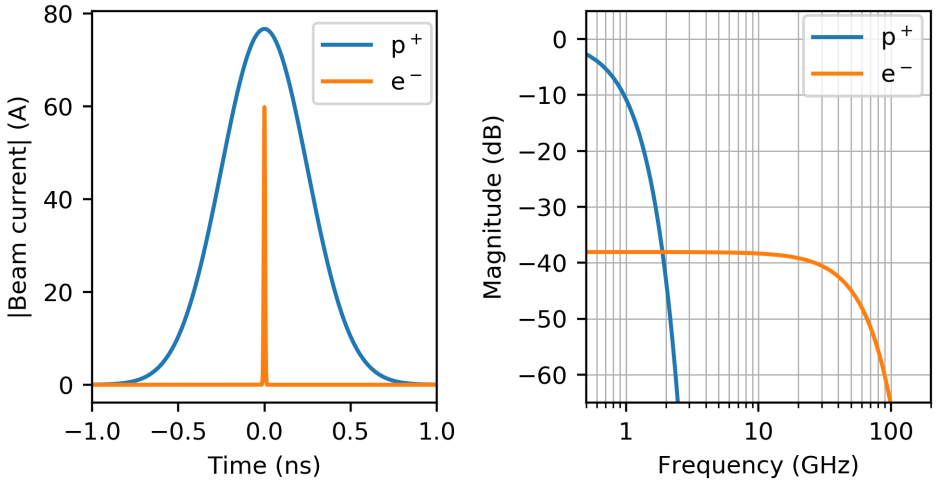

Figure 2.5: Time (on the left) and frequency domain (on the right) comparison of the parameters of the proton and electron bunches reported in Tab. 2.1.

means of Equation 2.24 and 2.25 as

$$\frac{I_{beam,e}(\omega)}{I_{beam,p}(\omega)} = \frac{N_e}{N_p} \exp\left\{\frac{1}{2}\sigma_p^2\omega^2\right\} \tag{2.26}$$

This leads to two interesting observations:

- for $\sigma_p^2\omega^2 \to 0$: if the detection frequency is not sufficiently high, the exponent in 2.26 reduces to 1. From Equation 2.21, the Δ/Σ factor is the sum of the e and p beams contribution, but with the e part attenuated be a factor of $\frac{N_e}{N_p}$. As it has been assumed that $N_e << N_p$, the Δ/Σ response is strongly determined by the p beam position.

- $\omega >> \sigma_p^{-1}$: if the detection frequency is sufficiently high, the opposite effect will take place. The Equation 2.21 terms which depend on the electron-beam position are amplified and the Δ/Σ factor is determined mostly by the electron beam position.

In the case of the AWAKE beam parameters reported in Table 2.1, the two beams have the same spectral power at 1.9 GHz, as shown in Fig. 2.5. The approximation in Eq. 2.25 of constant electron spectral power in this frequency range introduces an error of the order of 0.1‰, and it is therefore justified.

Name	Charge		σ
	nC	ppb	ps
Proton beam	48	3×10^{11}	250
Electron beam	0.6	3.7×10^9	4

Table 2.1: Beam parameters used in AWAKE.

2.3 Design parameter constraints

The constraints in designing beam instrumentation for the AWAKE experiment are listed in Table. 2.2. They are set by both the beam parameters, and the beampipe dimensions.

A key parameter for the design is the rather large beampipe aperture of 60 mm which constitutes an additional complication for a beam position monitoring system working at high frequencies. The beampipe itself acts as a

Parameter	p^+ beam	e^- beam
Beampipe diameter	60 mm	
Charge	48 nC	$100 - 600$ pC
Length	250 ps	$1 - 4$ ps
Energy	400 GeV	$16 - 20$ MeV

Table 2.2: AWAKE parameters for this study.

circular waveguide, propagating the electromagnetic waves with frequencies above the cutoff frequency of

$$f_c = \frac{1.8412\, c}{2\pi r} = 2.93 \text{ GHz} \tag{2.27}$$

where r is the waveguide radius and c the speed of light [74]. Unwanted electromagnetic radiation is expected to be generated by the beam passage through the vacuum chamber discontinuities, and will propagate along the beampipe, with some fraction of it potentially coupling to the BPM system and resulting in an unwanted spurious signal. In the case of AWAKE, this phenomenon is particularly likely to occur as several metres of the beamline near the plasma cell contain a large number of insertions and diagnostic devices. Therefore, a pickup operating above the beampipe cutoff frequency will not only produce a signal contaminated by the unwanted wakefields, but also the amount of spurious signal will depend on its exact installation location.

Another fundamental design constraint is given by the large charge ratio between the proton and electron beams. For the moment, both beams are considered to have a Gaussian longitudinal charge distribution. The implications of a different shape of the proton beam are discussed in Section 2.4. The power of the most intense electron beam, with a charge of 600 pC, is 38 dB lower at DC than that of the proton beam, as shown in Fig. 2.6. The electron bunch charge of 100 pC corresponds to an additional decrease of 15.5 dB of the spectral power. Under these conditions, the point at which the electron and proton beams feature the same spectral power moves between 1.9 GHz and 2.2 GHz. As discussed previously, successful detection of the electron beam has to be carried out at frequencies higher than these, to reduce the contribution of the proton beam to the signal.

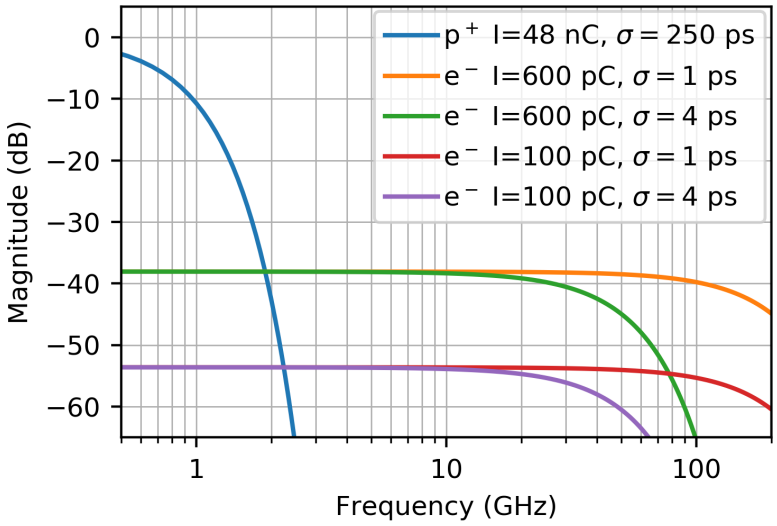

Figure 2.6: Beam spectral power as function of frequency for AWAKE experiment assuming Gaussian beams.

2.4 Proton beam spectrum measurement

The preceding discussion shows that for the AWAKE beam parameters, a frequency range in which the signal generated by the electron beam is stronger than the proton signal has to be determined. Assuming Gaussian longitudinal charge distributions for both beams, this frequency is above 1.9 or 2.2 GHz, depending on the operational scenario.

A fundamental question to be answered is whether the proton bunch longitudinal distribution extracted from the SPS can be approximated by a Gaussian curve. A non-Gaussian beam shape could include stronger components at high frequency, and therefore increase the frequency which both beams have the same power. Therefore, the correct determination of the proton bunch spectrum is crucial for selecting the operating frequency of an electron beam position monitoring system.

Conversely, this issue does not apply to the electron bunch, as due to its very short duration, the spectral power will remain constant up to tens of GHz. At even higher frequencies, the electron spectrum will drop similarly. Therefore, for the purpose of this study, the electron beam is assumed Gaussian.

Selecting the electron BPM system working frequency has a large impact on the possible technical solutions that can be exploited to carry out the measurement. Although it is possible to build a pickup using conventional coaxial

components working at very high frequencies, this becomes increasingly difficult above around 20 GHz.

The proton beam at AWAKE is produced in the CERN accelerator complex, using a modified version of an LHC-type beam with higher intensity [77], [78]. The proton bunch is accelerated up to 400 GeV in the SPS, and then it is adiabatically rotated in longitudinal phase space in order to shorten its length. The beam is stored in the SPS for an arbitrary period of time, waiting for the synchronisation with the AWAKE laser system. Therefore, after the rotation, the bunch is extracted each time at a different synchrotron phase and the resulting beam longitudinal profule varies shot-by-shot. This effect is worsened if the bunch has an internal sub-structure. Sources of longitudinal bunch profile imperfections can be e.g. energy and phase mismatch in the accelerator, and an imperfect extraction trajectory that causes the beam to scrape on the extraction septum aperture [13].

It is not possible to study the beam profile variation in the SPS before the extraction as the only suitable instrument installed in the SPS is the Wall Current Monitor [79] but its bandwidth does not exceed 2 GHz [80] which is not sufficient to resolve the profiles in the frequency range interesting for this study. The AWAKE beamline is better equipped for such a measurement, as it uses longitudinal beam diagnostics to observe the proton bunch self-modulation in plasma [66].

2.4.1 Longitudinal beam profile measurement

A number of scintillation and Optical Transition Radiation (OTR) screens are installed in the AWAKE beamline both up- and down-stream of the plasma cell [67]. They are generally used for beam emittance measurements. The OTR screens, although presenting a modest light yield compared with the scintillation screens, can be also used to sample the bunch longitudinal structure and measure the bunch length, due to their intrinsically fast response.

OTR is emitted when a particle traverses a material discontinuity, generating photons due to the different permittivities in the forward and backward directions [81]. To measure the temporal distribution of the proton bunch, an OTR screen is placed 3.5 m downstream from the plasma-cell exit [82]. A schematic representation of the setup is shown in Fig. 2.7. The screen is made of a 280 μm thick silicon wafer coated with 1 μm aluminum. The backward-emitted transition radiation is sent through an optical line to a streak camera.

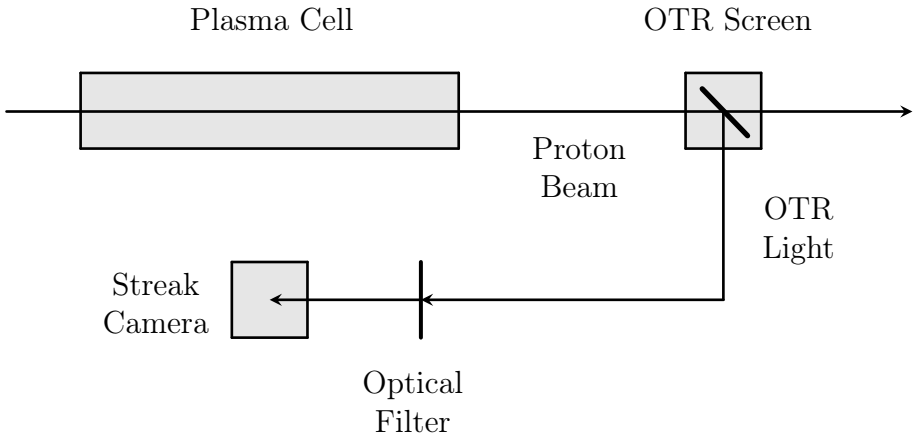

Figure 2.7: Schematic representation of the setup for longitudinal profile measurement.

Before entering the streak camera, the light is filtered using a bandpass filter with a central wavelength of 450 nm and a passband of 50 nm. The filter limits the optical dispersion effects from the optical transfer line and levels off the energy of the photons arriving at the streak camera photocathode, preventing resolution loss due to chromatic effects.

A streak camera is the only camera type that is capable of measuring the temporal profile of a light pulse while sacrificing the information on one of the two spatial directions. The principle of operation of a streak camera is shown in Fig. 2.8. The incident light pulse hits a photocathode after passing through a narrow slit, and gets converted to an electron beam with the same temporal structure. The produced electron beam is accelerated by a static potential difference, and then passes between two deflection plates with a time-varying potential difference applied between them. The potential difference determines the electron bunch tilt, as the head and the tail of the bunch are subjected to a different potential. This process maps the longitudinal bunch structure into a transverse profile. The electron bunch is then amplified by a MicroChannel Plate (MCP) and reaches a phosphor screen where the electrons are converted back into light. Finally, the light is recorded by a camera.

As outlined above, a streak camera measurement presents a high degree of complexity. In fact, the temporal resolution of a streak camera is intrinsically limited by the incident photon flux, and so the produced electron current which is proportional to the input light intensity. With large enough electron current, a strong space-charge force will increase the beam size, resulting in a dilated temporal profile of the camera output pulse. Hence, streak cameras

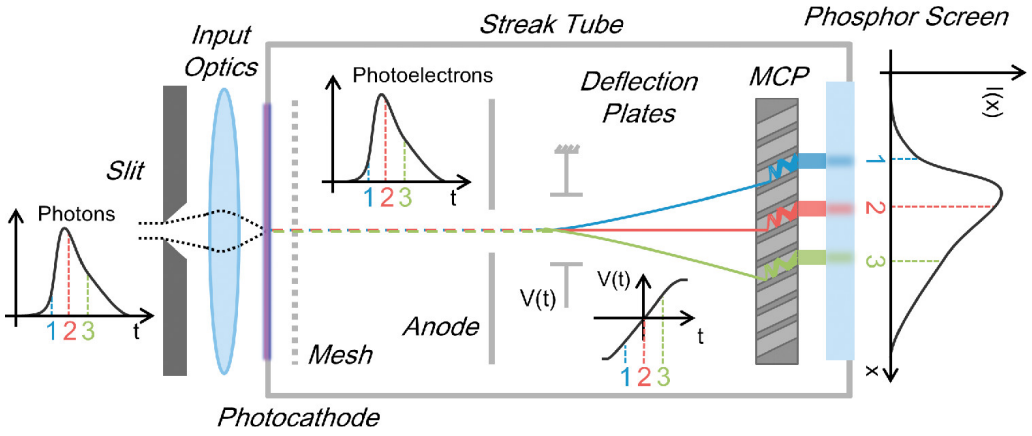

Figure 2.8: Schematic representation of the streak camera principle of operation [83].

are usually operated with limited input light and a sufficient output signal is produced via frame stacking. However, such a technique cannot be used for precise beam-profile measurements and each output profile has to be considered separately. Nonetheless, accurate estimation of the high-frequency components in the measured profile is not trivial since each single profile is polluted by the camera noise.

A Hamamatsu streak camera with ps resolution [84] is installed in the AWAKE experiment and is used to measure primarily the effect of the plasma wakefields on the proton beam [66], [82]. A longitudinal profile of an undulated proton bunch was measured using a time window of 1 ns, a slit width of 20 μm and MCP gain of 40. Figure 2.9 presents a typical proton bunch streak camera image. The beam profile is obtained by integrating the pixel intensity over the rows of the sensor matrix in the region of interest (ROI) to reduce the noise resulting from the dark areas. The pixel intensities are compensated to remove the effect of non-linear streak voltage which is recorded for each frame. Once a beam profile is obtained it is zero-padded and its baseline is removed. The plots in the left column of Fig. 2.10 show three examples of recorded longitudinal beam profiles. A Gaussian fit of each profile is also reported for comparison. Although some intensity dependent noise is expected from the used streak camera, the proton bunch presents consistent features clearly deviating from an idealistic Gaussian profile. In particular, the sharp edges at the beginning and at the end of the profiles cannot be attributed to the measurement noise.

A frequency domain representation of the measured profiles is presented in the right column of Fig. 2.10 and compared to that of the fitted Gaussian curve.

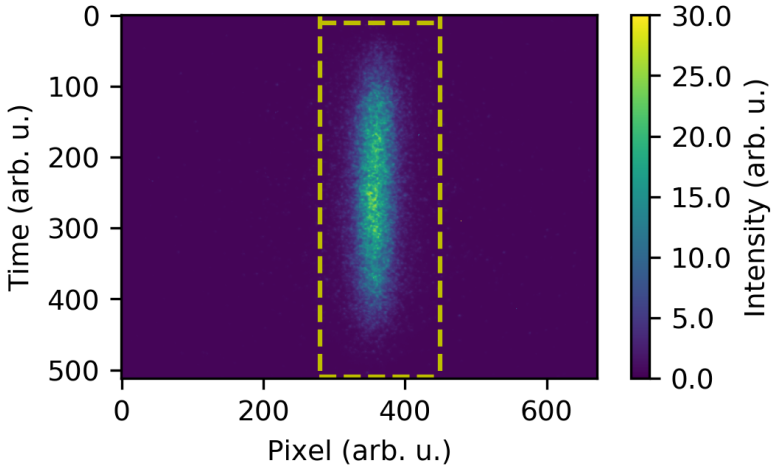

Figure 2.9: A streak camera image of the OTR light for an AWAKE proton bunch of 2.1×10^{11} protons. The vertical axis is time with one pixel being 2.2 ps. The horizontal axis is one of the transverse dimensions of the OTR light beam. The dashed yellow rectangle indicates the region of interest for beam profile calculation.

High resolution of the Fourier transform is achieved through zero-padding of the time domain profile, elongating the considered time window by a factor of 32.8. The zero padding consists of artificially elongating the profile tails, adding measurement points of zero value before and after the measured signal. In this case, this process does not alter the physical content of the signal (which has the form of a narrow pulse). This elongation of the profile in time domain provokes a finer binning of the spectrum in the frequency domain, as for the Discrete Fourier Transform (DFT) the binning is $\Delta f = 1/T_s$ where Δf is the frequency binning and T_s is the signal length in time domain [85]. The result of this manipulation is visible in the plots on the right hand side of Fig. 2.10, where the black dots are the DFT calculated using only the profile in the measured time window, and the blue trace is the result after the zero padding of the signal.

The measurements indicate that the bunch spectrum contains significantly more power at high frequency than would be expected of a Gaussian bunch. It is therefore necessary to understand if this is a measurement artefact. The complicated nature of the streak camera measurement of OTR light makes it very difficult to precisely estimate the amount of introduced noise. However, some camera-induced noise can be reduced by averaging many profiles after aligning them in time. The profile center can be estimated as the point in

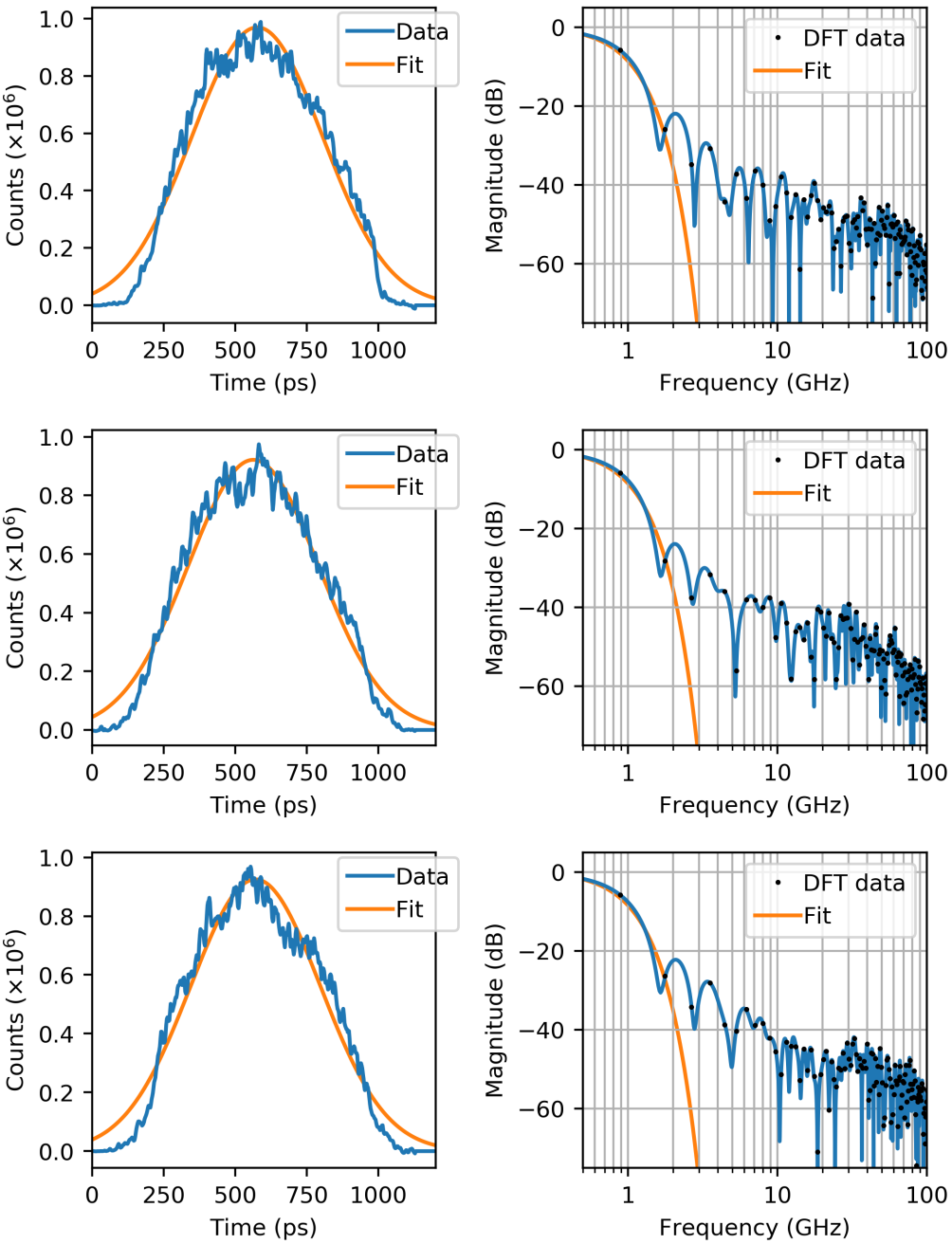

Figure 2.10: Three examples of longitudinal proton bunch profiles measured with the streak camera together with Gaussian fits (orange lines). The plots to the left are in time domain while those to the right are their Fourier transforms. The spectrum is calculated for the raw camera image (black dots) and after increasing the frequency resolution (blue line).

the middle of the full width at half maximum (FWHM). A profile and its Fourier transform obtained by averaging 179 images are shown in Fig. 2.11. In

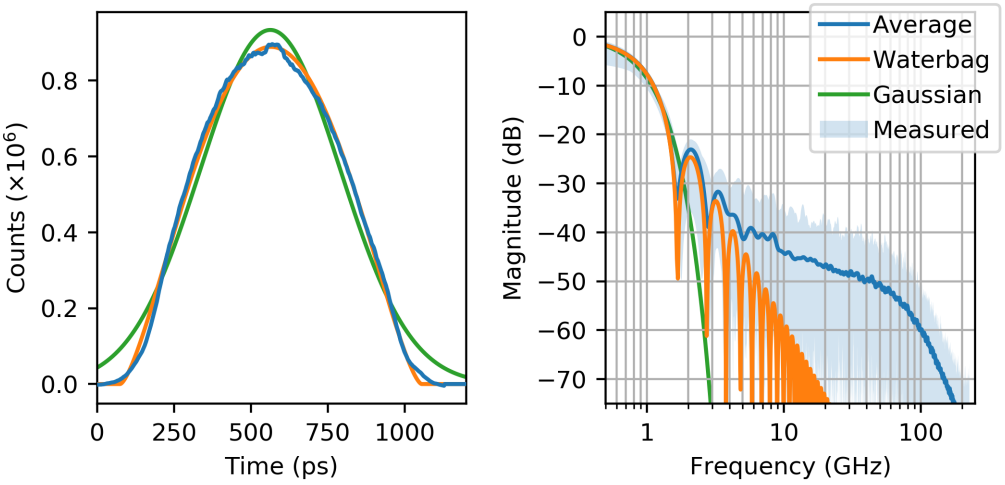

Figure 2.11: Average beam profile (blue) in time domain (left) and its Fourier transform (right). The envelope of all recorded pulse spectra is shaded. Fits with the Gaussian and water-bag function are reported for comparison. The fit parameters are indicated in Table 2.3.

	Gaussian	Water bag
Function	$A \exp\left\{\frac{1}{2}\left(\frac{x-\mu}{\sigma}\right)^2\right\}$	$\frac{A}{t_b}\left(1-\left(\frac{2t}{t_b}\right)^2\right)^{3/2}$
A	9553 ± 10	8887 ± 3
μ (ps)	559.1 ± 0.3	565.97 ± 0.07
length (ps)	216.7 ± 0.3	979.0 ± 0.2

Table 2.3: Fit parameters for the Gaussian and water bag functions. The bunch length is estimated as σ for the Gaussian and t_b for the water-bag function. It has to be noted that the two lengths are defined differently and, therefore, are not directly comparable.

the frequency domain plot, the envelope of all measured profiles is also shown around the average. Although a large part of the noise is removed, also most of the fine features are smoothed out. Two fits are also reported: Gaussian and using a 'water-bag' function. The parameters for both fits are reported in Table 2.3. The former clearly reproduces the data poorly also for the average profile. The latter is defined as

$$f_{\mathrm{WB}}(t, t_b, A) = \begin{cases} A\left(1-\left(\frac{2t}{t_b}\right)^2\right)^{\frac{3}{2}} & |t| < \frac{t_b}{2} \\ 0 & |t| \geq \frac{t_b}{2} \end{cases} \tag{2.28}$$

where t_b is the bunch length measured at the base of the distribution and A is a normalisation parameter. In the frequency domain, the water bag fit shows a good agreement with the measurement up to ∼3 GHz. At higher frequencies, however, the measured proton spectrum decays much more slowly than for the fit.

It is therefore not possible to precisely estimate the proton-bunch spectrum using streak-camera measurements at the frequencies of interest for this study, i.e. above ∼ 5 GHz. However, the most pessimistic estimation of the proton spectrum is the envelope of the measurements, which includes the noise induced by the measurement. The water bag function fit is an approximation of the beam shape that works well up to ∼3 GHz. It can be assumed that the real beam spectrum lies between the measurement envelope and the water-bag fit. Furthermore, substantial shot-by-shot variations of the proton-bunch spectrum at high frequencies was measured. Therefore, the average proton spectrum will be taken into account in the BPM system design as this is the best data available at the moment. It has to be noted, however, that the proton bunch might contain a different amount of power at a given frequency than accounted for using the average spectrum.

2.4.2 Implications for the system performance

The AWAKE electron BPM system needs to work at a frequency at which the electron beam signal is stronger than the proton one. As the working frequency choice is crucial for successful measurements, it is not sufficient to use the nominal parameters of 100-600 pC bunch charge and 1-4 ps bunch length [60], [61]. An independent measurement of the AWAKE electron bunch length was carried out [86], and is presented in Fig. 2.12.

The measurement shows that the bunch length is correlated with the bunch charge up to ∼ 400 pC, and then it stabilises at 5 ps. A linear fit was performed on the data for charges smaller than 400 pC. The values in Table 2.4 are obtained using the fit function, and serve as realistic design parameters of future beam instrumentation at AWAKE. It is not clear what caused the measurement discrepancy at 475 pC charge. However, other measurements indicate that 5 ps bunch length is achievable at this charge with appropriate injector settings.

The measured electron beam parameters are compared with the average proton bunch spectrum in Fig. 2.13 assuming that the longitudinal charge

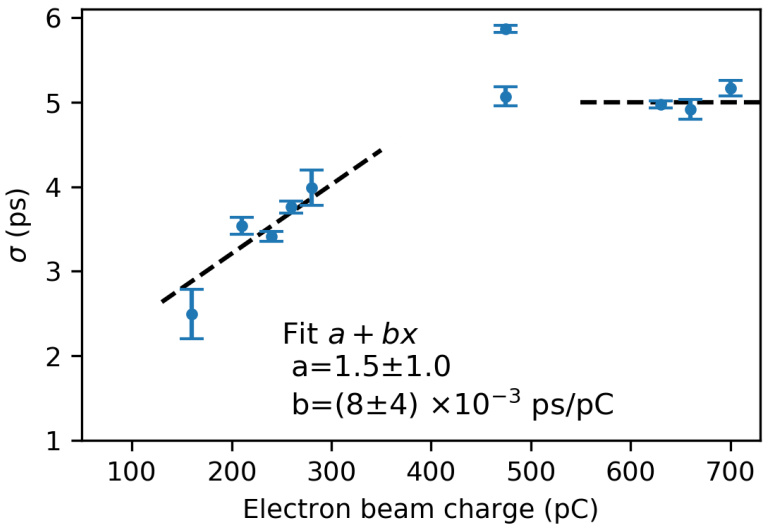

Figure 2.12: AWAKE electron bunch length (1 sigma) for different bunch-charge values. The measurement was carried out using the OTR screen light with the streak camera. The measurement error is its standard deviation obtained with three different processing methods. The dashed line on the left is a linear fit for charges smaller than 400 pC. The dashed line on the right indicates the mean value of the three measured points at charge larger than 500 pC [86].

Electron beam				
Charge (pC)	100	200	300	>500
σ (ps)	2.4	3.4	4	5

Table 2.4: Bunch-lengths obtained from measurements.

distribution in the electron bunch is Gaussian.

The ratios of power carried by the electron and proton bunches at different frequencies are shown in Fig. 2.14. For the lowest electron bunch charge of 100 pC, the electron bunch signal is stronger than the proton one only at a frequency above 100 GHz. For charges of 300 pC and above, the electron signal becomes stronger than the proton in the range between 15 and 40 GHz. Also, this analysis shows that there is no substantial difference between carrying out the measurement at 20 or 30 GHz. For technical and cost reasons a lower frequency is preferable, hence an operating frequency of the electron BPM system of around 20 GHz appears to be the optimal choice.

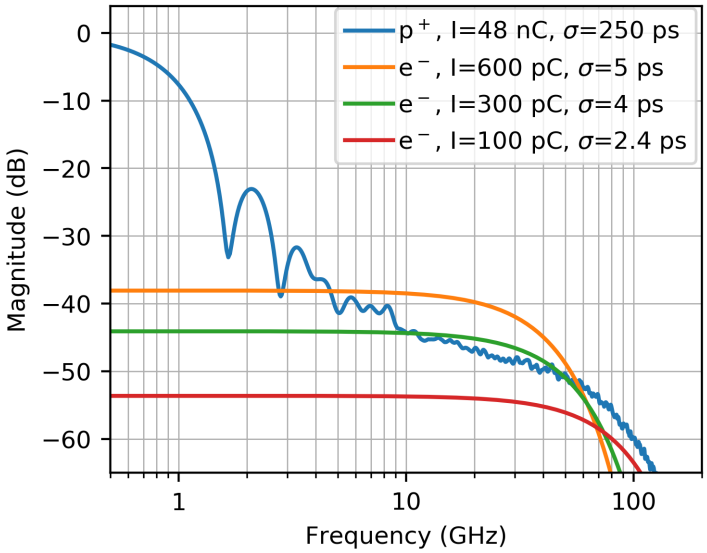

Figure 2.13: Comparison of spectra of the measured average proton bunch and electron bunch with different parameters. The electron bunch is assumed to follow a Gaussian longitudinal-charge distribution.

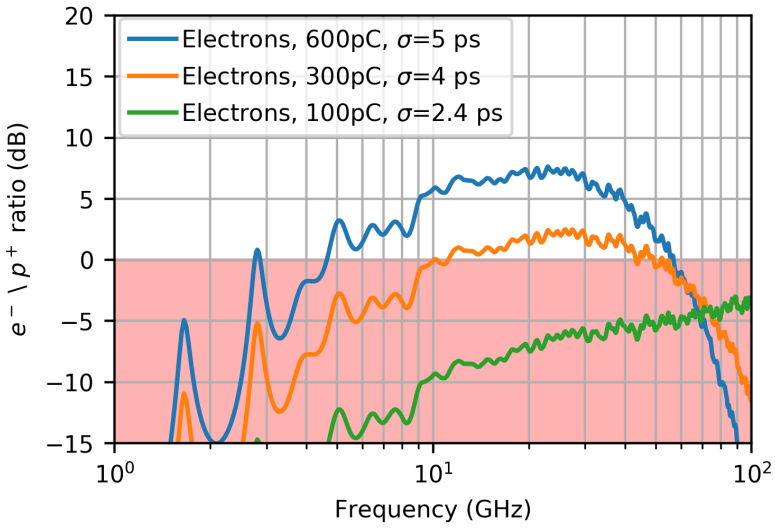

Figure 2.14: Ratios between the measured average proton-bunch and the electron-bunch spectra for different electron-beam parameters. The red area marks the region where the proton signal is more intense than the electron one.

In summary, the position measurement of a shorter and less intense electron beam can be achieved in the presence of a more intense and longer proton beam, provided that the measurement is carried out in a frequency band where the

signal from the electron beam is dominant. An analytical model for Gaussian beams has been presented. The impact of the non-Gaussian shape of the AWAKE proton drive beam was discussed, although the available data do not allow a precise estimate of the proton beam spectrum in the tens-of-GHz regime due to the nature of the streak-camera measurement. However, an estimation using the average proton-beam longitudinal profile was derived, showing that the AWAKE nominal electron-beam signal is dominant over the proton-beam signal in the 20-30 GHz range. Detecting the beam position in this high-frequency range presents major technical difficulties. An innovative approach to solve this problem based on the emission of Cherenkov Diffraction Radiation is presented in Chapter 3.

Chapter 3

A BPM working in the quasi-optical regime

The development of this work so far showed that to perform a simultaneous measurement of the electron and proton beam positions for the AWAKE experiment, it is necessary to carry out the measurement at a very high frequency.

Not many traditional pickup designs work reliably at frequencies of the order of tens of GHz, although designs based on conical metal buttons have been realised [87]. However, such pickups also couple to the low-frequency part of the beam spectrum, so additional filtering would be required to separate the short but weak electron bunch from the long but very intense proton bunch. Instead, it was decided to explore a less conventional method based on dielectric buttons. Dielectric materials placed in proximity to a moving charged particle beam produce electromagnetic radiation, which can be used as a beam diagnostic tool.

Diffraction Radiation (DR) is produced by the interaction of the beam field with any discontinuity in the beampipe geometry. Therefore, in some cases DR can be used for non-intercepting beam position measurements. A particular case of DR is the Cherenkov Diffraction Radiation (ChDR) that is produced in a material when the beam field propagates at a velocity faster than the speed of light in that medium. This radiation mechanism is becoming popular for short-bunch applications [88], with some expertise already present at CERN where proof of principle devices of this kind were tested in recent years [89].

This chapter presents the design, simulation and test of a proof-of-principle beam position monitor based on ChDR. Later, using the lessons learned, a BPM design proposal compatible with the AWAKE beam-line requirements is

presented.

3.1 Vavilov-Cherenkov Diffraction Radiation

Vavilov-Cherenkov radiation is produced when a charged particle traverses a dielectric medium faster than the velocity of light in that medium [90], [91]. Since its discovery in 1937, Vavilov-Cherenkov radiation (ChR) has been widely used in nuclear and particle physics [92], and astrophysics [93], [94] as a diagnostic tool. Its characteristic feature is photon emission at a well defined angle according to the relation

$$\cos(\theta_{\mathrm{Ch}}) = \frac{1}{\beta n} \tag{3.1}$$

where θ_{Ch} is the so-called Cherenkov angle, the $\beta = v/c$ factor is the particle velocity expressed in units of the speed of light in vacuum c, and n is the refractive index of the material through which the particle is propagating.

Vavilov-Cherenkov Diffraction Radiation (ChDR) is a particular kind of Diffraction Radiation propagating at the Cherenkov angle (Eq. 3.1), but contrary to ChR the ChDR-producing particle does not penetrate the radiating medium. Instead, it is the particle's electromagnetic field that interacts with the medium. Recently, the application of ChDR drew interest for nondestructive relativistic beam diagnostics [88], [95] and as a high-frequency radiation source in accelerators [96], and was compared with other radiation production mechanisms [97].

The theory of ChDR generation has been studied in detail in the last decade. ChDR can be described as one of the forms of polarisation radiation, together with Transition Radiation, Smith-Purcell Radiation, Diffraction Radiation and others [98]. The analytical model is based on the Polarisation Current Approach (PCA) [99]. According to the PCA theory, a charged relativistic particle passing in proximity to a dielectric medium induces a surface current on the medium. The emitted polarisation radiation field is generated by interactions between the particle field and the induced surface current. Although PCA is a powerful tool to derive the polarisation radiation form, this was accomplished only for some simple radiator geometries in vacuum [100], [101]. For the development presented in this thesis, it is interesting to understand how PCA works.

The PCA model considers a charged particle moving at a constant speed with the Lorentz factor $\gamma = (1-\beta^2)^{-\frac{1}{2}}$ that generates an electric field $\mathbf{E}^0(\mathbf{r}, \omega)$.

The EM fields are considered in frequency domain, however it is possible to switch between frequency and time domain by applying direct and inverse Fourier transformation. If the particle is passing in proximity to a dielectric material, the interaction of the particle field with the dielectric generates a polarisation current on the surface of the dielectric target. The polarisation current can be expressed as

$$\mathbf{j}_{\mathrm{pol}}(\mathbf{r},\omega) = \sigma(\omega)\left(\mathbf{E}^{0} + \mathbf{E}^{\mathrm{pol}}(\mathbf{j}_{\mathrm{pol}})\right) \tag{3.2}$$

where $\mathbf{r}$ is the spatial coordinate vector, $\sigma(\omega)$ is the frequency-dependent material conductivity, $\mathbf{E}^{0}$ is the Fourier transform of the particle field in vacuum and $\mathbf{E}^{\mathrm{pol}}$ is the Fourier transform of the field generated by the currents induced in the dielectric target.

The conductivity of a dielectric material is related to its permittivity $\epsilon(\omega)$ via

$$\sigma(\omega) = \frac{i\omega}{4\pi}\left(1 - \epsilon(\omega)\right) \tag{3.3}$$

By inserting the polarisation current (Eq. 3.2) into Maxwell's equations and solving for a volume V_T that contains the polarisation currents, the magnetic field of the polarisation radiation can be expressed as [98], [100]

$$\mathbf{H}^{\mathrm{pol}} = \nabla \times \frac{1}{c}\int_{V_T} \sigma(\omega)\mathbf{E}^{0}(\mathbf{r}',\omega)\frac{\exp\left\{\frac{i\omega}{c}\sqrt{\epsilon(\omega)}\,|\mathbf{r}'-\mathbf{r}|\right\}}{|\mathbf{r}'-\mathbf{r}|}\,d^{3}r'. \tag{3.4}$$

Equation 3.4 gives the exact solution of Maxwell's equations. This solution is independent of the target shape and the characteristics of the dielectric material. However, the equation describes any emission due to polarisation currents, hence not only the ChDR emission but also the DR emission from the radiator edges. Moreover, it can not always be solved analytically.

The general approach for solving Equation 3.4, followed for example in [89], is to approximate the integral in the far-field conditions and then solve it for simple radiator geometries in vacuum. Although this approach can be very powerful, it is not suitable for the radiator geometry used in this work. In fact, the radiator used in the tests not only features a complex geometry, but also some dielectric surfaces are in contact with metal. This adds the complication of electromagnetic wave reflections and interference building up during the propagation of the DR and ChDR fronts along the dielectric volume. The radiator geometry is described in detail in Section 3.2. In light of the difficulties

in deriving analytical expressions to predict the radiation produced by the radiator, it was decided to study the problem with numerical simulations; these are described in Section 3.3.

Although it is not possible to study analytically the radiation production in a target with complex shape, it is instructive to consider the emission for a flat dielectric radiator of finite length. Figure 3.1 depicts a particle passing parallel to a flat dielectric radiator, with an impact parameter h and a radiator length d. The interaction of the particle field with the radiator will generate one forward and one backward DR front when the particle field encounters each perpendicular edge of the material. Additionally, as the particle travels along the radiator surface, the ChDR front will also form inside the target. The different components of energy lost by the particle due to the radiation were estimated using PCA [100].

The spectrum of emission for a single particle due to DR losses is given by [102]:

$$\left(\frac{dW}{d\lambda}\right)_{\mathrm{DR}} = \alpha\hbar c\sqrt{\frac{\gamma}{2h}}\left(\frac{\epsilon(\lambda)-1}{(\epsilon(\lambda)\mp 1)^2}\right)^2 \cdot \cdot \frac{1-\cos\left[2\pi d\left(\sqrt{\epsilon(\lambda)\mp 1}\right)/\lambda\right]}{\lambda^{3/2}} \exp\left\{-\frac{4\pi h}{\gamma\lambda}\right\} \tag{3.5}$$

where α is the fine structure constant, $\hbar$ is the reduced Planck constant, γ is the Lorentz factor, λ is the wavelength and d the dielectric length. In the $\pm$ terms, the negative and positive signs describe the forward and backward DR, respectively. Similarly, the spectrum of emission of a single particle for ChDR

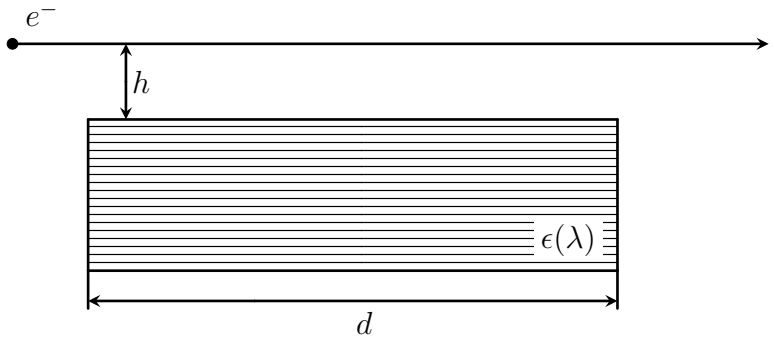

Figure 3.1: Schematic representation of a particle passing in proximity to a flat dielectric radiator.

losses is [102]:

$$\left(\frac{dW}{d\lambda}\right)_{\text{ChDR}} = \frac{\alpha\hbar c}{2\pi\Theta_m}\frac{1}{\lambda\sqrt{\lambda B}}\frac{\sqrt{\epsilon(\lambda)-1}}{\epsilon(\lambda)}\,\text{erf}\left[\sqrt{\frac{\pi B}{\lambda}}\phi_m\right]\cdot \\ \cdot\left(\frac{A\Theta_m}{\lambda}\,\text{si}\left[\frac{A\Theta_m}{\lambda}\right]+\cos\left[\frac{A\Theta_m}{\lambda}\right]-1\right)\exp\left\{-\frac{4\pi h}{\gamma\lambda}\right\} \tag{3.6}$$

where Θ_m and ϕ_m are the polar and azimuthal angles describing the size of the Cherenkov cone, $\text{erf}(x)$ is the error function, $\text{si}(x)$ is the sine integral function [103], and the A and B factors are

$$A = 2\pi d\sqrt{\epsilon(\lambda)-1}$$

$$B = 2\gamma h\left(\epsilon(\lambda)-1\right)$$

The field of a particle bunch is the sum of the radiation of the individual particles [104]. The emitted radiation from a bunch of particles can be expressed as [105]

$$I(\omega) = I_{\text{SP}}(\omega)\left(N + N(N-1)\left|f(\omega)\right|^2\right) \tag{3.7}$$

where I_{SP} is the single-particle emission, N is the number of particles in the bunch and $f(\omega)$ is the bunch form factor, i.e. the Fourier transform of the bunch longitudinal profile. For a bunch with a Gaussian longitudinal charge distribution emitting ChDR, I_{SP} is expressed by (3.6) and $f(\omega)$ is the Fourier transform of a Gaussian curve. Two radiation components can be identified in Equation 3.7. The first term is the incoherent part of the emission, which is proportional to the number of particles N. The second term is the coherent part of the emission, which is emitted at wavelengths longer than the bunch length and therefore with very small phase differences in the emissions by the individual particles. This determines a constructive interference of the emissions of the single particles, that enhances the produced radiation intensity as $N(N-1) \sim N^2$.

For illustration, figure 3.2 shows the spectrum of ChDR emission by a Polytetrafluoroethylene (PTFE or teflon) radiator exposed to a 100 pC 2 ps-long (1 σ) electron bunch for varying impact parameters and radiator lengths.

In summary, the total emission from a dielectric target depends on two main components: the Diffraction Radiation generated at the target edges, and the Cherenkov Diffraction Radiation generated by the interaction of the

beam field with the radiator surface. The former depends on the geometry, materials and impact parameter, while the latter also depends on the radiator area that is exposed to the beam field.

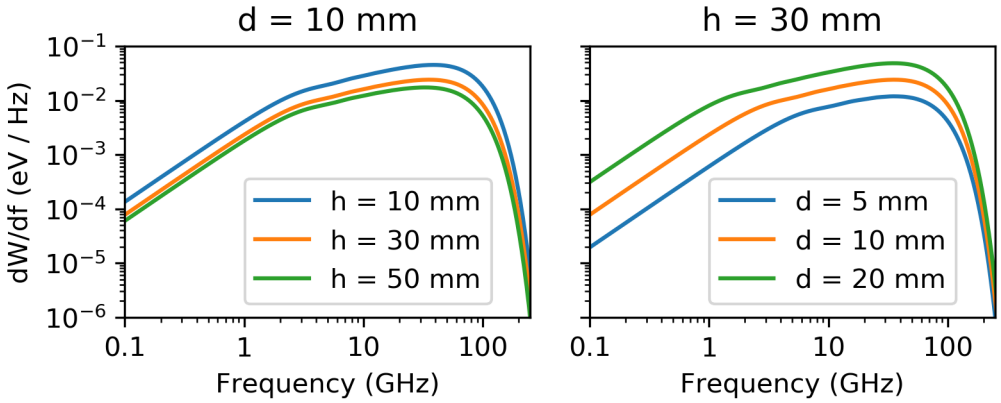

Figure 3.2: Spectrum of ChDR emission for a 100 pC 2 ps-long electron beam passing in proximity to a PTFE flat target. On the left, the emission of a 10 mm long radiator was computed at various impact parameters. On the right, the impact parameter is kept constant at 30 mm and the length of the radiator is varied.

3.2 A BPM prototype for in-air testing

A proof-of-principle beam position monitor prototype was designed at CERN. The goal of this design was to validate the use of ChDR for beam position monitoring while retaining the largest possible flexibility in the tests. For this reason, a simple and rather inexpensive design was realised for in-air testing. The test device was manufactured from a 26 cm-long aluminium tube. An internal beampipe diametre of 60 mm was chosen, matching the AWAKE common beamline dimensions. Figure 3.3 illustrates the longitudinal section of the device. Four circular holes were drilled at 45° angle and fitted with 18 mm-diameter PTFE inserts. The inner face of the dielectric inserts follows the beampipe curvature. The inserts are fixed to the main body with bolts.

The test device is depicted in Fig. 3.4. As the particle beam passes through the device, ChDR is generated at the radiator surface. It then propagates through the radiator and finally is emitted in air. Figure 3.5 (a) shows the PTFE radiator surface trimmed inside the beampipe. The produced electromagnetic wave is then coupled to RF detectors. The downstream section of the

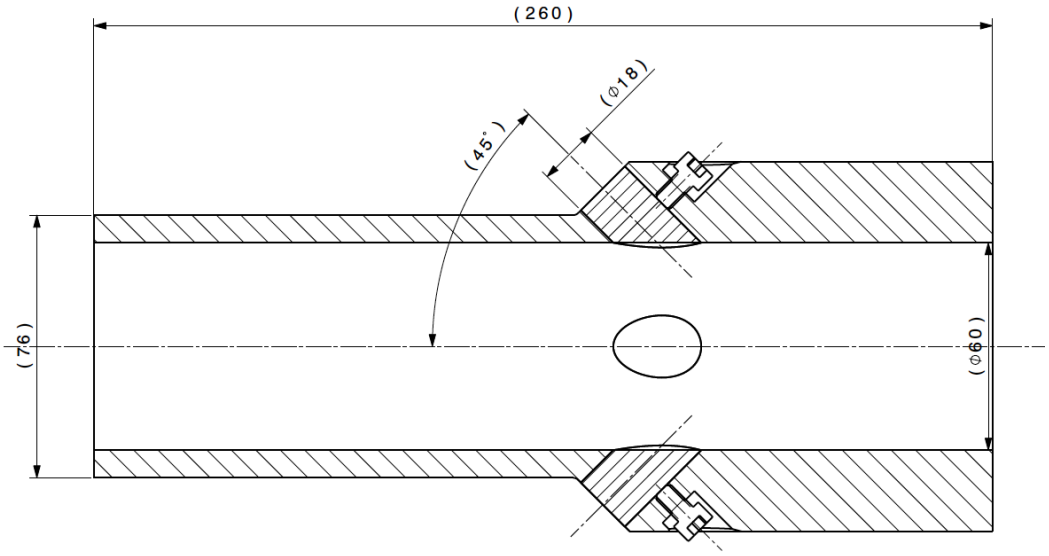

Figure 3.3: A longitudinal section of the test device. The beam moves in the right-to-left direction. The two components oriented at 45° and filled with the denser ruling are the PTFE inserts.

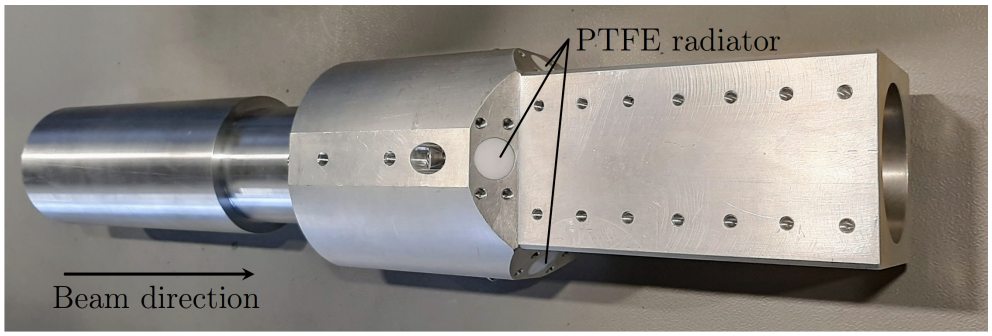

Figure 3.4: The test device with the extension tube installed. The beam direction is left-to-right. The white disks on the faces cut at 45° are the radiator output surfaces. Above the radiator, the fixing bolt is visible. The part of the device downstream from the radiators has a square external shape and was fitted with threaded holes to support the detection system.

test device features multiple tapped holes used to fix the RF detection system. Figure 3.5 (b) shows the RF detection system mounted on its support. Each detector is housed in a metal case that is clamped to a support pillar. Standard optical posts were used for this purpose. The support of the pillar can slide, adjusting the distance from the radiator. By means of this system, the distance and orientation of the detection system with respect to the radiator can be adjusted. The test device, and all the support part were designed and manufactured in-house.

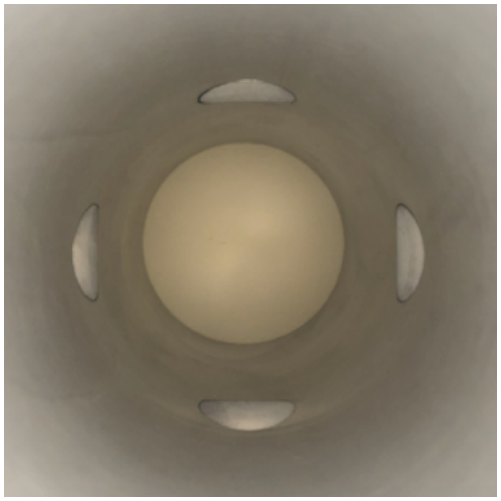

(a) The four PTFE inserts seen from inside the beampipe. The four white disks are the radiators machined to be flush with the beampipe inner surface.

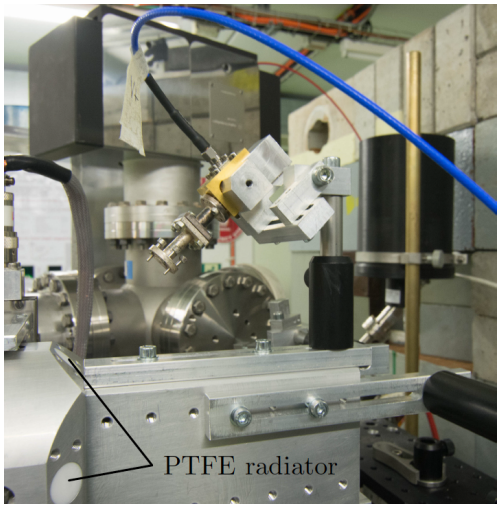

(b) The RF detectors installed on supports downstream of the radiators. The white disk on the metallic edge oriented at 45° is the face of the radiator that emits the electromagnetic wave into air. The electric field is then coupled into the waveguide facing the radiator.

Figure 3.5: The PTFE inserts and the RF detectors of the test device.

To reduce electromagnetic disturbance due to geometric discontinuities, a metal extension tube with a matching internal diameter was fixed to the upstream end of the test device. The whole assembly was supported on an external bracket which could then be attached to a static or motorised support.

The electric field generated by the test device was measured using commercially available zero-bias[1] RF detectors enclosed in a metal cases with a waveguide input and a coaxial output. The detection system is described in detail in Section 3.4.1.

3.3 Electromagnetic simulations

A 3D model of the test device was created in CST Studio 2018 [106] for electromagnetic simulations. The test-device dimensions, shown in Fig. 3.3, are large compared to the sub-millimetre wavelengths generated by the short electron bunch. The initial attempts with uniform (or automatic) meshing of the model led to more than 2^{31} mesh cells, which cannot be simulated using the available

[1]Zero-bias RF detectors are a class of RF detectors that does not require a bias voltage to operate.

resources, as it would require access to a multi-node computer cluster. Therefore, the model had to be simplified. An additional issue arose due to the large volume of air added outside the device in order to reliably reproduce the test conditions.

Out of the multiple electromagnetic-field solvers available in CST, two were considered to simulate the test device: the wakefield solver and the Particle In Cell (PIC) solver.

The wakefield solver uses the time-domain electromagnetic field of the moving bunch of charged particles. For the investigated problems, the simulated bunch had a Gaussian longitudinal profile and was relativistic. In this approach, the beam is only a source, and no feedback effect of the EM fields on the beam is considered. A big advantage of the wakefield solver is that the beam field is considered also at the boundaries so the beam field enters the simulation domain smoothly with the correct shape [107].

The Particle In Cell (PIC) solver approximates the beam as a group of macroparticles, each of them carrying a given charge and with its own coordinates in the bunch. The macroparticles are treated independently and interact with themselves and the EM fields in their environment. Accordingly, PIC solvers are extensively used in plasma physics [108] and in beam dynamics studies with space charge [109]. Such an analysis allows the user to define any beam-charge distribution, provided that the number of macroparticles is sufficiently high. Further advantages include the possible exploitation of GPU computing and low noise in specific simulation conditions [110]. An important drawback of the PIC solver is that the beam fields are distorted at the simulation domain boundaries, and some space must be allowed for the field to develop in a realistic way. Figure 3.6 compares the beam field computed by the PIC and wakefield solvers.

Due to the large size of the simulation domain, it would be impractical (if not impossible) to use the PIC solver, as it requires an additional volume for the beam field to develop properly. Therefore, the wakefield solver was selected to simulate the test device after preliminary investigations at low resolution. Nevertheless, the model had to be simplified to be simulated with reasonable time and computing power. Two approaches were investigated independently: approximating the problem with a thin slice and appropriate boundary conditions, and applying custom meshing to reduce the computing power required to simulate a full test device with a single radiator.

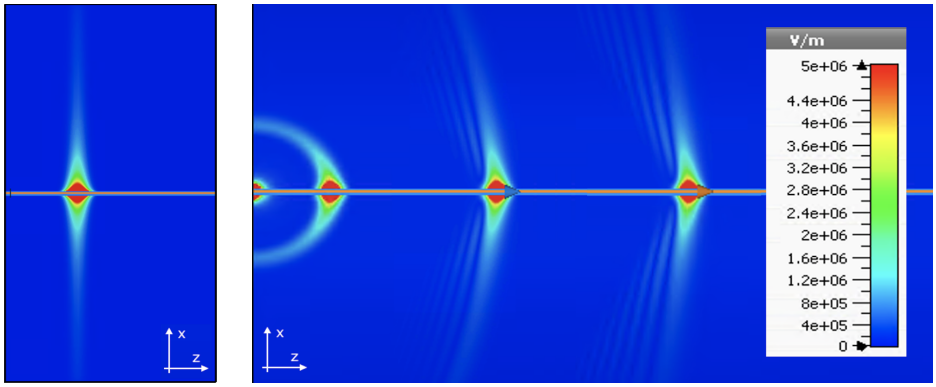

(a) Bunch electric field in a wakefield simulation.

(b) Bunch electric field in a PIC simulation.

Figure 3.6: Comparison of the beam electric field in vacuum close to the edge of the simulation domain for (a) the wakefield solver and (b) the PIC solver. The beam propagates left to right and the absolute value of the electric field is plotted. An electron bunch of 100 pC charge and 1 ps length is shown. In the wakefield simulation (a) the beam enters the simulation domain smoothly and the electric field is realistic already at the simulation domain boundary. The displayed frame shows the field density 20 ps into the simulation. Conversely, for the PIC simulation (b), there is some necessary time for the field to assume a realistic distribution. Picture (b) shows the field expansion process for the bunch at 2, 20, 100 and 200 ps into the simulation. A uniform meshing is used, assuring 100 GHz simulation bandwidth with 20 mesh cells per wavelength. The disturbance trailing the beam field in (b) is caused by the noise in the simulation, and can be controlled by decreasing the mesh cell size. The colour bar for the field intensity is valid for both plots.

3.3.1 Simulation of a slice

As the first attempt to simplify the model and reduce the simulation size, the test device was cut longitudinally into a quasi-2D model. In the past, researchers at other institutes used the 2D electromagnetic simulation code MAGIC [111] for simpler designs. However, MAGIC was not available for simulations of the test device and CST Studio does not offer 2D solvers. A similar approximation was nonetheless achieved by applying appropriate boundary conditions to a thin slice of the full model. A longitudinal slice of the test device was made just a few mesh cells thick. Open boundary conditions were used on four sides, but in the cutting plane where magnetic boundary conditions ($H_t = 0$) were used (see Fig. 3.7). Perfect vacuum was used as a background material. Despite being an approximation of the full model, such an approach gave insight into the internal propagation of the electromagnetic fields. How-

ever, in the thin slice model the DR generation is affected by the approximated geometry of the material edges. Fig 3.8 shows the formation of the ChDR front at the beam passage, and the propagation of the electromagnetic fields

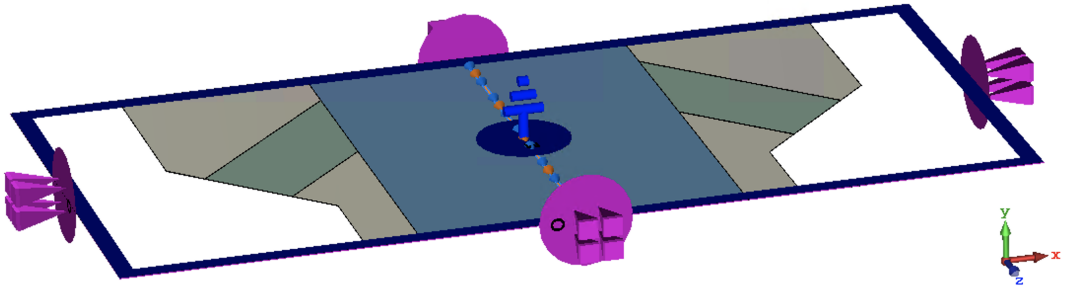

Figure 3.7: Boundary conditions of the slice model. The blue ground symbol represents the magnetic boundary condition ($H_t = 0$), which is applied at both edges of the simulation domain in the y direction. The violet symbol with the four pyramids represents the open boundary condition, used in all the other boundaries.

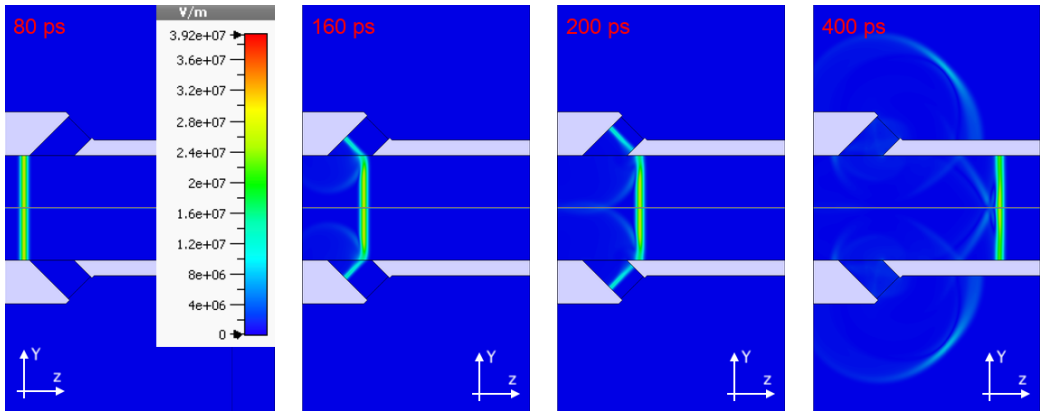

(a) t = 80 ps (b) t = 160 ps (c) t = 200 ps (d) t = 400 ps

Figure 3.8: Electric field in the slice model at different time steps. In (a) the beam is propagating in the beampipe and has not yet interacted with the radiator. In (b) the beam is interacting with the radiator, producing the ChDR front that propagates at 45° inside the radiator. Furthermore, the DR produced by the interaction with the upstream radiator edge is visible inside the beampipe with a circular wave-front. In (c) the propagation continues after the beam passed the radiator and the ChDR front advances. After exiting the radiator (d), the field expands in vacuum as a circular wave. The formation of additional circular DR fronts due to the interaction with the radiator edges visible in (b), (c) and (d) is described later for the 3D simulation. The simulation parameters are: a simulation bandwidth of 50 GHz, 20 mesh cells per wavelength, 100 pC and 5 ps long electron beam.

that follow. The importance of having a quickly running model to assess the internal reflections will be manifest in Section 3.4.6 where the effect of the back-propagation of the beam through the device is shown.

3.3.2 3D Simulation of a single radiator

Although the simulation of a slice shows how the electromagnetic radiation propagates inside the device, a more quantitative 3D simulation is beneficial. The DR that is generated depends on the geometry of material discontinuities and edges that are present, in this case, in the beampipe. These cannot be reliably modelled with a thin slice and a full 3D simulation is necessary.

For 3D simulations, the model was divided into six areas, shown in Fig. 3.9. To minimise the simulation time, each area was meshed with a different resolution. In the figure, the beam propagates left-to-right along the path indicated by the orange and blue arrows. Inside the beampipe, the beam propagates in

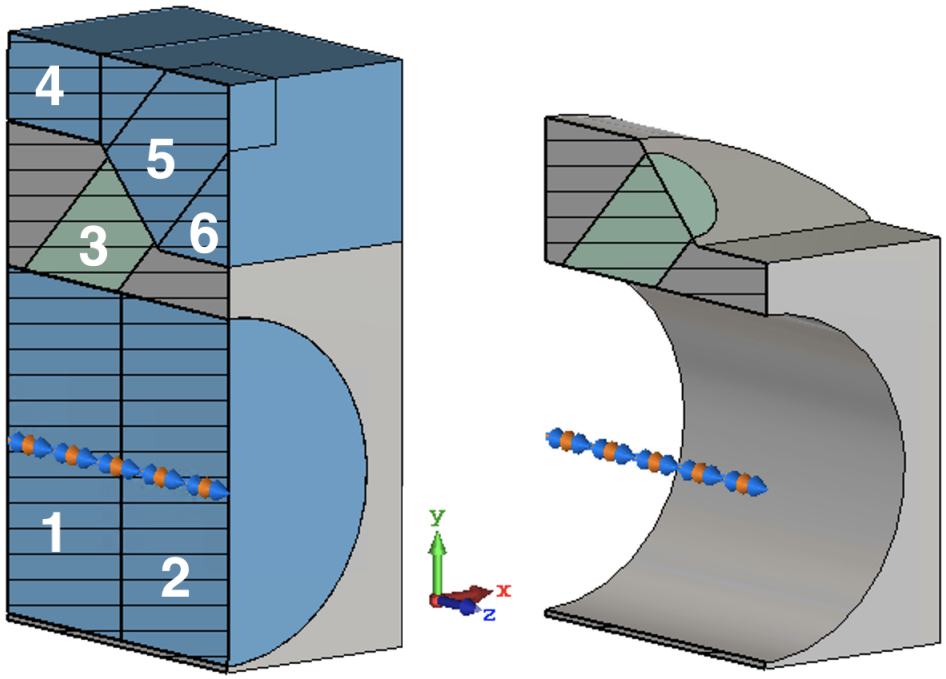

Figure 3.9: Longitudinal section of the 3D model used for the electromagnetic simulations. On the left the model is displayed including the vacuum parts and indicating the different meshing regions, on the right the vacuum volumes are hidden. Light blue volumes are made of vacuum, light green volume is the PTFE radiator, and volumes in grey are metal. The orange and blue arrows indicate the propagation path and direction of the beam.

vacuum through regions 1 and 2. Region 1 contains the interface with the radiator. When the beam leaves region 1, it stops contributing to the production of electromagnetic waves in the radiator, and therefore region 2 is excluded from the simulation to save computing resources. The produced ChDR and DR propagate through the dielectric radiator, marked with 3. At the radiator exit face, the radiation starts to propagate in free space. As the radiation is produced at the Cherenkov angle, at which also the radiator is installed, the radiation exits along the normal to the radiator face. Therefore, region 5 is the most interesting as it is where the forward emitted radiation is present. Region 6 is meshed with a coarser mesh as the fields generated there are not so interesting, saving substantial computing resources. The metal volume is treated with the same mesh resolution as region 6. To save additional computing resources, region 4 is also excluded from the simulation.

Regions 1, 3 and 5 are vital to understand the operation of the test device, while the other regions can be ignored or simulated with lower resolution. To achieve this, different mesh groups are defined manually, with the parameters reported in Table 3.1. At the interface between regions with different mesh size, the finest meshing is extended to the adjacent region for 1 mm.

Such a meshing technique led to a tenfold reduction of the number of mesh cells compared with the same 3D model with uniform meshing and 20 cells per wavelength. Usually, simulations with the optimised mesh completed in less than two days on the CERN computing cluster.

An additional complication of large volume and large bandwidth simulations is the size of the output, which is of the order of 25 GB and 15 thousand files for the discussed model. Most of the space is used to save the field monitor outputs. Due to the size of the simulation, the field values can be recorded only by probing the field in a point or on a plane, but not in the whole simulated volume. Given the output size, transferring the simulation results from

Mesh group	Cells/λ	Cell size (mm)	Regions on Fig. 3.9
High resolution	20	0.15	1, 3, 5
Low resolution	3	1	6
Metal	3	1	-
Do not simulate	0	-	2, 4

Table 3.1: Parameters of the different meshing regions used in the simulations. The calculations are performed for a simulation bandwidth of 100 GHz which corresponds to a wavelength of 3 mm.

the computing cluster to the local computer is a complex operation and can require up to half a day, which has to be added to the computing time.

The result of a simulation for a 2 ps long, 100 pC electron beam propagating through the test device described in Section 3.2 is presented in Fig. 3.10. The picture shows the absolute value of the electric field 90, 140 and 220 ps into the simulation. The results offer valuable insights into the electromagnetic radiation production mechanics. Figure 3.10 (a) shows the beam as it passes next to the radiator. The ChDR front propagating at the Cherenkov angle inside the radiator is clearly visible. An additional spherical front is visible inside the beam pipe following the direct field of the bunch (marked as DR1). This is the DR front generated at the discontinuity due to the upstream edge of the radiator. In (b) the beam has passed the radiator. A second front of DR both in the beampipe and in the radiator is visible, provoked by the interaction with the downstream radiator edge (indicated as DR2). Looking forward in time in (c), the electromagnetic wave has left the radiator. The forward front being ChDR, while the trailing wavefront is the DR from the interactions with the radiator edges. Looking more carefully inside the radiator, there is a less intense front of radiation visible that was reflected back inside (indicated as REF). This is a part of the DR front, that traveled inside the radiator at some

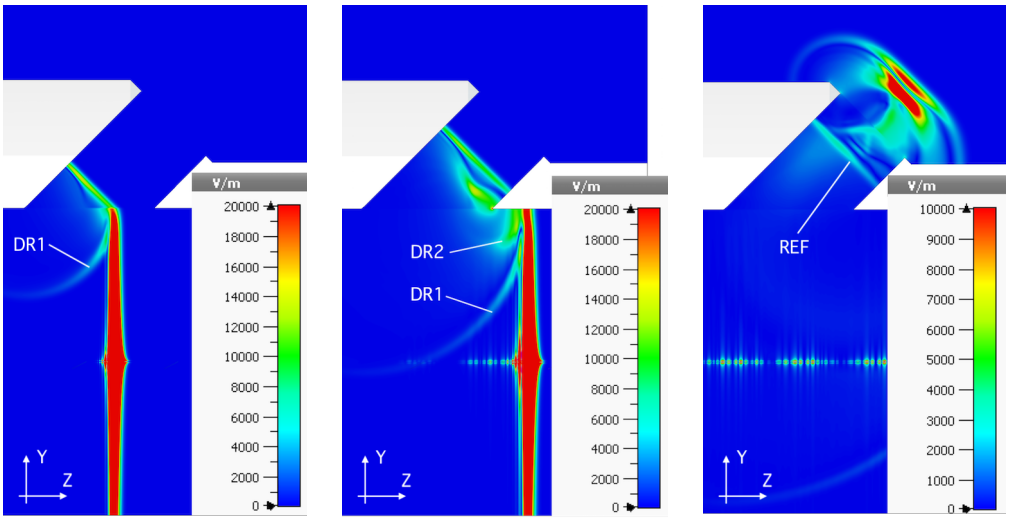

(a) t= 90 ps (b) t= 140 ps (c) t= 220 ps

Figure 3.10: 3D simulation of the electric field produced by the beam passing next to a PTFE radiator with the same geometry as the one used for the tests at CLEAR. The grey and white areas represent the metal pipe. The ChDR and DR front formations are visible and are described in detail in the text.

angle to the radiator output surface normal. On the other hand, the ChDR is completely emitted as it travels perpendicularly to the output surface. Please note that the field intensity scale of (c) had to be enhanced to visualise the reflected field.

3.3.3 Position sensitivity

The absolute value of the electric field is considered as

$$E_{\mathrm{abs}} = \sqrt{E_{\mathrm{x}}^2 + E_{\mathrm{y}}^2 + E_{\mathrm{z}}^2} \tag{3.8}$$

where the different components of the field are calculated for each point in space and time.

To estimate the response of the test device to beam-position variations, i.e. its sensitivity, the electric field is sampled in vacuum 10 mm above the centre of the radiator exit surface. The field probe position is shown in Fig. 3.11 (a). A number of different beam positions are simulated. Figure 3.11 shows the absolute value of the electric field simulated in the time domain for three beam positions. The two peaks visible correspond to the two emission fronts of ChDR and DR that are clearly visible in Fig. 3.10 (c).

The beam position was swept over a 30 mm range around the centre of the beampipe. The resulting electric field was considered over a 100 ps-wide window, and the RMS of the windowed signal was calculated. The Δ/Σ quantity was then computed from the RMS values. The opposite electrode was not simulated due to the limited computing resources, but its signal could be deduced from the response of the simulated electrode assuming symmetry. Figure 3.12 shows the RMS electric field at the observation point from the simulated dielectric radiator and from the the opposite radiator (deduced from the geometry). The squared electric field was then used to compute the Δ/Σ as a function of the beam position. The device response exhibits a linear behaviour near the beampipe centre, and becomes non-linear for larger displacements. A linear fit for beam displacements of ± 3 mm from the beampipe centre was carried out, resulting in a sensitivity of 1.3×10^{-1} mm^{-1}.

3.3.4 Improvements to the simulation capabilities

Two significant limitations of the CST wakefield solver were identified during the simulation work. First, the solver can only simulate particle bunches with

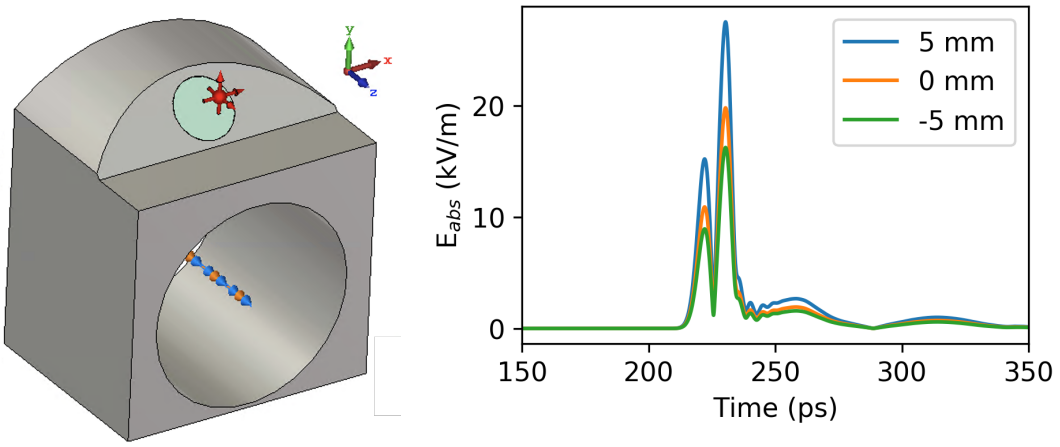

(a) Simulation model.

(b) Absolute value of the electric field at the probe position.

Figure 3.11: On the left, the simulated 3D model is shown, including the probe point of the electric field (in red). On the right, the absolute value of the electric field at the probe point is shown for three different beam positions. Zero is the beampipe centre and the positive positions correspond to the beam getting closer to the radiator. The field is sampled in a single point, 10 mm above the centre of the radiator output surface.

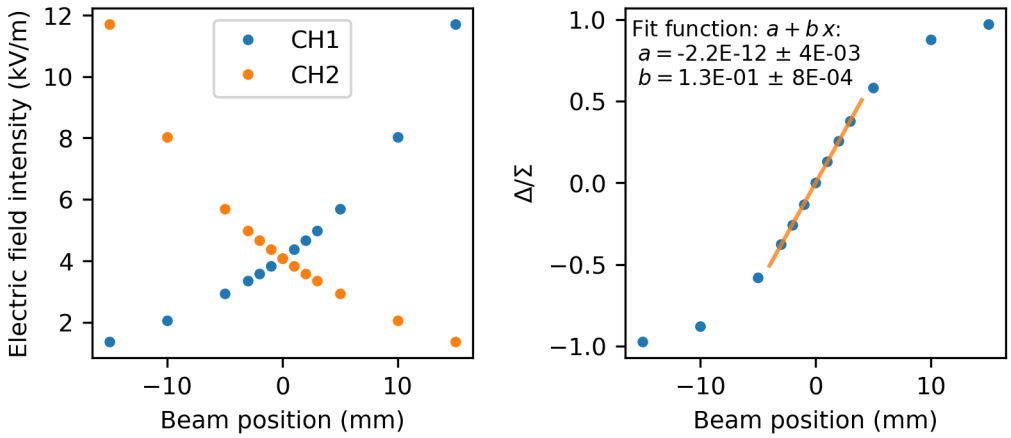

Figure 3.12: On the left, the RMS electric field emitted from the radiator measured at the test point shown in Fig. 3.11 (a). The signal from the second radiator is deduced by geometry. On the right, the Δ/Σ quantity calculated from the simulation results for a beam displacement of ± 15 mm. The linear fit in the region of ± 3 mm displacement is also reported.

a Gaussian longitudinal charge distribution. Secondly, waveguide ports, used to observe the generated electromagnetic waves, must be parallel to one of

the simulation domain boundary planes. Therefore, they cannot be used to evaluate the overall field exiting from the radiator surface as it is not parallel to one of the axes. Solutions for both of these problems were studied and are described below.

A method to evaluate non-Gaussian bunches

Even though the CST wakefield solver uses only bunches with a Gaussian longitudinal charge distribution, the model's transfer function can be calculated using signal-processing theory. Let us consider the simulation of a complex model like the one described in Section 3.3.2. The simulation can be seen as a system that transforms the time-varying beam current into an electromagnetic field that is probed in a point of space at a given time. The system in question is linear, as the superposition principle is valid, and it is also time-invariant, as the response does not change if the stimulus is applied with a delay. Therefore, the simulated model can be treated as a Linear Time-Invariant (LTI) system.

In an LTI system, the output signal in the time domain is a convolution of the system's impulse response with the input signal, and the convolution is defined as

$$h(t) * I(t) = \int_{-\infty}^{\infty} h(t-\tau) I(t) d\tau \tag{3.9}$$

where $h(t)$ is the system's impulse response and $I(t)$ is the input signal. In the frequency domain, the convolution simplifies to a product of the transfer function $H(f)$ and the input signal spectrum. A flowchart of this process is shown in Fig. 3.13. The frequency domain representation of a continuous time-varying signal is usually obtained using the Fourier transform. For the beam current and the probe field signal this operation is automatically provided by CST.

This method works in two steps: first, the system transfer function is calculated; second, the convolution of the transfer function with an arbitrary beam shape is computed. This process assumes that the original Gaussian pulse used to calculate the impulse response is significantly shorter than the arbitrary function that is convolved later.

To benchmark this method, two simulations of the model described in Section 3.3.2 were carried out with a 1 ps and 2 ps long Gaussian beams. The simulation bandwidth was 100 GHz. First, the results of the simulation of the 1 ps beam were used to calculate the three-dimensional transfer function that represents the the electric field components (measured at the probe) as a

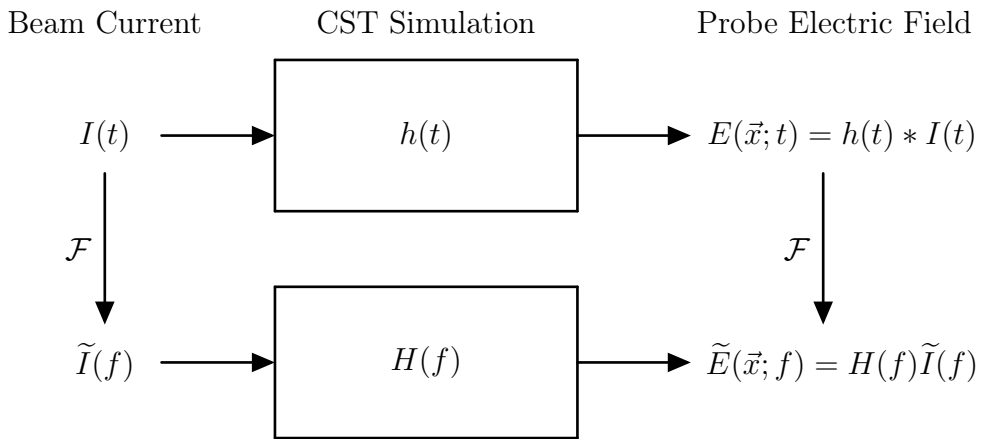

Figure 3.13: Flowchart of an LTI system simulation. The beam current input (left) is used to compute the electric field at a probe position (right) via the system impulse response. The passage between time and frequency domain is possible using the direct Fourier transform $\mathcal{F}$ and its inverse form.

function of the beam current. The field probe used is placed 10 mm above the centre of the radiator output surface in the ChDR emission direction. Secondly, the convolution of the transfer functions with the beam-current spectrum of the 2 ps simulated beam can be computed to obtain the response to a longer bunch. Figure 3.14 shows the electric field components at the probe position obtained from the 2 ps CST simulation and calculated using the convolution method. A good level of agreement is reached in the y and z component, while a noticeable difference is visible in the x field component. However, the field magnitude in the x component is significantly reduced compared to the other components, as the signal-noise ratio is reduced.

Transferring the results within the simulations

As discussed previously, the simulation volume is critical in modelling the design of this device. However, the simulation can actually be split into two separate parts. The core of the simulation is the ChDR and DR production in the first part of the radiator. After that, the radiation fronts propagate in the radiator body similarly to inside a loaded waveguide. Therefore, the simulation process can be divided in two smaller simulations:

1. Simulate with wakefield solver the beam interaction with the radiator surface, and sample the electric and magnetic fields after a short propagation space inside the radiator. The sampled fields are exported to text

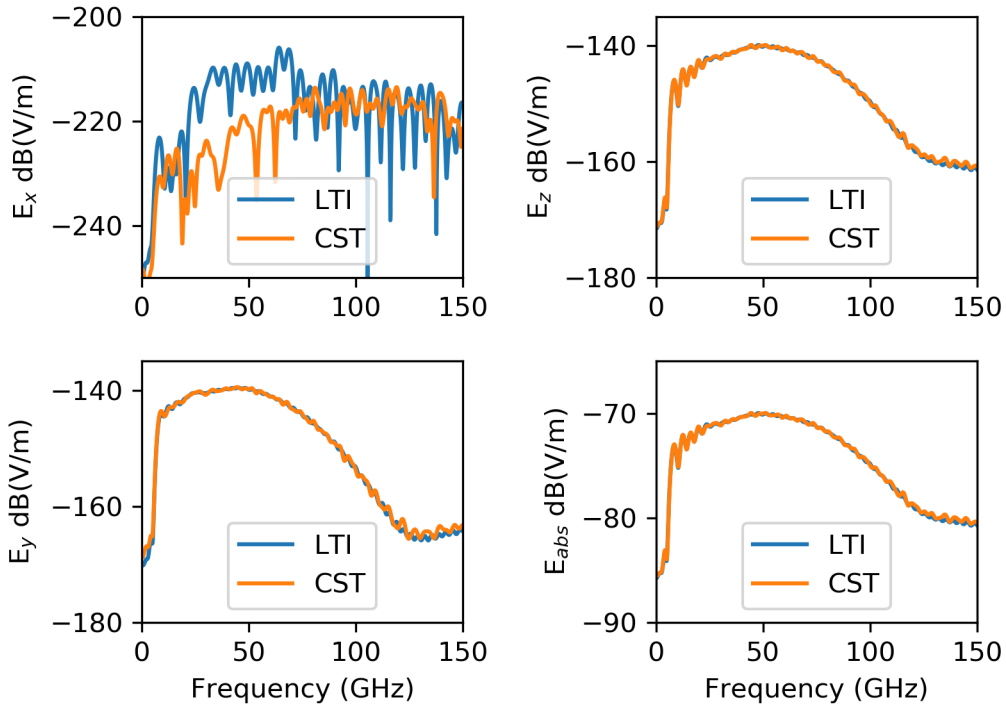

Figure 3.14: Electric field components in a point of the space calculated by means of a 3D simulation (CST) and using the convolution method (LTI). In both cases, the same 100 pC 2 ps Gaussian beam profile was used to run the full CST simulation and as input of the convolution method.

files.

2. Import the fields in a separate time-domain simulation that will simulate the propagation of the field through the radiator.

This approach is particularly advantageous. First, any simulation code can be used to simulate the beam-material interaction (step 1.). Secondly, if the shape of the radiator is modified, but the area exposed to the beam does not change, there is no need to run the first simulation again.

This procedure was successfully implemented by means of export and import of the electric and magnetic fields to ASCII files. However, this experience showed that to avoid the creation of artifacts, a very fine and uniform spatial sampling of the fields recorded at the exit of the first step in the simulation 1 is essential.

Although these initial studies were successful in simple geometries with uniform meshing, it is not possible to extend this approach to models with a more complicated geometry (e.g. circular) while retaining the uniform meshing. To

accomplish this with complicated geometries, it is necessary to get access to the mesh cells coordinates, which is not possible via the CST front-end. Further studies are planned in the future, in particular with the goal of using the IW2D [112] code to simulate the beam-material interaction and then evaluate the propagation through the radiator. These studies showed that overcoming the limitations of commercial simulation codes is possible, however it requires to access the source code, that is not freely available to the user.

3.4 Test in air

3.4.1 Experimental setup

The test device was installed in the CLEAR facility at CERN [113], in the so-called in-air test stand [114]. A high-energy electron beam was produced in the CLEAR linac, and sent towards the end of the beamline where it exited into air through a thin metal window. The beam travels in air for approximately two metres before encountering the beam dump. This space was used to install the test device on translation stages remotely controllable with micron resolution. The transverse position of the device could be scanned around the beam in both the transverse directions independently over a span of 25 mm. By doing so, there was no need to modify the beam trajectory to carry out the tests. The achievable beam parameters that can be produced at CLEAR are reported in Table 3.2.

The installed test device can be seen in Fig. 3.15. The window through which the beam exits the vacuum chamber is on the left-hand side. The beam proceeds through the white ring, which is an Integrating Current Trans-

Parameter	Value
Beam energy	60 - 220 MeV
Bunch charge	10 pC - 2 nC
Bunch length	1 – 4 ps
Bunch frequency	1.5 GHz
RF frequency	3.0 GHz
Number of bunches	1 - 200
Beam repetition rate	0.83 – 10 Hz
RMS energy spread	< 0.2 %

Table 3.2: Beam parameters achievable at the CLEAR facility [113].

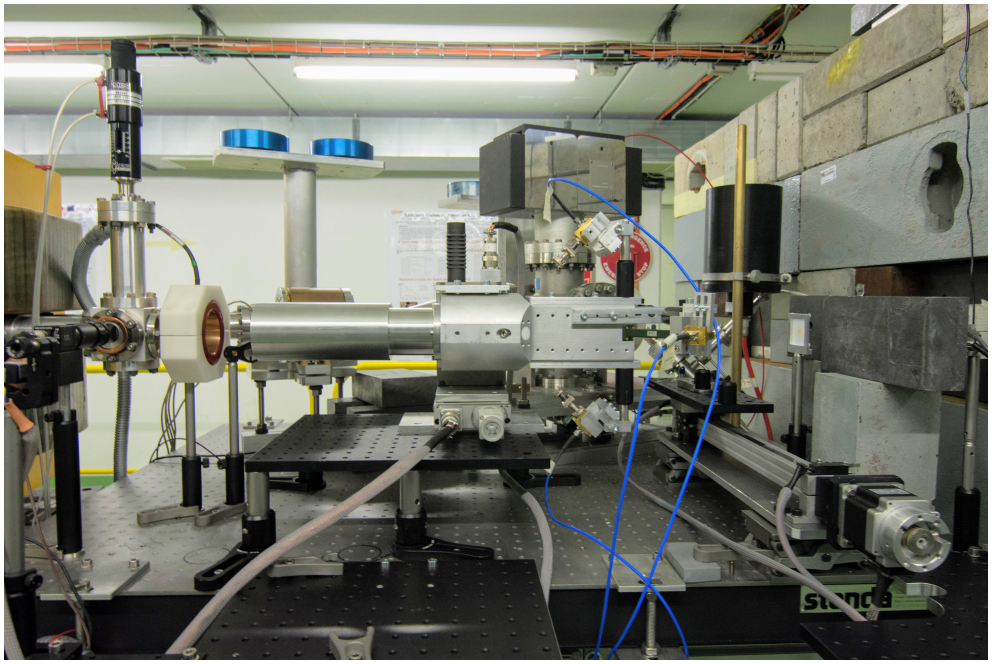

Figure 3.15: The test device installed in the CLEAR in-air test stand. The beam exits the vacuum chamber on the left and passes through the white Integrating Current Transformer. It passes through the test device and reaches the lead and concrete beam dump on the right after hitting the small white screen. The blue cables connect the RF detectors to the signal acquisition chain. In the centre, the translation stage is visible.

former [115] that measures the charge of each bunch train. Then the beam traverses the test device, hits the white beam screen on the right-hand side of the figure and is finally dumped on the lead and concrete absorber. The components installed in-air are aligned using an alignment laser.

The electromagnetic field produced by the test device was measured using zero-bias RF Schottky diode detectors. The advantages of such detectors include their relative simplicity and being fitted with a waveguide input and a coaxial output. Detailed characterisation of these detectors will be presented in Section 3.4.2.

In order to maximise the frequency range accessible during the experiment, two pairs of RF diodes working in different frequency bands were chosen for the horizontal and vertical planes as reported in Table 3.3. The detection was carried out in the Ka band (26.5-40 GHz) in the horizontal plane, and in the V band (50-75 GHz) in the vertical plane. In the horizontal plane, both the RF diodes were of the same model. On the other hand, in the vertical plane, one diode detected the full band (DXP15-SPFW0), while the other was narrow

Plane	Diode model	Frequency band
Horiz.	Millitech DXP28-SPFW0	Ka band (26.5-40 GHz)
Vert.	Millitech DXP15-SPFW0 Millitech DXP15-SNNW0	V band (50-75 GHz)

Table 3.3: RF diode detectors specifications.

band (DXP15-SNNW0). The implications of this difference for the output signal will be discussed later.

Some preliminary tests immediately showed that the RF diodes easily saturate with the high peak power produced by the ChDR radiators of the test device, making them unusable for precise measurements. Therefore, to prevent saturation, the horn antennas initially installed in front of the diodes were removed, and a waveguide attenuator was added in front of the Ka-band diodes installed on the horizontal plane of the test device. The attenuation was adapted according to the beam charge in the range from 10 to 30 dB. Suitable waveguide attenuators were not available for the RF diodes installed in the vertical plane and a standard waveguide was used instead. The waveguide equipment installed in front of the RF diodes acted as highpass filters. In the horizontal plane only frequencies above the 21 GHz cut-off frequency of a WR28 waveguide could reach the diodes. Similarly, in the vertical plane, only frequencies above the 39.9 GHz cut-off frequency of a WR15 waveguide reached the diodes.

The signal detection and acquisition chain is presented in Fig. 3.16 for the Ka- and V-band implementations. The signal from each Ka-band RF detector was sent via a short cable to an amplifier placed under the test stand to shield it from background radiation. The amplified signal was then sent via a long coaxial cable to a fast oscilloscope located outside the accelerator tunnel. No amplifier was used for the V-band detectors and their signal was acquired directly by the same oscilloscope.

The dual-channel amplifier used was custom made for an earlier project. Before using it for the ChDR application, the amplifier was characterised in-situ using a portable 20 GHz bandwidth Vector Network Analyser. The measurements showed a bandwidth of 1.3 GHz and a gain of 13.9 dB on one channel and 1.2 GHz bandwidth and 14.3 dB gain on the other channel. A high-resolution, fast-sampling and remotely controllable oscilloscope was used to acquire the data. Depending on the test, it was set to 12 bit resolution and

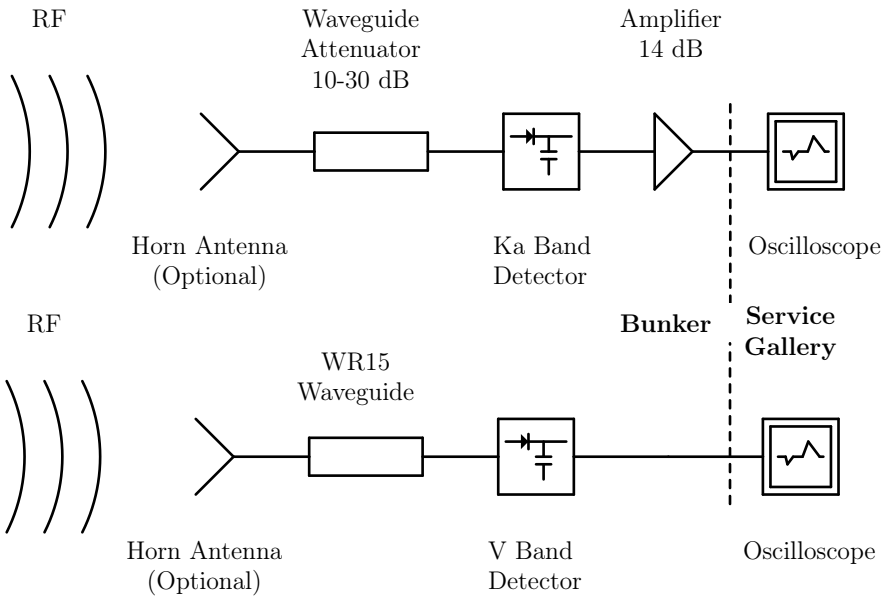

Figure 3.16: Schematic representation of the ChDR signal detection used for the experiments. The Ka-band acquisition system used for the horizontal plane is represented on the top. The V-band acquisition for the vertical plane is drawn on the bottom.

4 GHz analog bandwidth, or 8 bit resolution and 6 GHz analog bandwidth.

3.4.2 RF Schottky-diode detectors

The electromagnetic radiation produced by the test device was measured using commercial zero-bias RF detectors based on Schottky diodes that rectify the incoming RF wave, providing a signal proportional to the incident power. Such detectors are often employed to measure the power of Continuous Wave (CW) RF signals but can also be used to measure short pulses provided that the pulse length is considerably shorter than the detector rise time. RF diodes already available at CERN from other projects were used for characterising the test device at CLEAR. The sensors operating in the Ka band were tested with a 40 GHz synthesizer but it was not possible to measure the detectors working in the V band as no suitable test instrument was available.

To test the Ka-band RF diodes, an HP83642 40 GHz synthesizer was used. An HP R281A adapter connected the 2.4 mm coaxial output of the synthesizer to the detector waveguide input. The synthesizer produced 5 μs-long RF pulses every 19 μs with the desired frequency and power. The diode output voltage was acquired with the oscilloscope described in Section 3.4.1. Figure 3.17 shows

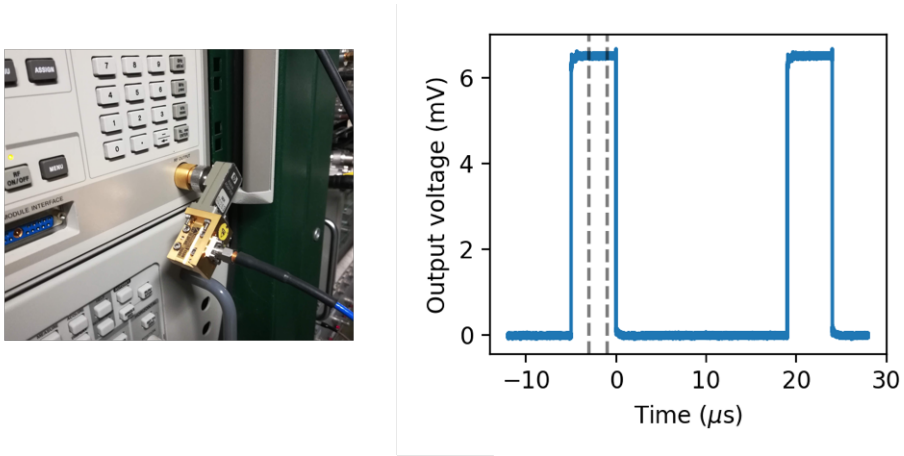

Figure 3.17: An RF diode installed on the synthesizer for calibration (left) and a typical diode output signal during calibration (right). Only the region between the dashed lines is taken into account to evaluate the average voltage output. The rise and fall of the pulse are discarded, as it is not possible to assess to which extent these are determined by the diode or the synthesizer. Additional details on the response of Schottky diodes to fast transients are given in Section 3.4.5.

the test setup and a typical diode output voltage. The signal was averaged over 50 acquisitions directly on the oscilloscope before saving the trace. The number of averaged acquisitions was determined empirically to achieve the maximum measurement noise reduction while being able to carry out the characterisation of both diodes in a single day.

The synthesizer and the oscilloscope were remotely controlled via GPIB [116] and LXI [117] commands respectively from a remote computer using a custom script which set the power and frequency, sweeping the frequency between 26 and 40 GHz in steps of 1 GHz and the power between -14 and 3 dBm[2] in steps of 1 dBm. The diode output voltage was calculated as the average voltage in a 2 μs window after the initial transients. The considered window is marked by the two vertical bars in Fig. 3.17.

The response of an ideal RF diode detector based on a Schottky diode is well known from simple equivalent circuit models [118]. At low power levels, the response is linear with the input power. This regime is called the 'square law region' as the voltage output is proportional to the square of the input voltage. For the detectors used at CLEAR, the linear region extends up to input power of -10 dBm [119] (0.1 mW). With higher input power, the response

[2]The dBm is a common RF power unit expressed in decibels and normalised to 1 mW. For reference, 0 dBm = 1 mW, and -10 dBm = 0.1 mW.

becomes non linear. After an initial transition, the device enters a nonlinear region where the output voltage is proportional to the square root of the input power. These two regions are called the 'transition region' and the 'linear region' (as the output voltage is linear with the input voltage). At very high input power the diodes saturate and eventually they might be permanently damaged.

The calibration results are shown in Fig. 3.18. The tested RF diodes' response is linear up to input power of 0.1 mW, or -10 dBm, indicated by the dashed line agreeing with what is advertised by the manufacturer. Increasing the input power, the response becomes nonlinear and more frequency dependent. This is particularly visible in the right plot of Fig. 3.18 at the operating band edge frequencies of 26 and 40 GHz, where the response kinks when surpassing 0.1 mW input power. A smoother response at the center of the frequency operating band is found, that likely depends on optimisations performed in the device design.

The RF diode averaged response was calculated to identify the linear and non-linear working regions and the transition region between them. For each input power level, the mean and standard error of the mean of the acquired responses were computed and are shown in Figure 3.19. A linear and square root function were fitted to the data in the respective working regions. The

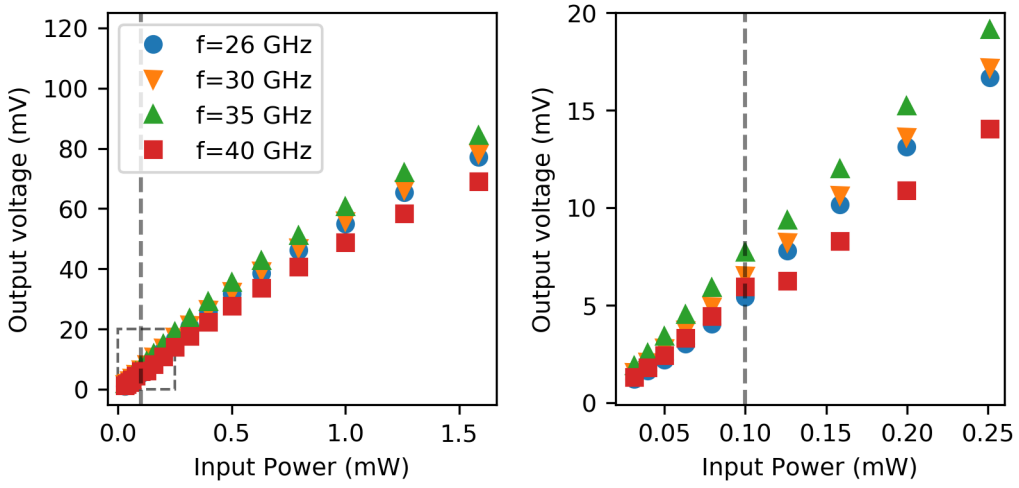

Figure 3.18: Diode response to the CW RF input produced by the synthesizer. The vertical dashed line indicates the linearity limit of 0.1 W indicated by the manufacturer. The response at different input frequencies is shown. The left plot shows the full tested range. The dashed box shows the reduced data range shown in the right plot.

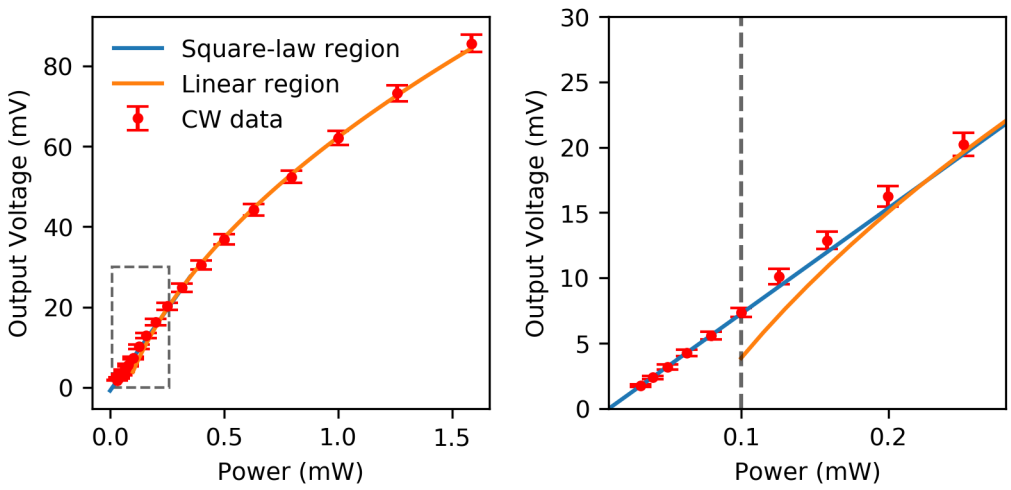

Figure 3.19: Tested Schottky-diode average response to CW RF input from the synthesizer. The vertical dashed line delimits the linear region. The left plot shows the full tested range, while the right plot zooms on the low input power range indicated by the dashed box. The bars represent the standard error of the mean output voltage at each input power.

linear region is on the left-hand side of the plot. The transition region can be seen between approximately 0.1-0.3 mW (-10 and -6 dBm) input power. The linear fit was calculated for input power < 0.1 mW. Statistical analysis showed that by extending this linear behaviour to higher input power, the residual error on the fit is below 5% up to 0.4 mW.

After preliminary tests, the signals sent to the diodes were attenuated to avoid saturation. For the results presented in this work, the diode output voltage never exceeded 15 mV, so it can be assumed that the diodes worked in their linear region. Unfortunately, no reference in literature was found for characterisation of Schottky diode detectors with short RF pulses. However, in this work the diode detector response is assumed to be linear for the power levels produced by the ChDR.

3.4.3 Beam position response for single bunch beam

The primary goal of the tests was to assess whether ChDR emission can be used to measure the transverse position of an electron beam. For this purpose, an electron beam with energy exceeding 200 MeV, a bunch charge between 10 and 200 pC and a bunch length of 2 ps was used. Slight variations of these parameters were anticipated due to the varying bunch charge which was

recorded shot-by-shot. The beam was kept at a constant transverse position, and the test device was moved around it by motorized translation stages.

A beam consisting of a single bunch was used to test the device response with two values of the beam charge and over two different position ranges. Table 3.4 shows the parameters of the four tests. A comparison of the spanned position range in the different tests is presented in Fig. 3.20.

Dataset name	Charge (pC)	Position scan range
coarse scan	35 ± 7	25 mm
fine scan	37 ± 7	4.5 mm
finest scan	41 ± 7	2.5 mm
fine scan low charge	12.6 ± 1.9	4.5 mm
100μm low charge	$10 - 15$ (est.)	1.5 mm

Table 3.4: Parameters of the tests with a single bunch beam. The charge for the dataset '100μm low charge' was not recorded, but the settings of the preceding dataset were retained. It can therefore be assumed that the charge was between 10 and 15 pC per bunch.

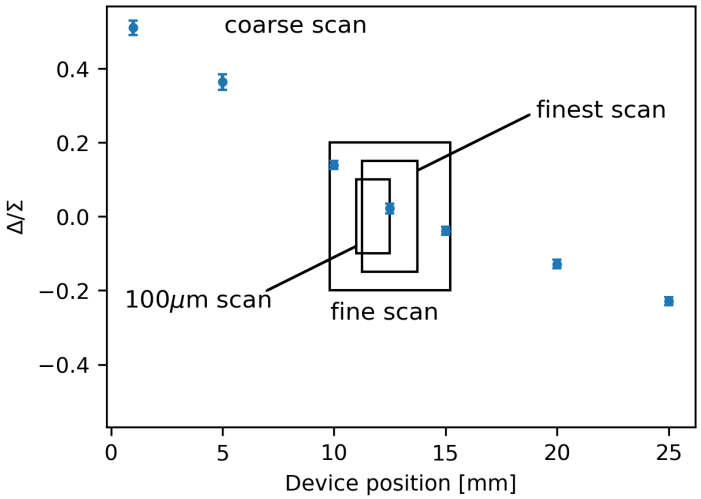

Figure 3.20: Comparison of the translation stage position range for different datasets. The 'coarse scan' dataset spans over the whole translation stage range of 25 mm. The displayed data were processed with method 2 (presented later).

Data acquisition was controlled remotely via custom python scripts interfacing the CERN accelerator control system via pyJAPC [120], setting the accelerator parameters, controlling the translation stages, and managing the oscilloscope.

The large amount of data produced was saved locally on the oscilloscope

and later copied to the CERN infrastructure for processing using the following procedure:

1. The oscilloscope saves the recoded data at each beam passage to four comma-separated value files, one per channel. The files are timestamped using the oscilloscope's local time accurate to the second. At the same time, the beam charge and readings of other diagnostic devices, such as the beam screen images, are stored in the CERN infrastructure by the CLEAR acquisition system.

2. All the data are copied to a common location. The oscilloscope files are opened one by one, and one Pandas [121] DataFrame per scope channel is assembled. Each of them contains the oscilloscope trace matched to its timestamp and the translation stages position. The timestamp is used to match the beam charge measured at that time.

3. The data are then saved to a new single DataFrame creating a single event structure. At each 'event', i.e. each beam passage, a common timestamp is used for the four oscilloscope traces, beam charge and translation-stage position.

4. For the signals of the Ka-band detectors the amplifier gain and baseline are removed.

Throughout this process, the data quality was assessed and the events where the oscilloscope was saturated or the acquisition was faulty were eliminated. Typically, for each translation stage position, 50 events were acquired. If some event was deleted during the processing, the reduction of the number of samples was taken into account in the analysis. An example of the signal produced by the ChDR emission picked up by a diode detector is presented in Fig. 3.21.

A number of processing algorithms were tested and the ones found to be the most satisfactory are:

Method 1: upsample, align and average. Each trace is upsampled five times and the signal peaks are aligned for all events recorded at the same translation-stage position. The events are then averaged and a smaller time window of the signal is selected. The standard deviation of the windowed signal is calculated for both channels in the same plane. The quantity Δ/Σ is then calculated using the standard-deviation values. This method produces a single measurement per translation position

stage. Therefore, a statistical error on the Δ/Σ cannot be calculated in this case.

Method 2: upsample and align. The Method 1 procedure is followed but the signals are not averaged. Therefore, one value of Δ/Σ is produced per event.

Method 3: data windowing only. Each oscilloscope trace is windowed. The data are used to calculate the standard deviation and the Δ/Σ of each event.

All applied processing methods assume that the beam does not move during the measurement. Although the beam position monitoring was not available during these tests, it is likely that only limited drifts occurred as the measurements were taken during the night and the acquisition of each dataset takes $\sim$ 10 minutes, limiting the possible effect of thermal drifts of the accelerator. Furthermore, it is assumed that the detector response is linear and that the bunch-charge variation affects both detectors in the same way.

The device was installed and aligned to the reference laser of the test stand with the best accuracy possible. The translation stage was set such that the 12.5 mm position corresponds to the laser in the center of the beampipe. Assuming that the reference laser and the beam are aligned, the 12.5 mm position corresponds to the quantity $\Delta/\Sigma = 0$.

The results of the three processing methods for the 'fine scan' dataset are shown in Fig. 3.22 together with a linear fit. The fit parameters are reported in the first row of Table 3.5. The derived beam position sensitivity is consistent

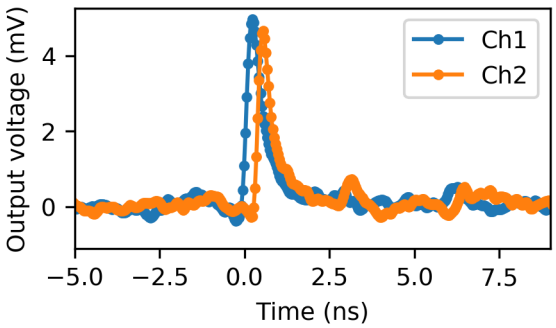

Figure 3.21: The output signal of the Ka band diode detectors installed for the horizontal plane. The amplifier gain and baseline were removed. Some minor reflections due to the cable connections are visible, e.g. on channel 2 after 2.5 ns. The solid dots mark the oscilloscope sampling points.

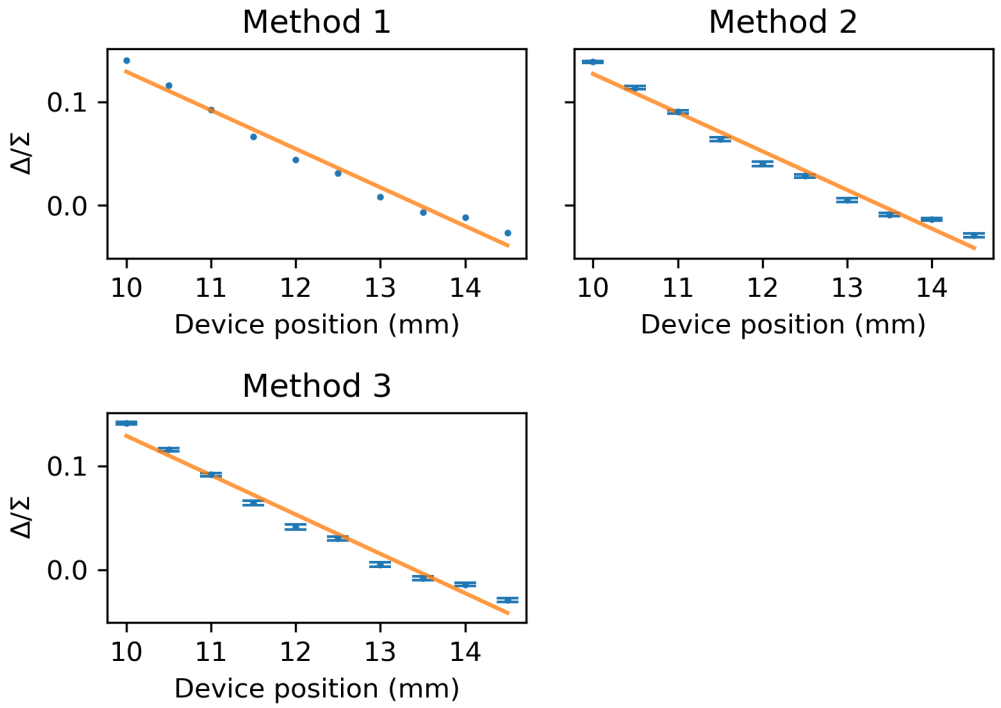

Figure 3.22: Comparison of the different processing methods together with the linear fit for the 'fine scan' dataset. The fitting parameters are reported in Table 3.5. The error bars represent the standard error of the mean of the response measured at each position.

for all processing methods. The average Δ/Σ sensitivity to the beam position is $(3.8 \pm 0.5) \times 10^{-2}$ mm^{-1} where the uncertainty is conservatively estimated using the Root Sum Square (RSS) of the uncertainties calculated individually for the three methods.

The same methods were applied to all available datasets, and the results are reported in Table 3.5. As before, the methods are consistent within the same dataset. Figure 3.23 shows the method 2 results for most datasets. The 'coarse scan' dataset is not shown as over the large 25 mm range the response is not linear, as expected from theory. The Δ/Σ differences between the examined datasets can be explained by the device response not being properly linear in different position ranges. The linearity of the data fitted with a straight line are evaluated by mean of the reduced χ^2. The reduced χ^2 cannot be calculated for Method 1, as this method does not provide an uncertainty on the Δ/Σ values. Datasets acquired on reduced position ranges exhibit a good linearity, the most evident is the '100 μm scan' dataset that presents reduced χ^2 of the order of 1 over a 1.5 mm range. Increasing the sampled position

Dataset	Parameter	Method 1	Method 2	Method 3
fine scan	Slope ($\times 10^{-2}$/mm)	-3.7 ± 0.2	-3.8 ± 0.2	-3.9 ± 0.2
	Intercept	0.50 ± 0.02	0.51 ± 0.02	0.51 ± 0.02
	χ^2/DF	N/A	35	29
finest scan	Slope ($\times 10^{-2}$/mm)	-3.40 ± 0.11	-3.42 ± 0.12	-3.45 ± 0.11
	Intercept	0.459 ± 0.014	0.458 ± 0.015	0.463 ± 0.014
	χ^2/DF	N/A	3.6	2.7
fine scan low charge	Slope ($\times 10^{-2}$/mm)	-3.4 ± 0.3	-3.4 ± 0.3	-3.5 ± 0.3
	Intercept	0.45 ± 0.04	0.46 ± 0.04	0.45 ± 0.04
	χ^2/DF	N/A	6.0	6.1
100μm scan low charge	Slope ($\times 10^{-2}$/mm)	-4.67 ± 0.19	-4.60 ± 0.19	-4.15 ± 0.15
	Intercept	0.58 ± 0.02	0.57 ± 0.02	0.55 ± 0.02
	χ^2/DF	N/A	1.23	0.98

Table 3.5: Linear fit parameters for the three processing methods for most of the datasets.

range to 2.5 mm, the 'finest scan' dataset also exhibits a good linearity. In the 5 mm range, the non-linearity of the data points starts to become evident. The two datasets 'fine scan' and 'fine scan low charge' present a poor agreement to the linear fit, although the 'fine scan low charge' features a visibly lower value of reduced χ^2.

The dataset '100μm scan low charge' showed an average sensitivity up to 30% larger than the other datasets. It was therefore compared to a subset of the other datasets over the same translation-stage position range. For all datasets, the Δ/Σ sensitivity increases when only the 11.0 to 12.5 mm translation-stage position range is analysed. Figure 3.24 shows how the results change for the full and reduced translation stage position ranges using the processing method 2 for two different datasets. To recalculate the fit, a shorter linear range was selected for the 'fine scan' and 'fine scan low charge' datasets. On the other hand, a range of 1.5 mm is too small for the '100 μm scan' dataset as it would use only three data points to estimate the two linear fit parameters. Instead, a range from 10.5 to 13 mm was used. Table 3.6 reports the linear fit parameters and the goodness of the fit is estimated using the reduced χ^2 value. In both the subsets of the 'fine scan' and 'fine scan low charge' datasets, the sensitivity

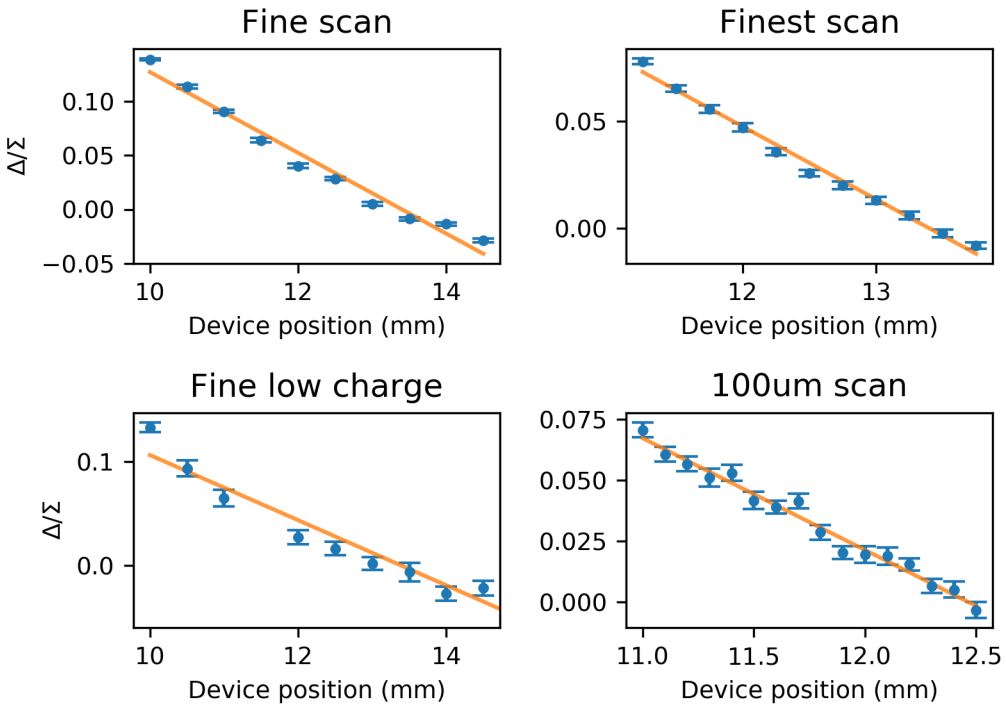

Figure 3.23: Each dataset processed with method 2

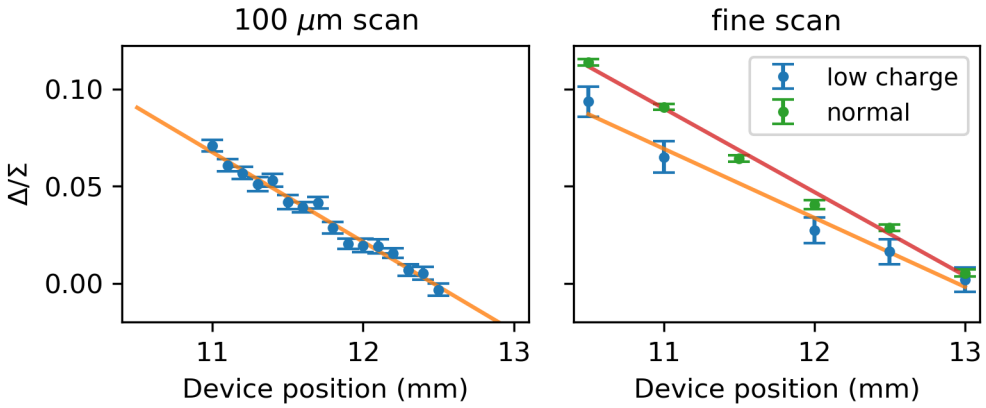

Figure 3.24: Comparison of the Δ/Σ sensitivity calculated for the '100μm scan' dataset (left) and the 'fine scan' and 'fine scan low charge' (right) for the same translation stage position range. The error on the data in the 'fine scan' dataset is visibly larger than in the others due to the reduced statistics. The fit parameters are reported in Table 3.6.

to the beam position increased compared to the full position range and remain within 30% difference also after considering the reduced datasets.

In conclusion, the test device was demonstrated to be sensitive to the transverse beam position, but some non-linearity was observed. It must be empha-

Dataset	Slope ($\times 10^{-2}$ mm^{-1})	Intercept	χ^2/DF
100μm scan low charge	-4.6 ± 0.19	0.57 ± 0.02	1.2
fine scan low charge	-3.6 ± 0.3	0.46 ± 0.04	0.7
fine scan	-4.30 ± 0.18	0.56 ± 0.02	5.1

Table 3.6: Linear fit parameters for three datasets in the position range 10.5-13 mm.

sised that the test device was designed to allow maximum flexibility during the tests and that the acquisition chain was not optimised. Sources of non ideality of the measurements are: the alignment of the test device with the beam, the alignment of the detection system with the radiators, the beam-charge fluctuations that can drive the RF diodes to the non-linear regime in some shots. Furthermore, simulations show that the response of the test device is not linear outside a zone close to the centre (see Fig. 3.12), and the width of this region depends on the operation conditions of the RF diodes.

3.4.4 Response to beam position, for bunch trains

For particle beams formed of a train of bunches, the test device produces a number of RF pulses corresponding to the number of bunches in the train. Each pulse is detected by the Schottky diodes as shown in Fig. 3.25.

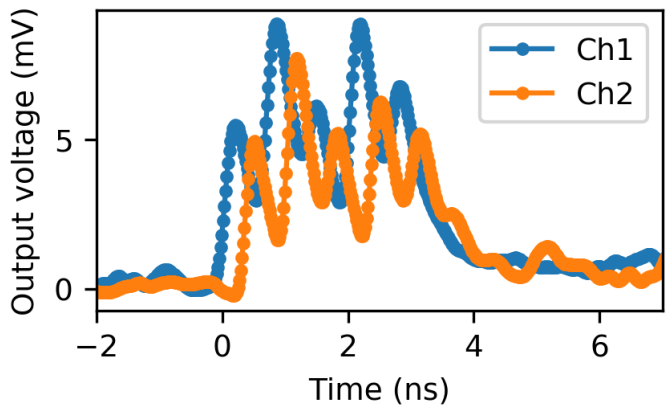

Figure 3.25: The signal produced by the Ka band diode detectors for a train of 5 bunches. After the five peaks corresponding to the bunches spaced by 0.66 ns, a sixth smaller peak is visible at 3.8 ns. This is a smaller less intense bunch that is occasionally produced due to an imperfect setting of the CLEAR injector laser system.

When detecting bunch trains, the RF diode fall time is significantly longer than the bunch spacing. Therefore, the signal of the subsequent bunch is affected by the preceding one. The relative amount of signal leakage depends on the intensities of the ChDR emitted by both bunches. This aspect of Schottky-diode detectors will be discussed in Section 3.4.5. The source of the difference in the ChDR emission intensity of different bunches is the different charge or position of the bunches along the train. This effect, combined with the slow fall time of the RF diodes, determines the signal observed in Fig. 3.25. Nevertheless, the three processing methods used for single-bunch beams can be applied to derive the average transverse position of the entire train.

Two datasets were collected with trains of five bunches and parameters as listed in Table 3.7.

Dataset name	Train charge (pC)	Position scan range
fine scan	115 ± 15	4.5 mm
finest scan	115 ± 12	2.5 mm

Table 3.7: Parameters of the tests using trains of five bunches. The error on the train charge is the standard deviation.

Figures 3.26 and 3.27 show both datasets processed using the three different methods already used for single-bunch analysis. The linear fit parameters are reported in Table 3.8. In both datasets, a non linearity is present at around the translation-stage position of 12 mm, but this is correlated with a momentary beam-charge reduction. It is possible that a temporary perturbation of the accelerator systems determined a beam production instability, that provokes a temporary charge reduction and energy modulation. This couples through dispersion, resulting in a beam displacement in the test stand. Such behaviour causes the calculated high values of reduced χ^2. Despite the momentary drift during these measurements, the sensitivities in these tests are within 15% of the response measured for single-bunch beams (see Table 3.5).

The signal produced by the diodes installed on the ChDR test device was compared to the signal of the Wall Current Monitor (WCM) installed upstream in the CLEAR beamline [122]. The WCM is a high-bandwidth monitor designed to measure each bunch individually. One of the oscilloscope channels was connected directly to the WCM through a long coaxial cable while the remaining channels were used to observe the signals from the Ka-band system. The monitors are compared in Fig. 3.28 for measurements of 3 and 20 bunches.

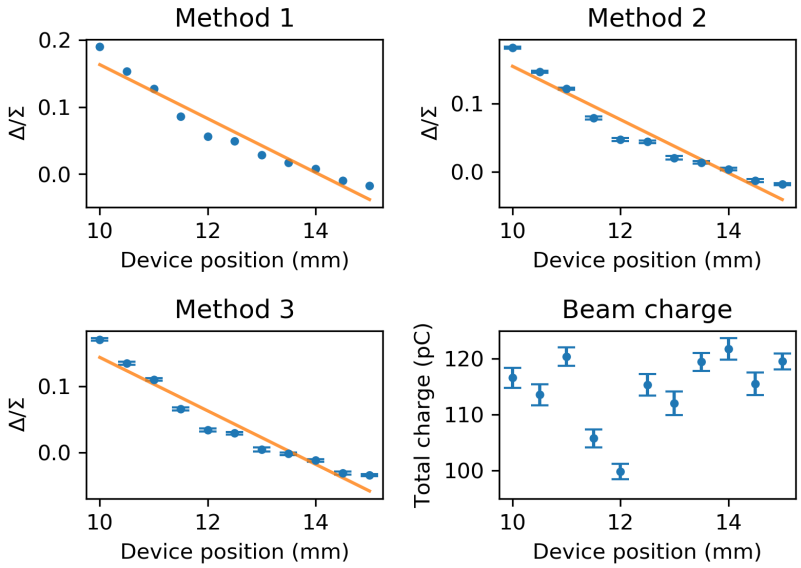

Figure 3.26: 'Fine scan' dataset processed by the three methods.

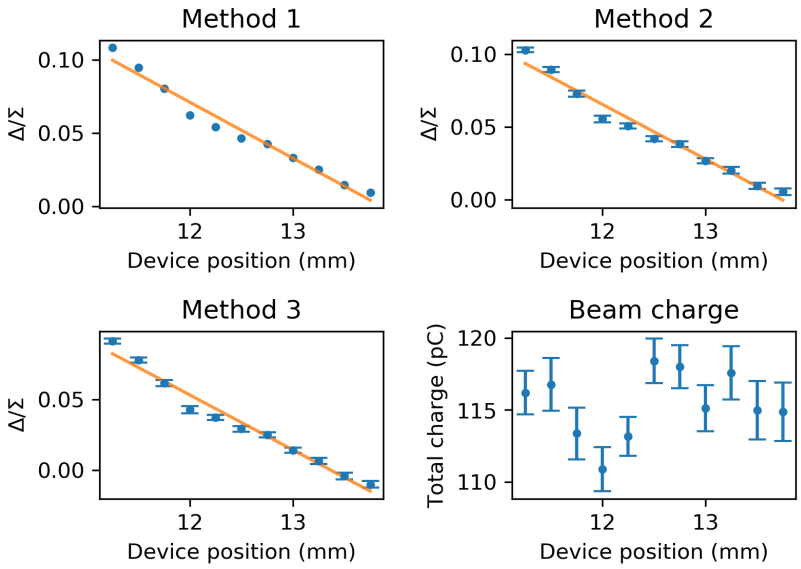

Figure 3.27: 'Finest scan' dataset processed by the three methods.

The comparison shows that the detected bunch spacing is the same in both cases, and it is consistent with the CLEAR RF frequency.

The WCM signal quality deteriorates after the first three bunches due to signal reflections and baseline drift caused by the bunch-to-bunch signal leakage that can be observed in longer trains (e.g. Fig. 3.28). However, the WCM has a faster fall time than the ChDR test device.

The comparison of the two instruments suggests that the bunched beam

Dataset	Parameter	Method 1	Method 2	Method 3
fine scan	Slope ($\times 10^{-2}$/mm)	-4.0 ± 0.3	-4.0 ± 0.3	-4.0 ± 0.3
	Intercept	0.57 ± 0.04	0.55 ± 0.04	0.56 ± 0.05
	χ^2/DF	-	101	83
finest scan	Slope ($\times 10^{-2}$/mm)	-3.8 ± 0.2	-3.9 ± 0.2	-4.0 ± 0.2
	Intercept	0.53 ± 0.03	0.56 ± 0.03	0.54 ± 0.03
	χ^2/DF	-	9.2	7.7

Table 3.8: Linear fit parameters for the three processing methods applied to both datasets.

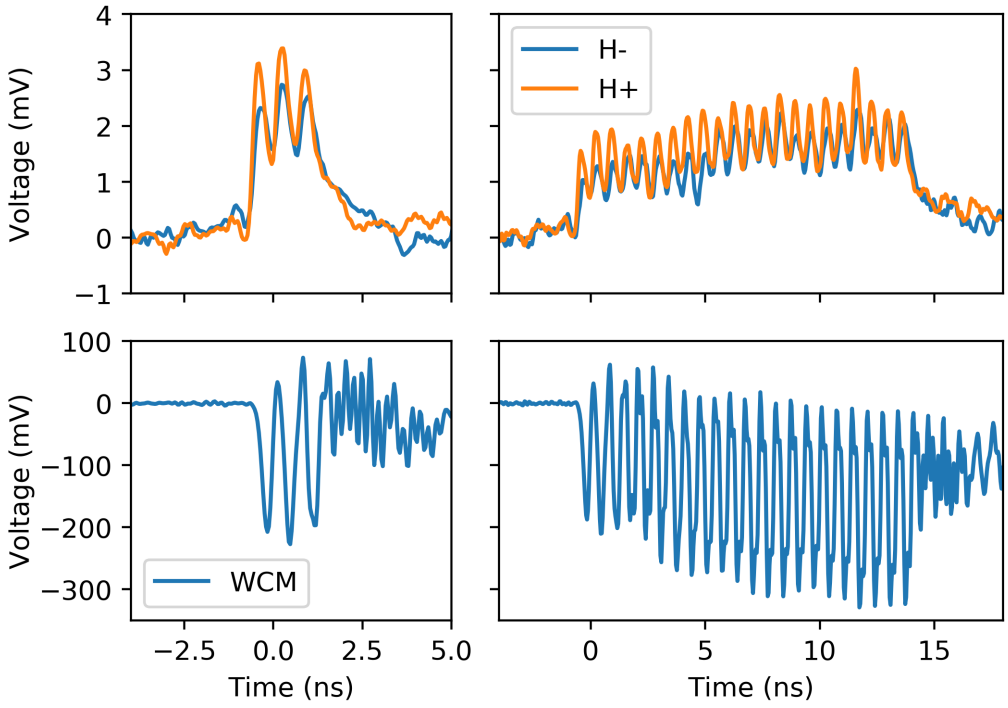

Figure 3.28: ChDR signal from the diode detectors in the horizontal plane (top) compared to the Wall Current Monitor signal (bottom). The plots on the left show the measurements of a train of three bunches, while the plots on the right show the measurements of a train of 20 bunches. The signal level difference between both monitors is due to their design, attenuators and cables. The diode-detector signals show the emission in the Ka-band of the two PTFE radiators installed in the horizontal plane (H+ and H-). The amplifier baseline was not subtracted, and the gain is compensated.

structure is correctly reproduced by the ChDR, but the fall time of the installed detection system is too slow to correctly distinguish individual bunches without polluting the signal of subsequent bunches. Therefore, the use of ChDR-based

beam-position detection is valid for bunch-by-bunch position measurement, provided that a detection capable to resolve the different bunches is used.

3.4.5 Limitations of the present setup

Schottky-diode-based RF detectors were chosen for this experiment for their flexibility and ease of use. Although they were successfully used in Section 3.4.3 and 3.4.4 to estimate the position dependence of the ChDR emission, they also highlighted some limitations such as their relatively slow fall time. No work describing the response of Schottky-diode detectors to short RF pulses has been found in the literature as not many applications use RF pulses of ps duration. Moreover, sources of such short pulses other than a particle beam are not widely available. For the work presented in this thesis, it is nevertheless interesting to discuss the diode response to a single-bunch beam and bunch trains. The data collected with the Ka-band diode detectors from the 'fine scan' dataset introduced in Section 3.4.3 were used to study the diode response.

Most RF detectors based on Schottky diodes exhibit a fall time significantly longer than their rise time. This is also the case for the RF detectors used in this experiment. The output voltage response to a single-bunch beam, and so to a single short RF pulse, is shown in Fig. 3.29.

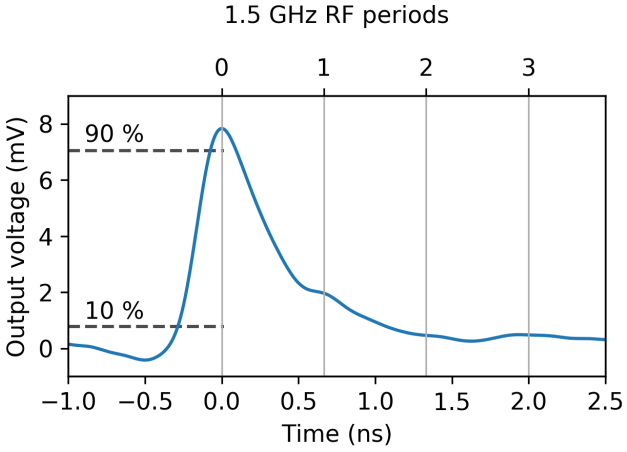

Figure 3.29: Response of one of the Ka band diode detectors to a single bunch. The RF periods of 666 ps are marked. In this acquisition, a shoulder is visible after one RF period. It is generated by the second, less populated bunch trailing the first one occurring due to an imperfect setting of the laser pulse picker system. The second bunch is not always present.

The rise time of a signal is commonly defined as the time necessary for the output signal to move from the 10% to 90% of the peak output voltage. The average measured rise time of the Ka-band detectors was 0.20 ± 0.05 ns, with the uncertainty being the sampling time of the oscilloscope. The fall time is harder to measure precisely, due to the intermittent presence of a spurious bunch trailing the main bunch (see Fig. 3.29). Neglecting this contribution the average fall time was 0.88 ± 0.05 ns.

It is possible that the real rise time was faster than measured, as the bandwidth of the complete acquisition system using long coaxial cables was neither measured nor corrected for. However, the fall time is longer than the accelerator RF period of 666 ps, resulting in signal leakage to the consequent bunches. The leakage affects mostly the next bunch. This is visible in Fig. 3.29, where the RF periods, and so the position of any next bunch, is marked. Small drifts of the rise and fall times of the order of 5% over 12 minutes were recorded, and can be attributed to thermal drifts [118]. Detailed studies of the acquisition system for multi-bunch beams and of the RF diode response exceed the scope of this work.

A method to compensate the signal leakage between the bunches was tested, based on iterative subtraction of the leaking signal tail. Starting from the first bunch, its falling edge is fitted to a negative exponential function and then subtracted from the trailing bunches. After this compensation process, the real peak height can be estimated. Figure 3.30 shows the first iterations of this process.

Peak differences up to 85% were present after the correction. These extreme cases correspond to two consecutive bunches with a large charge difference. In general, e.g. in the data shown in Fig. 3.30, the leakage causes a wrong estimation of the peak height of the order of 20-30%. However, the leakage is present in both diodes measuring opposite sides of the same plane and therefore its impact on the overall sensitivity is limited. Furthermore, this approach assumes that the RF diodes are linear to subtract the contribution of different bunches. This assumption might not always be correct.

In the presence of very long trains, another anomalous behaviour of the RF diodes was detected. A series of measurements was performed using a beam consisting of 80 bunches, scanning the beam position over a 5 mm range. The output voltage level of the RF diode is rather constant along the bunch train, and the output voltage does not suggest any saturation (see Fig. 3.31).

When computing the average train position with any of the three methods

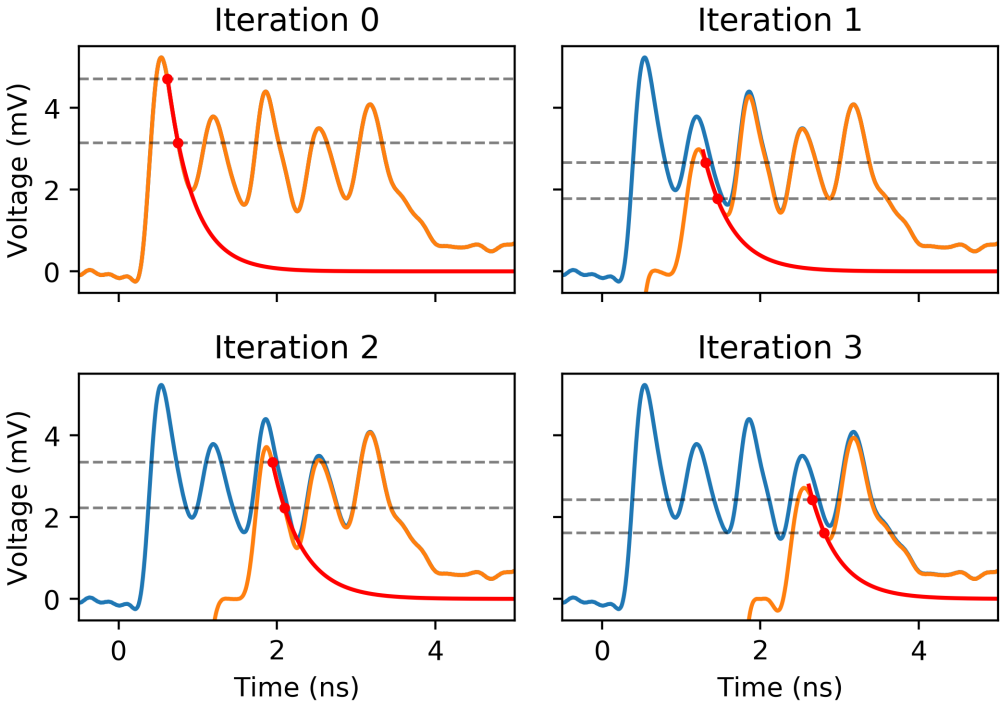

Figure 3.30: Successive iterations of the signal leakage compensation algorithm for a five bunch train. The blue trace shows the measured signal, the red one shows the negative exponential fit and the orange one shows the signal after subtracting the fit. The dashed horizontal lines delimit the fitted region, in this case between 90% and 60% of the peak voltage. At iteration 0 (top left), the blue and orange traces are overlapped, and the first peak is used for fitting the exponential decay. In iteration 1, the exponential decay fitted on the peak of the first bunch is subtracted from the signal, allowing to measure the correct height of the second peak (orange curve). The exponential decay is then fitted again onto the second peak after the correction, and it is used to move to the next iteration.

presented in Section 3.4.3, no position dependence is found. A more in-depth analysis windowing the diode signal to use only the first bunch, and then adding one bunch at a time in the train was carried out. The results of this analysis are shown in Fig. 3.32. On the left plot, the Δ/Σ curve is shown when considering only the first two bunches and the first 20. When only the first two bunches are considered, the response is linear. Conversely, when the first 20 bunches in the train are considered, the linearity and the position dependence are lost. The right plot of the figure shows a more systematic study of this behaviour. To estimate the linearity of the response the Pearson's r coefficient is plotted versus the number of considered bunches. The Pearson's r

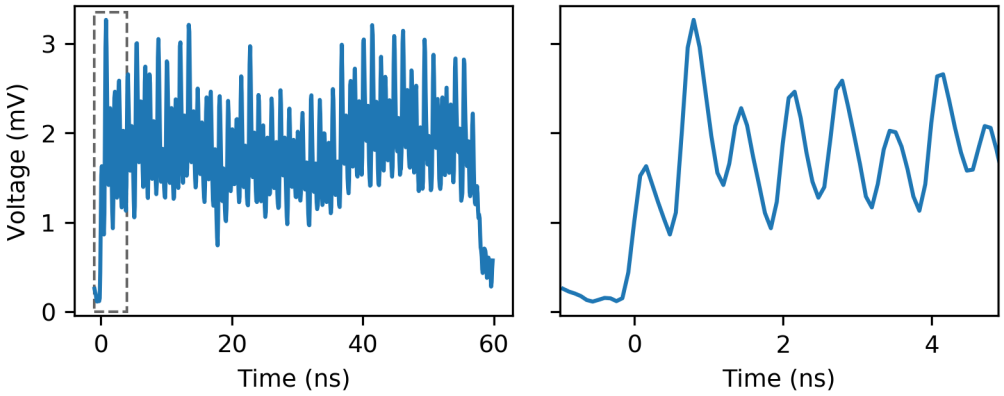

Figure 3.31: Recorded signal of a Ka band RF diode generated by a beam of 80 bunches. On the left the full signal is shown, while the region in the dashed box is presented on the right.

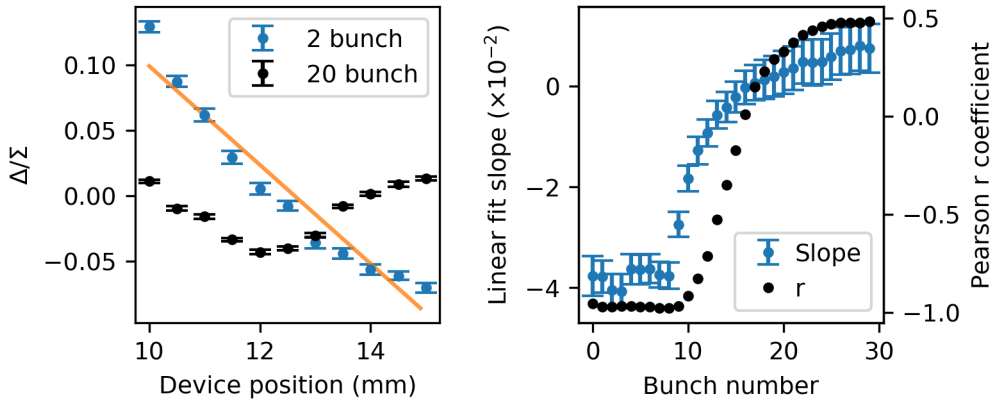

Figure 3.32: On the left, the beam position sensitivity measured for the first two and 20 bunches is shown. On the right, the slope of the linear fit and the Pearson r coefficient are presented as a function of the number of bunches considered.

correlation coefficient is a statistical indicator with values between -1 and $+1$ [123], where the ± 1 value indicate perfect linearity while zero is the absence of linear correlation. The slope of the linear fit is reported as well, although it is not meaningful for nonlinear data. This analysis shows that after the first 10 bunches, the correlation between the diode output and the beam position is lost. For the moment, there is no clear explanation of this behaviour, and additional studies involving RF detectors of known internal structure would be needed to investigate it further. These effects are also essentially undocumented in literature, as the population of users of these devices that detect

trains of ps-long RF pulses is extremely limited.

3.4.6 Directivity

Another interesting aspect when designing and testing a device of this kind is the directivity, i.e. the capability to selectively measure only the beam arriving from a given direction. In fact, the dielectric button BPM technology could be applied to any accelerator that features short bunches, including circular colliders. In such accelerators, two beams traverse the device in oppoite directions, and the signal generation in this case is investigated in this section. The properties of the radiation produced by the beam passing in the forward direction were explained previously. To test the radiation production from the beam traversing the device in the backward direction, the device was rotated by 180° about its vertical axis on the test stand. Figure 3.33 (a) shows the device after being reversed for this test. Only a single Ka-band diode detector was installed per plane. Due to the large number of electromagnetic reflections, produced mostly at the downstream beam dump, some copper foil was added for shielding the radiator and the RF detector. The diode detector output signal is shown in Fig. 3.33 (b). The immediate difference from the signal produced by the beam propagating in the forward direction (see e.g. Fig. 3.21

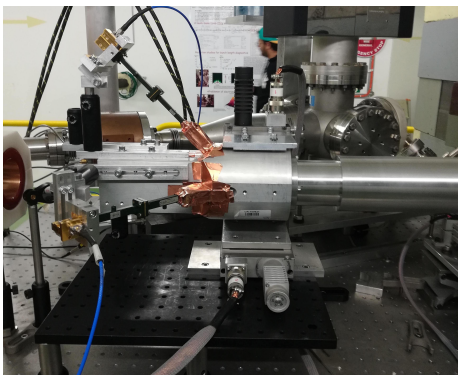

(a) Reversed device installed for testing

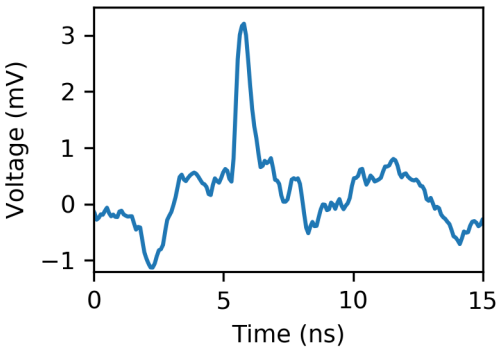

(b) Output signal

Figure 3.33: To test the directivity, the device was reversed as shown in (a). The beam is moving from left to right. The shielding copper foil connects the radiator output surfaces to the waveguide input of the detection system. Only one RF detector per plane was installed due to space constraints. The output signal of one of the RF detectors is shown in (b). The amplifier gain and baseline are compensated.

for comparison) is the presence of a rather large modulation of the baseline. This behaviour can be partially explained by the electromagnetic waves being reflected inside the copper foil due to its uneven section and shape. However, a part of this modulation is also generated by the ChDR emission itself and can be better understood through EM simulations.

A simulation was carried out with the slice model presented in Section 3.3.1. The results are presented in Fig. 3.34. The ChDR front is produced inside the radiator, but after travelling through the whole dielectric diameter it collides with the metal surface. The superposition of all internal reflections eventually escapes the radiator surface, together with the DR fronts that were generated, reflected and interfered inside the radiator. The emitted ChDR front is substantially more intense than the DR fronts that precede and trail it.

The tests revealed that, even with reverse orientation, the test device is emitting ChDR with reduced power and signal quality loss. Should this technology be used with the strict requirement of directivity, some major changes in the geometry need to be developed. The developed simulation model could be used to optimise the geometry and avoid the internal reflections. For example, developing a wedge-shaped radiator with two output surfaces.

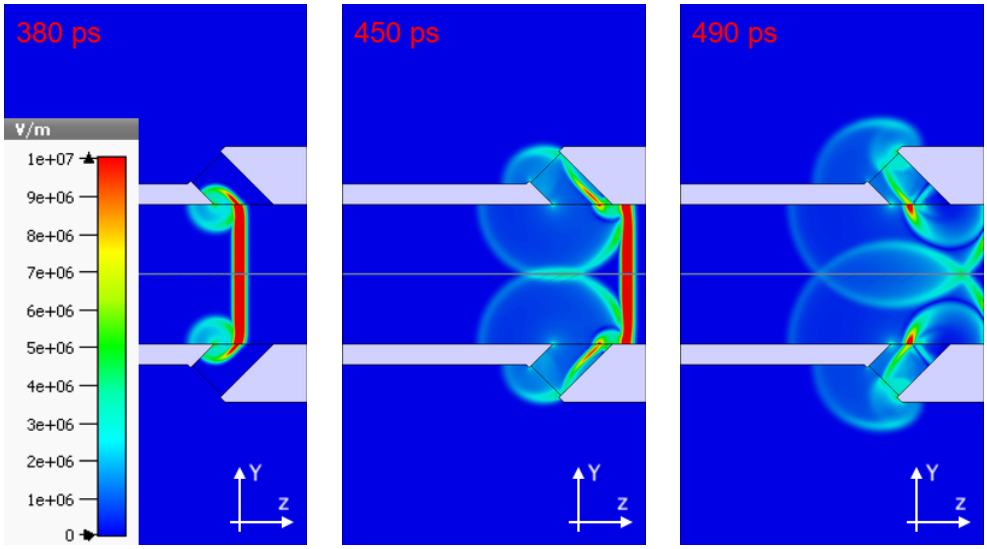

(a) t = 380 ps

(b) t = 450 ps

(c) t = 490 ps

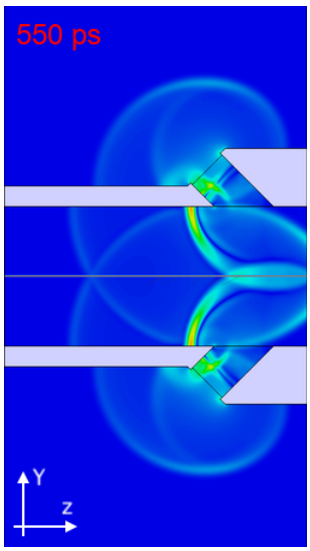

(d) t = 550 ps

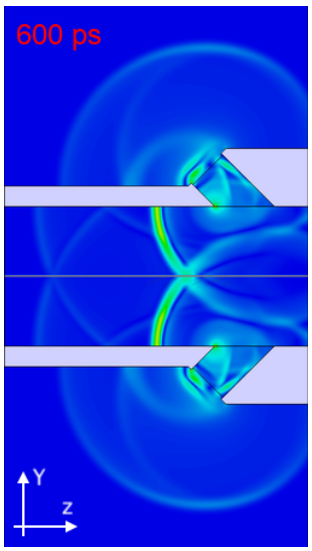

(e) t = 600 ps

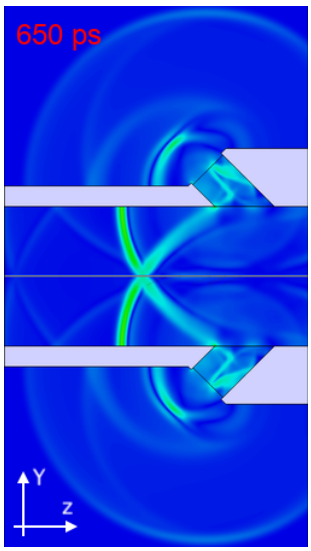

(f) t = 650 ps

Figure 3.34: The absolute value of the electric field generated as the beam passes through the test device with reversed orientation. The ChDR front is generated when the beam arrives (a), but then it collides with the edge of the radiator and the metal that surrounds it (b). This results in a series of internal reflections on the metal walls, visible in (c), (d), (e). The various DR and ChDR fronts eventually exit the radiator surface with the strongest front clearly visible in (f). The results are generated with the single slice model, using the parameters: a simulation bandwidth of 50 GHz, 20 mesh cells per wavelength, 100 pC and 5 ps long electron beam.

3.5 Tests with narrow-band diagnostics

Almost a year after the experiments described in Section 3.4, an additional measurement campaign was carried out to further study the use of ChDR for beam position measurement.

3.5.1 Experimental setup

The test device was reinstalled in the CLEAR in-air test stand on a motorized support. In this testing campaign, emission from a single radiator was analysed. The device was displaced around the beam over a 20 mm range. The measurements were done with one of the vertical radiators due to the superior beam stability in that plane. Any drifts in beam energy or magnet settings were immediately visible in the horizontal plane as they were amplified through horizontal dispersion. The beam position was nevertheless constantly monitored with an OTR screen placed before the beam dump. The installed device is shown in Fig. 3.35 and the detection system in Fig. 3.36.

A large horn antenna in the Ka band was installed in front of the radiator to couple the emitted signal to the detection system. A waveguide bandpass filter with a central frequency of 35.99 GHz and a passband of 1 GHz (model ELVA-1 BPF-28-35.99-1/20) connected the horn antenna to a waveguide network. The electromagnetic radiation was sent to the detector installed in a service gallery through a 15 m-long waveguide network. The filter proved to be necessary in preliminary tests to avoid deterioration of the broadband signal due to dispersion and reflections in the transmission chain. The waveguide network attenuated the signal by 11.5 dB.

In the service gallery, a precision rotary manual attenuator was placed at the end of the waveguide network before the RF diode. The diode output signal was amplified, when needed, with a 28 dB, 500 MHz amplifier before digitization.

The tests carried out with this setup present two main differences with respect to the tests described in Section 3.4:

1. Propagation along the long dispersive waveguide stretches the pulse before it arrives at the RF diode.

2. An attenuator in front of the RF diode makes it possible to maintain a constant input power. Therefore, the diode always works in the same region.

Figure 3.35: The test device reinstalled in the in-air test stand on movers visible in the centre. The beam exits the accelerator, going though the white Integrating Current Transformer on the left, traversing the test device and hitting the beam dump on the right. The radiator emission is captured by a horn antenna, and sent to the detection system through a waveguide network.

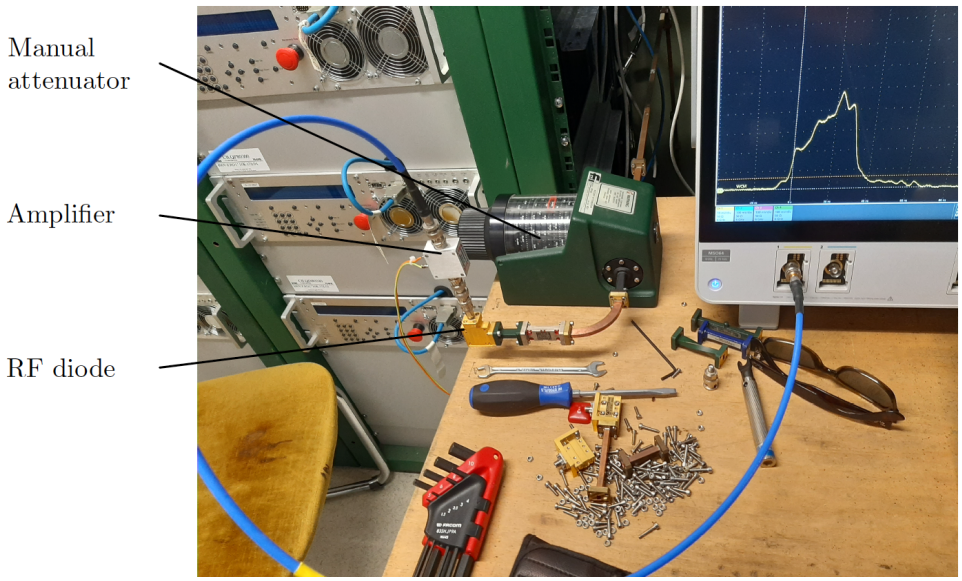

Figure 3.36: The detection setup in the service gallery. The electromagnetic radiation arrives via the waveguide exiting the rack, then it proceeds to the rotary attenuator, finally reaching the RF diode. The signal is digitised with an oscilloscope after being amplified, if necessary.

3.5.2 RF diode linearity

The RF diode response was tested with single bunches and trains containing up to five bunches, since in such conditions it is possible obtain a good transport through the accelerator and maintain the same bunch charge in each bunch of the train. Each bunch carried a charge of 200 pC and had a length of 2 ps.

In order to increase the radiated power, the test device was moved 20 mm off-centre with the beam passing 10 mm away from the radiator. The beam was maintained in a stable position during the measurements to obtain a constant ChDR production from the test device. The manual attenuator was adjusted in steps of 3 dB. For each setting, the average of 100 acquisitions was acquired 5 times. The averaging was carried out directly by the oscilloscope in order to reduce the noise.

The measurement results are compared in Fig. 3.37 to those obtained with the CW synthesizer set at 36 GHz, described in Section 3.4.2. First, it has to be noted that for a bunched beam no calibration of the absolute incident power is available. However, the attenuator settings allow for a correct relative scaling of the power between the different measured points. Secondly, for the ChDR generated by a bunched beam, two different operation regimes of the RF diode are reached. With a single bunch the diode remains in the transient regime, while for bunch trains of two or more bunches, the diode reaches the steady state regime. Hence, the measurements of a bunch train can be compared to

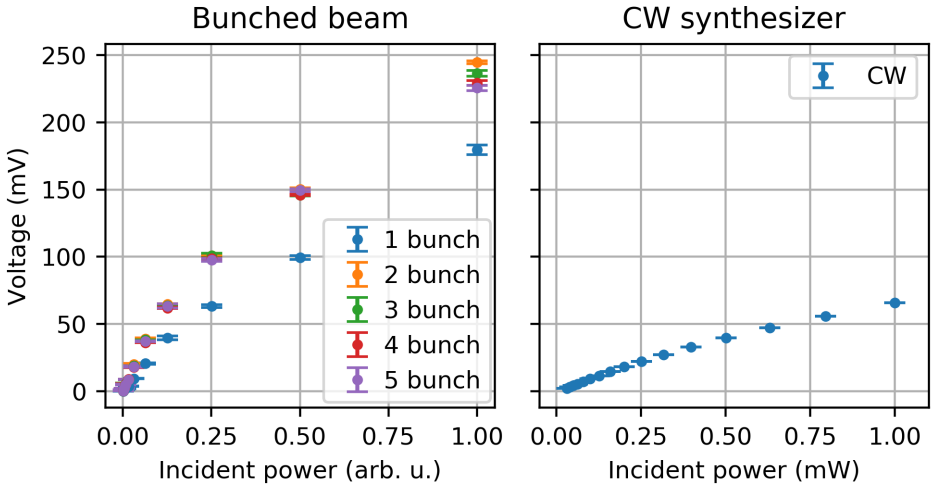

Figure 3.37: Diode output voltage as a function of the input power generated from ChDR (on the left), and from the CW synthesizer (on the right). The number of bunches is indicated in the legend.

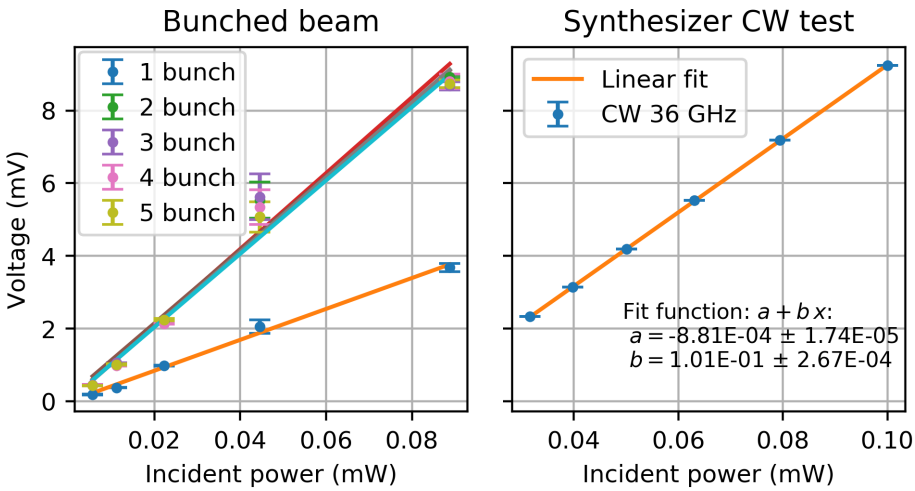

Figure 3.38: Diode output voltage for different levels of input power. The input power for bunched beam operation was deduced by cross-calibration with the CW source in the linear operation region.

those done with the CW synthesizer. The response exhibits the typical RF diode behaviour with the initial response linear with the input power which then becomes proportional to the square root of the input power.

Assuming that the the bandpass filter and the waveguide network stretched the ChDR generated by bunch trains enough to reach the RF diode steady-state regime, the diode's response can be compared to the CW synthesizer measurements. This hypothesis is supported by the fact that the response does not change regardless of the bunch-train length. During the cross-calibration procedure, the response to 5 bunch trains was assumed equal to the CW response. This yields a factor of 5.58 to be applied to the arbitrary input power scale in Fig. 3.37 to convert it to power in mW. Furthermore, this allows the diode response to be calibrated also for a single bunch. The cross-calibration results are shown in Fig. 3.38. The sensitivities calculated for bunch trains of various lengths and CW are presented in Table 3.9. The sensitivity to short pulses produced by a single bunch is 42.7 ± 1.9 mV/mW, i.e. less than half of that found for CW operation.

3.5.3 Response to beam charge

The test device response to a single bunch was measured in the charge range between 3 and 525 pC. The result of the measurement is shown in the left plot of Fig. 3.39. The goal was to perform the measurement of the emitted

Number of bunches	Intercept (mV)	Slope (mV/mW)
1	$(-0.8 \pm 8.6) \times 10^{-2}$	42.7 ± 1.9
2	$(2 \pm 39) \times 10^{-2}$	104 ± 8
3	$(1.2 \pm 4.4) \times 10^{-1}$	101 ± 9
4	$(2 \pm 34) \times 10^{-2}$	103 ± 7
5	$(2 \pm 20) \times 10^{-2}$	101.3 ± 5.5
CW	$(-88 \pm 2) \times 10^{-2}$	101.3 ± 0.3

Table 3.9: Linear fit parameters for Fig. 3.38. The slope is RF diode sensitivity under various test parameters.

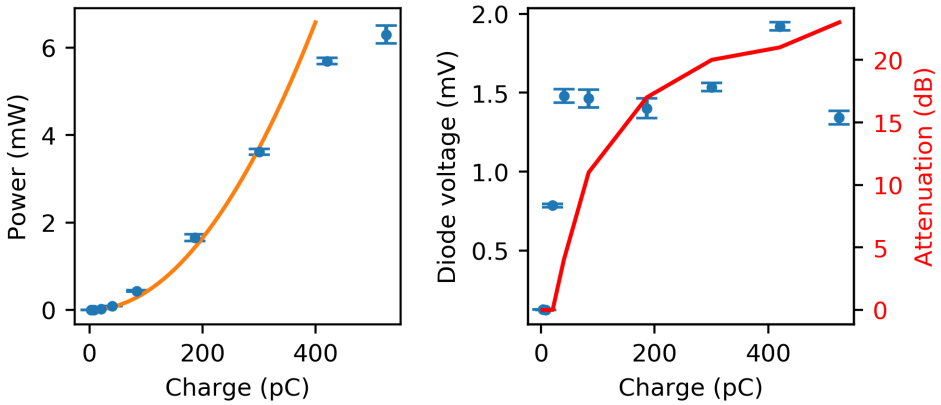

Figure 3.39: Left, measured emitted power depending on the single bunch charge. The fit with the quadratic curve is shown, representing the expected dependence for coherent radiation. The emitted power is measured by attenuating the input signal on the diode by a known factor, in order to keep a constant output voltage of 1.5 mV. This procedure ensures that the diode does not change the operation regime. The measured diode output voltage (in blue) and the manual attenuation settings (in red) are reported in the plot on the right-hand side.

power while keeping the diode detector working in a constant regime. To make sure that the diode works constantly in the same regime, the input power is reduced by mean of the attenuator, maintaining the output voltage at 1.5 mV. The radiated power can then be reconstructed by means of the diode output voltage and the attenuator setting. Constant output voltage was measured for bunch charges above 40 pC, as shown in the right-hand side of Fig. 3.39. For smaller bunch charges, the attenuator was set to zero, and the full radiated power was delivered to the diode.

The measured power production was fitted to a quadratic function $P = a\,q^2$, where q is the beam charge, as it is expected for coherent radiation production

in Equation 3.7. The obtained fit parameter is $(4.11 \pm 0.12) \times 10^{-5}$ mW/pC. The quadratic dependence is valid only for data points recorded with a charge below 400 pC. Above this charge, a saturation of the power production is recorded. It can be excluded that the saturation is related to the experimental setup as the beam position was stable and the input power on the diode was kept in the same regime also at charges above 400 pC. Conversely, it is likely that the charge increase caused a bunch elongation [124] which reduces the beam spectral power at high frequencies and therefore reduces ChDR production in the detected band. Unfortunately, no measurements of the bunch length were available for this dataset.

3.5.4 Response to beam position

Using the same procedure as for the charge scan, the vertical position of the test device was also varied while controlling the RF diode input power with an attenuator. The explored displacement from the beampipe centre ranged between -0.25 and 20.75 mm. The radiated power as a function of the beam position is shown in the left plot of Fig. 3.40. The recorded beam charge, the diode output voltage and the attenuator settings are shown in the right plot of the same figure.

The measured data can be used to derive the beam position sensitivity of

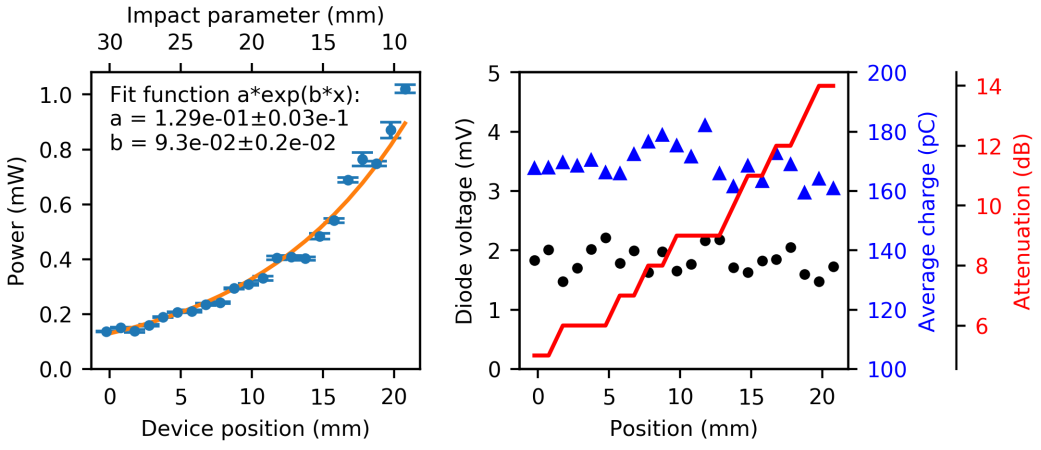

Figure 3.40: Left, measured radiated power as function of the beam position. The distance from the radiator is also reported on the top axis. An exponential fit is shown. Right, the experiment parameter for each data point. For each position, the charge (in blue), the diode output voltage (in black) and the attenuator settings (red solid line) are reported.

the test device. By fitting the data to an exponential function, the response of a second detection system for the opposite electrode can be extrapolated. The derived sensitivity is shown in Fig. 3.41 together with a linear fit over a 10 mm wide region around the device centre. The derived sensitivity in this range is 8.9×10^{-2} mm^{-1}, more than twice as much as in the previous tests. The comparison of the different tests is discussed later.

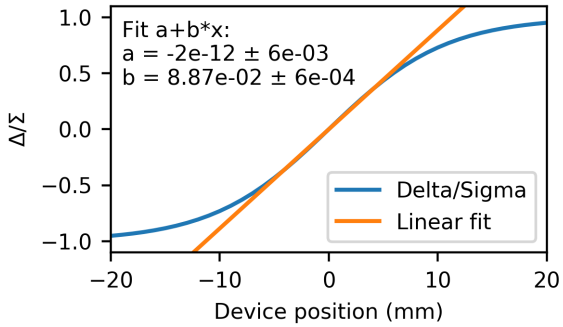

Figure 3.41: Δ/Σ response as function of the beam position, assuming that another radiator with identical response to the measured one is present on the opposite side of the device. The fit from the data in the left plot of Fig. 3.40 was used to calculate the response. The linear fit is performed on the curve in a range of ± 5 mm from the device centre.

3.6 Lessons learned

The tests at CLEAR showed that ChDR emission is a valid technique for beam position monitoring of ps-long bunches and that a radiator can be integrated into a beampipe. However, for the moment the tested design was not compatible with in-vacuum operation as the rapid degradation of PTFE in a radiation environment might compromise the vacuum tightness of the device [125]. The comparison of data, simulations and theory also suggest that improvements on all the three aspects are necessary to fully develop this technology.

The beam position sensitivity was tested with two different experimental setups for single-bunch beams.

The first setup used RF diodes placed in close proximity to the test device (Section 3.4). The beam position sensitivity of the test device over a range of 5 mm around the beampipe centre was tested. On average, a sensitivity of $(3.8 \pm 0.5) \times 10^{-2}$ mm^{-1} was measured, where the error on the measurement

is conservatively estimated by the RSS of the uncertainties of the fine datasets processed with the three different methods. In this range, the test device showed a linear response within the experimental errors over a small region around the centre of the test device, while, on the 5 mm range, nonlinearities become increasingly important. Further observations on the measurements with bunch trains showed that part of the nonlinear behaviour is correlated to brief charge fluctuations. The weak points of this system are the difficulty of alignment of the detector to the radiators, the fixed attenuation and the ps-long ChDR pulse that reach the detector, which is therefore used in the undocumented transient regime. However, this setup allowed substantial experience on ChDR emission and detection to be gained.

A second setup involved narrow-band detection placed outside of the radiation area (Section 3.5). A large horn antenna to capture the emitted ChDR was used, followed by narrowband filtering, a long waveguide network and a precision attenuator to characterise the ChDR emission while controlling the RF-diode detector operation. With this setup, the beam position sensitivity cannot be measured directly and has to be extrapolated by assuming that the identical system is placed on the opposite side of the test device. These tests resulted in a beam position sensitivity of $(8.87 \pm 0.06) \times 10^{-2}$ mm^{-1}.

Electromagnetic simulations were compared with the measurements, as shown in Fig. 3.42. A sensitivity of 13×10^{-2} mm^{-1} over a 6 mm range resulted from the simulations. The sensitivity in simulations is symmetric around the centre. This result represents the theoretical device sensitivity, assuming that the emitted field is uniform and well represented by the emission measured at the sampled point.

A number of considerations arise from the comparison of these results.

First, the CST simulations and the extrapolated sensitivity from the narrowband detection agree to within 30%, with a smaller measured sensitivity with respect to the simulations. In both cases, a single radiator is used, and the emission is considered after the propagation in vacuum a few cm away from the radiator output surface.

Secondly, the measured sensitivity with the two diodes installed inside the bunker is much reduced with respect to simulations and other measurements. It is also not symmetric and it is larger for positive beam displacements. The centred beam position was deduced as the position where $\Delta/\Sigma = 0$, which corresponds to the 13 mm position setting of the translation stage. Asymmetries in the measured response could be explained by unequal sensitivities of the

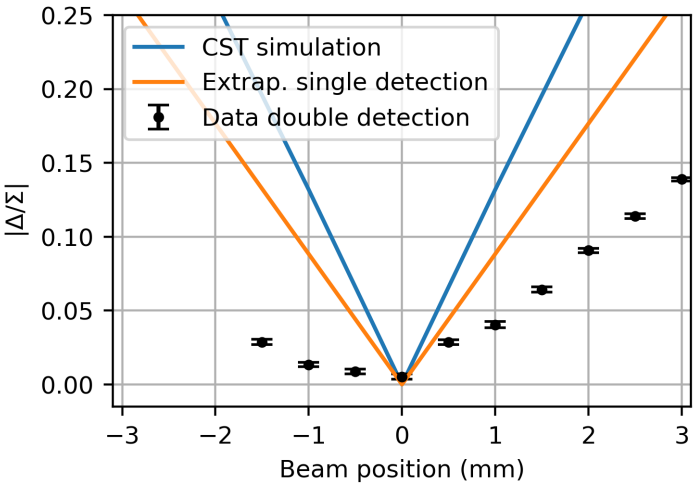

Figure 3.42: Comparison of the measured beam-position sensitivity with the CST simulations. The black data points ("Data double detection") show the measured data from the 'fine' dataset processed with Method 2 (see Section 3.4.3). The 0 mm beam position corresponds to the 13 mm position setting of the translation stages. The orange line is the extrapolated sensitivity from the measurements with the narrow-band detection ("Data single detection"). The blue line is the result of the CST simulations.

two RF diodes. A number of factors could cause this in the CLEAR setup, for instance unmatched amplifiers or detection-system misalignment (in this setup the alignment was complicated by the absence of horn antennas). The additional difference with the narrow-band detection system is that neither an active control on the signal attenuation is available, nor is the ChDR pulse is stretched before arriving at the RF diode.

The analytical PCA model is not sufficient to explain the measurements or the numerical simulations results. In fact, no analytical expression to estimate the radiated power is available for this complex geometry. Considering only ChDR emission from a surface (Eq. 3.6) is not sufficient, as the DR was shown to play an important role in the emitted radiation power, and the DR emission depends on the radiator edge shape. Therefore the control of the edge shape can be crucial for the device performance, and a larger development of the theoretical models is desirable to describe cylindrical geometries as well.

The comparison of the two measurement setups showed that the narrow-band detection gave a better agreement with the simulated values. Furthermore, the control of the diode input power and the band-pass filtering of the ChDR allow one to perform experiments under more controlled conditions. Al-

though the beam position sensitivity measured with this method is just an extrapolation, this detection system is the most promising of the tests conducted so far. In future tests detecting the radiation from two opposite radiators, it is desirable to directly couple the ChDR to a waveguide to limit the asymmetries arising from antenna misalignment.

Using the methods applied for single bunches, the sensitivity to short bunch trains was tested as well using the setup with two RF diodes. The average sensitivity to trains of five bunches was $(4 \pm 0.6) \times 10^{-2}$ mm^{-1}. The comparison with a high-bandwidth wall current monitor showed that the ChDR emission pattern follows the bunch structure. This suggests that the technique could be used for bunch-by-bunch position monitoring. However, due to limitations of the detection system, it was not possible to measure the exact position of each bunch independently, but only the average train position.

The next chapter discusses if the ChDR technology is suitable in the presence of both the electron and proton beams in the AWAKE experiment. If that is the case, a new instrument addressing all shortcomings of the test device would need to be designed.

Chapter 4

Proposal for an improved design

Chapter 3 showed that the ChDR emission can be used to detect the beam position of a relativistic charged-particle beam. In this chapter, the experience gained with the test device at CLEAR is extrapolated to the possible application of this technique at AWAKE by using electromagnetic simulations and scaling laws.

4.1 Coupling to the proton beam

The main difference between the test conditions at CLEAR and in the AWAKE beamline is the presence of the proton beam. Chapter 2 showed that carrying out the measurement at high-enough frequency is sufficient to detect the electron beam with reduced contribution from the protons. Using a design similar to the one tested at CLEAR exploits the inherent insensitivity of ChDR to low-frequency signals.

According to the PCA theory, electromagnetic radiation is produced on the surface of a dielectric radiator and then propagates through it. In the geometry examined in this work, the radiator is cylindrical and surrounded by metal. Therefore, the electromagnetic wave propagates de facto through a circular waveguide filled with the radiator dielectric material. The cutoff frequency of the fundamental mode of a dielectric-loaded circular waveguide is

$$f_c = \frac{1.8412c}{2\pi r}\frac{1}{\sqrt{\epsilon_r}} \tag{4.1}$$

where r is the waveguide radius, c the speed of light in vacuum and ϵ_r the relative permittivity of the dielectric material [74].

The prototype device tested at CLEAR featured PTFE radiators with a radius of 9 mm, resulting in a cutoff frequency of 6.74 GHz. Using the 3D model presented in Section 3.3.2, it is possible to simulate the response of the device to bunches of varying length and charge. Figure 4.1 shows the electric-field magnitude computed at the location indicated in Fig. 3.11 (a) when simulating proton and electron beams with parameters as in Table 4.1. It can be immediately noted that, even though the proton-beam electric field decreases at frequencies above 0.1 GHz, it is still higher than the electron beam field up to ∼1 GHz (see Fig. 2.6 for a comparison of the beam spectra).

The parameters of simulated beams were selected on the one hand to investigate the effect of the AWAKE proton beam on the device tested at CLEAR,

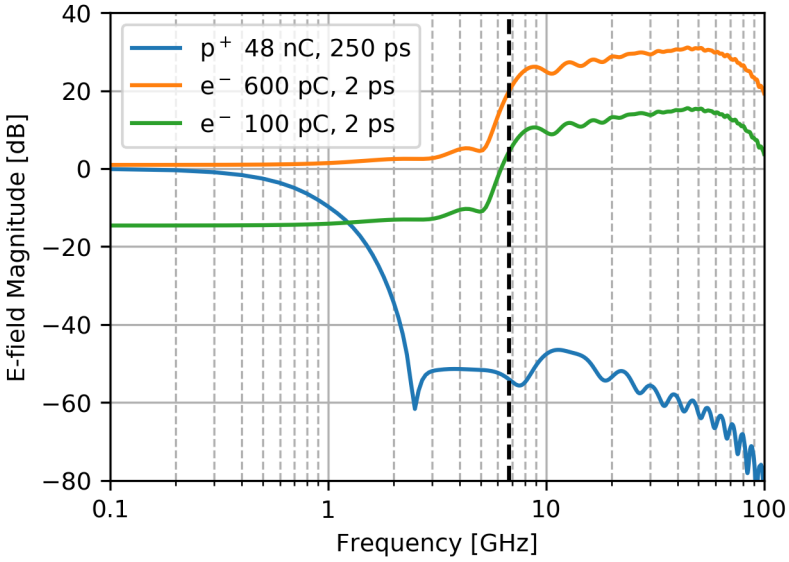

Figure 4.1: Electric field computed at a probe placed 1 cm above the radiator output surface. Spectra of various beams, as reported in Table 4.1, are shown. The vertical dashed line is the cutoff frequency of an 18-mm-diameter waveguide loaded with PTFE.

Name	Charge nC	σ ps
Proton beam	48	250
Electron beam	0.6	2
Electron beam	0.1	2

Table 4.1: Beam parameters used as baseline parameters for this study. See Table 2.2 for comparison with the AWAKE operational parameters.

and on the other hand to compare them with the CLEAR electron beam. In the case of AWAKE, bunch lengths up to 1 ps are used. However, the simulation results shown in Fig. 4.2 show that, up to 30 GHz, the ChDR emission is not strongly dependent on the simulated bunch length. Studying a 2 ps long bunch was preferred due to the reduced computing time required to complete the simulations.

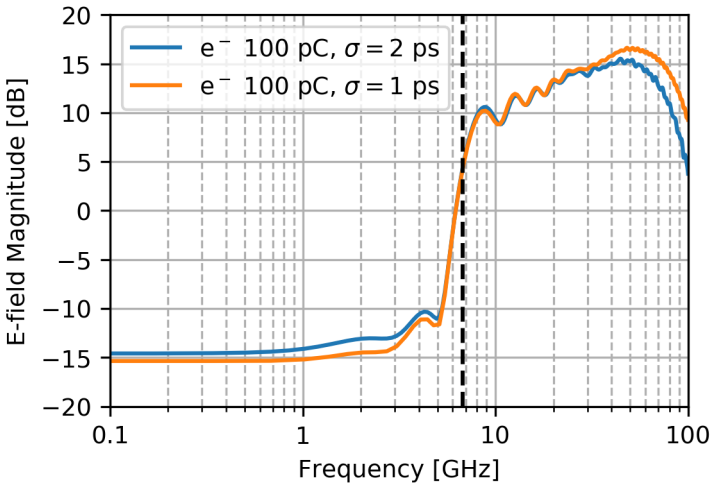

Figure 4.2: Comparison of the electric field spectrum emitted by 1 ps- and 2 ps-long electron bunch with a charge of 100 pC.

4.2 Lower-energy beams

The AWAKE facility uses a tenfold-lower electron-beam energy compared with CLEAR. Therefore, a different electron-bunch-field distribution is expected, as explained in Chapter 2. The relativistic beam parameters for both facilities are compared in Table 4.2. Although in AWAKE the β is still very close to 1, a simulation was performed to assess if the lower beam energy could affect the ChDR emission. The 3D model presented in Section 3.3.2 was simulated with a 2 ps-σ 100 pC electron beam. No appreciable difference in the field spectrum emission was observed, with the maximum differences smaller than 0.01 dB (i.e. 0.1%).

Accelerator	Energy	γ	β
CLEAR	200 MeV	392	0.999997
AWAKE	16 MeV	31	0.9995

Table 4.2: Relativistic electron beam parameters for AWAKE and CLEAR beams.

4.3 The design of a vacuum compatible radiator

Although the device tested at CLEAR would be sensitive to the electron-bunch position regardless of the proton-bunch presence, some modifications would be necessary before it could be installed in the AWAKE beam line. The test device is not compatible with Ultra-High Vacuum (UHV) and using PTFE in radioactive environments should be avoided due to its rapid degradation [125]. A different radiator material is therefore necessary, which would affect the BPM mechanical design because its permittivity would differ from that of PTFE. Two dielectrics were considered for a vacuum-compatible BPM installed in a radioactive environment: Fused Silica and Alumina 99.5%. Both change the emission angle of the radiator and the fundamental-mode cutoff frequency. The variation of the Cherenkov angle can be derived from Eq. 3.1, remembering that $n = \sqrt{\epsilon_r}$ for non-magnetic materials. As the material's relative permittivity increases, so does the Cherenkov angle, up to the maximum value of 90°. On the other hand, the radiator's cutoff frequency decreases if either the material permittivity, or the radiator radius increases (see Eq. 4.1). Figure 4.3 shows how the change of the radiator radius affects the radiated electric-field spectrum. The simulations were conducted using the model described in Section 3.3.2. Table 4.3 presents relevant parameters for the different materials considered.

Material	PTFE	Fused Silica	Alumina
Relative permittivity ϵ_r	2.1	3.8	9.6
Cherenkov angle θ_{Ch}	46°	59°	71°
Relative cutoff frequency $f_c/f_{\mathrm{c,vac}}$	0.69	0.51	0.32

Table 4.3: Relative permittivity of the materials considered for the radiator. The different Cherenkov angles and the fundamental-mode cutoff frequency are reported. The cutoff frequency is normalised to an equivalent evacuated circular waveguide.

Based on CERN's experience in realising vacuum-tight assemblies by brazing alumina to metal, the final material of choice is alumina. Compared with PTFE, alumina radiators have a cutoff frequency lower by a factor of 2.15. In order to reach a cutoff frequency in the order of 20 GHz, a 3 mm radiator diameter was selected. See Table 4.4 for a comparison with the cutoff frequency of PTFE radiators of different diameters. The inherent Cherenkov angle for alumina is 71°.

For an installation in the AWAKE beamline, it is convenient to design the radiators such that they are compatible with the existing BPM vacuum chambers. Such a 'dielectric button' consists of a cylindrical metal insert fitted with a vacuum flange. The cylinder is 44 mm long and has a diameter of 36 mm. The alumina radiator is inserted into the cylinder by welding a

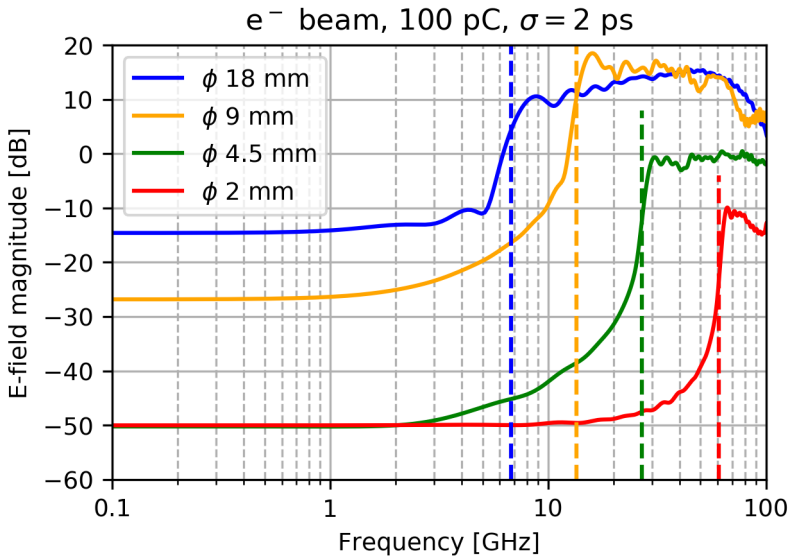

Figure 4.3: Comparison of the electric field vs frequency, measured 1 cm away from the centre of the radiator output surface produced with different radiator radii in a PTFE radiator (model described in Section 3.3.2). The coloured vertical dashed lines represent the fundamental mode cutoff frequency of an equivalent PTFE-loaded waveguide of the same diameter (the numerical values are reported in Table 4.4).

Diameter (mm)	18	9	4.5	3	2
f_c (GHz)	6.7	13.5	26.9	40.4	60.6

Table 4.4: Fundamental-mode cutoff frequencies for PTFE-loaded waveguides of different diameters.

metal collar brazed to the radiator. The cylinder dimensions allow one to accommodate radiators with diameters up to 15 mm, while retaining the 71° angle. Figure 4.4 shows an existing BPM vacuum chamber with the dielectric button inserted, and details of the button.

An alternative design option featuring an orthogonal radiator to the beampipe was also considered. This design with the radiator at 90° would provoke internal reflections which could result in signal deterioration, while offering a significantly simpler construction.

In general, the design is substantially more complicated than the CLEAR test device described in Chapter 3, which featured radiators with a diameter of 18 mm and an average length of 25 mm. In the AWAKE case, the diameter is reduced to 3 mm while the length is increased to 40 mm. While in the CLEAR test device the radiation fronts not propagating at the Cherenkov angle quickly reach the output surface with limited reflections, this is no longer true in the AWAKE design. Therefore, part of the radiation would be subjected to multi-

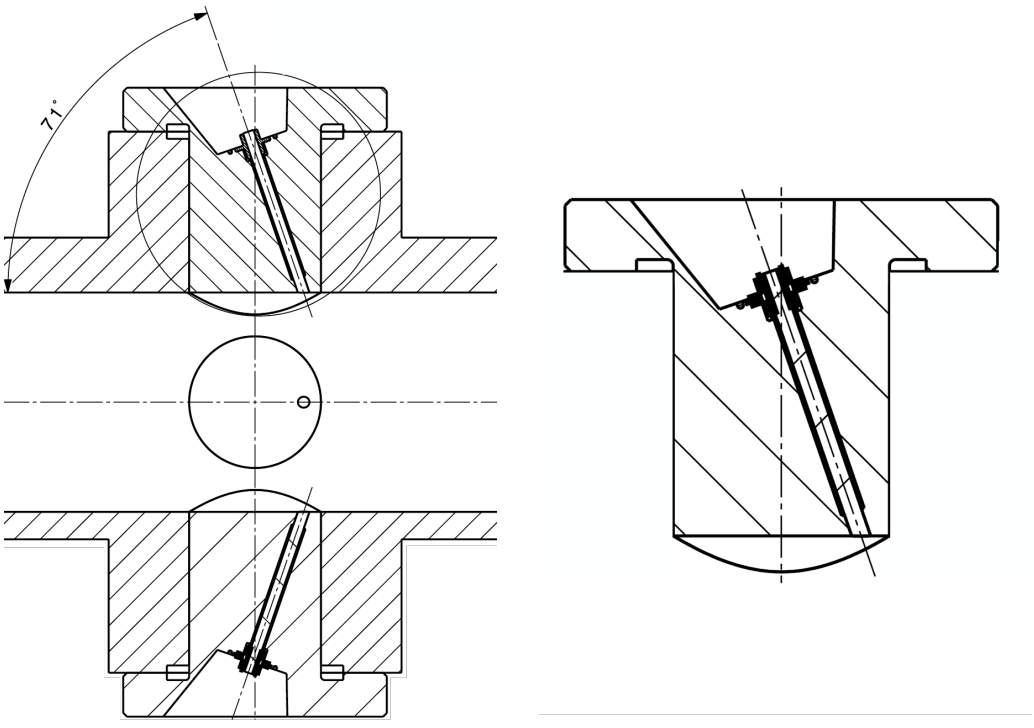

(a) BPM body (b) Button detail

Figure 4.4: Longitudinal section of the BPM vacuum chamber (on the left) and of the dielectric button (on the right). The beam direction is right to left. The design is preliminary.

ple reflections and eventually some would be reflected back into the beampipe. An additional complication is the increased electromagnetic-simulation complexity due to the longer radiator.

4.4 Radiator oriented at the Cherenkov angle

The design of a ChDR radiator oriented at the Cherenkov angle offers the simplest field-propagation dynamics. In fact, the ChDR front is not reflected inside the radiator as it propagates on axis. Conversely, the DR fronts are not emitted on axis, and therefore may be reflected during the propagation before reaching the exit surface.

A 3D electromagnetic model was created to simulate this configuration using an average radiator length of 7 mm. Although the radiator size for a real-life BPM would be in the order of 40 mm, a shorter radiator was simulated to reduce the computing power required. Furthermore, a heavily optimised meshing was necessary to limit the simulation complexity due to the relatively large mechanical dimensions. The approach was similar to what was done for the CLEAR test device in Section 3.4.3. Figure 4.5 shows the 3D model and its division into separate meshing regions. High resolution meshing of 20 cells per wavelength was used in regions 1, 5 and 6. A 100 pC, 2 ps-long electron bunch was used as an EM source.

The emitted electric field was computed for a probe placed 1 cm above the center of the output surface. The simulated cutoff frequency for a 3 mm diameter radiator matched the theoretical value of 19.11 GHz. Additional simulations were carried out to assess the effect of slight angle variations due to mechanical tolerances. This would be equivalent to a slight change of the dielectric constant of the radiator material. The comparison of the emitted spectrum for $\pm 1^\circ$ variations from the Cherenkov angle of 71° is shown in Fig. 4.6. In general, a discrepancy up to 1 dB is observed below the fundamental mode cutoff frequency and up to 0.2 dB above it.

Choosing a high dielectric constant material for the radiator is particularly favourable as the Cherenkov angle is not very sensitive to dielectric constant variations. For high-purity alumina (99.5%), the dielectric constant $\epsilon_r = 9.4$ results in a Cherenkov angle of 71°. Even rather large ϵ_r variations, for example $\epsilon_r = 9$ and $\epsilon_r = 10$ result in limited variations of the Cherenkov angle of 70.5° and 71.6°, respectively. This is reassuring for two reasons: first, it is not

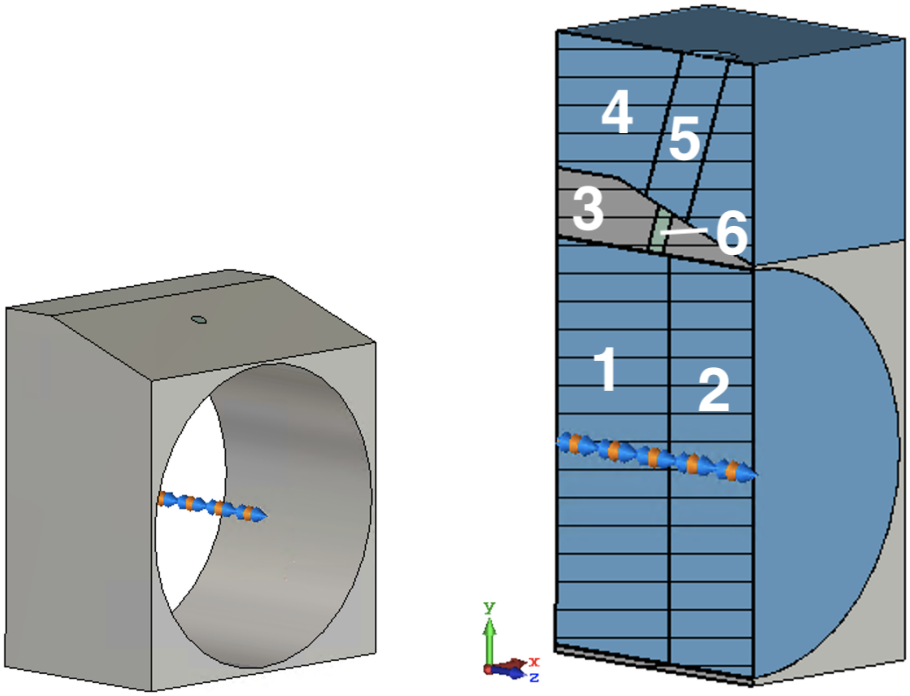

(a) Model overview (b) Meshing regions

Figure 4.5: (a) Simulated model overview and (b) meshing regions. The vacuum volumes in (a) are not shown. Coarse mesh size is used for the metal (3), and the vacuum regions (2 and 4). The finely meshed regions are the initial part of the beampipe (1), the radiator (6) and the vacuum above the radiator (5). For reference see Section 3.4.3.

necessary to adapt the radiator installation angle to the exact value of the radiator dielectric constant; secondly, although the dielectric constant has a frequency dependence, it is typically low enough that it would not affect the emission angle of the different spectral components. This approximation is justified up to approximately 100 GHz, but it is not necessarily true at higher frequencies where ϵ_r can drastically change [126].

4.5 Radiator orthogonal to the beampipe

Other than the nominal Cherenkov angle, an AWAKE ChDR BPM could also use radiators orthogonal to the beam propagation direction. Although such a design could be simpler to construct, it would potentially lead to internal reflections of the emitted wavefronts that must considered.

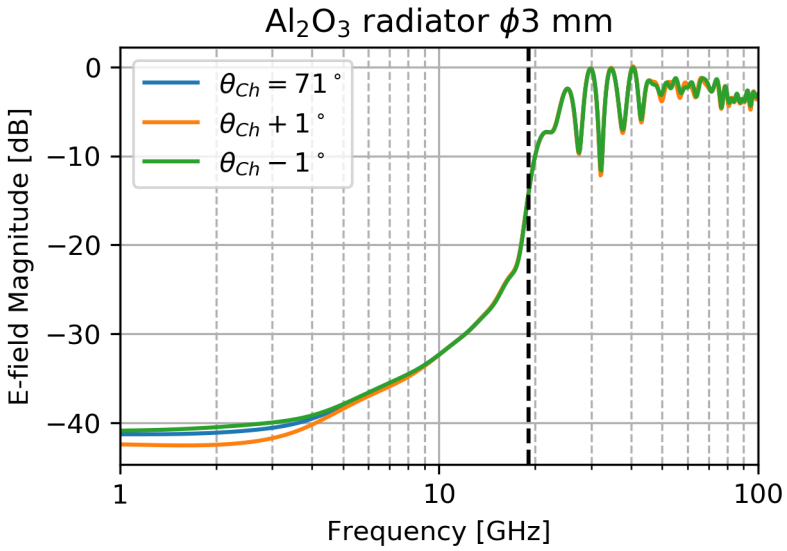

Figure 4.6: Electric field 1 cm away from the radiator output surface versus frequency. The results for a radiator orientation at $71 \pm 1°$ are shown. The dashed black line marks the theoretical cutoff frequency of 19.1 GHz.

4.5.1 Simulation

A 3D electromagnetic simulation model was developed similar to the one with radiators oriented at the Cherenkov angle described in Section 4.4. A vertical radiator with a 7 mm average length and a 3 mm diameter was placed in a metal beampipe. Again, a regional meshing approach was used. Figure 4.7 (a) shows the simulated 3D model and how it was divided into the different meshing regions. The finely-meshed regions 1, 5 and 6 used 20 mesh cells per wavelength. A 100 pC 2 ps-long electron bunch was used as a source. Figure 4.7 (b) shows the computed electric field on the longitudinal-cut plane.

The substantially different field-propagation evolution in a radiator not oriented at the Cherenkov angle is illustrated in Fig. 4.8, showing the radiator and the surrounding vacuum. In (a) and (b), the bunch has just passed the radiator surface, and several wavefronts are visible in the radiator. When the radiation reaches the output surface in (c), the first fronts are emitted towards the right, while the subsequent fronts in (d) propagate towards the left. Additionally, some wavefronts in (e) are internally reflected inside the radiator and in (f) propagate back to the beampipe. These results suggest that, for long radiators, different wavefronts may interfere with each other which could lead to a different spectrum of emission from the radiator compared

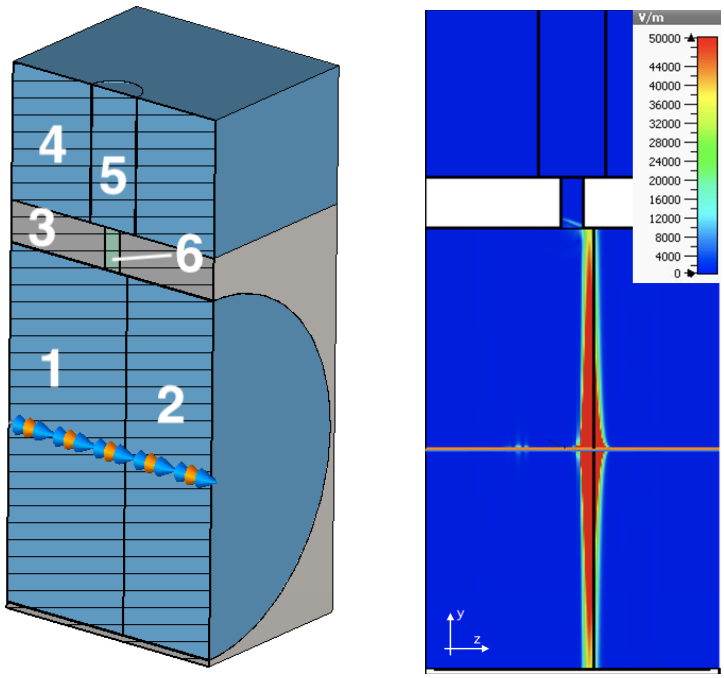

(a) (b)

Figure 4.7: (a) Simulated model with the meshing regions indicated and (b) the absolute value of the electric field in the transverse plane. Minimum resolution is used for the metal (3), and the vacuum regions (2 and 4). The high quality meshing regions are the initial part of the beampipe (1), the radiator (6) and the vacuum above the radiator (5). See for reference Section 3.4.3. The simulation was produced with a bandwidth of 100 GHz, and a 100 pC and 2 ps-long electron beam.

with the radiator installed at the nominal Cherenkov angle.

The beam position sensitivity of the two designs was compared by considering the absolute value of the electric field in the time domain computed for a probe at the centre of the output face using methods described in Section 3.3.3. The beam-position sensitivity over a 6 mm range is shown in Fig. 4.9. No appreciable difference can be observed.

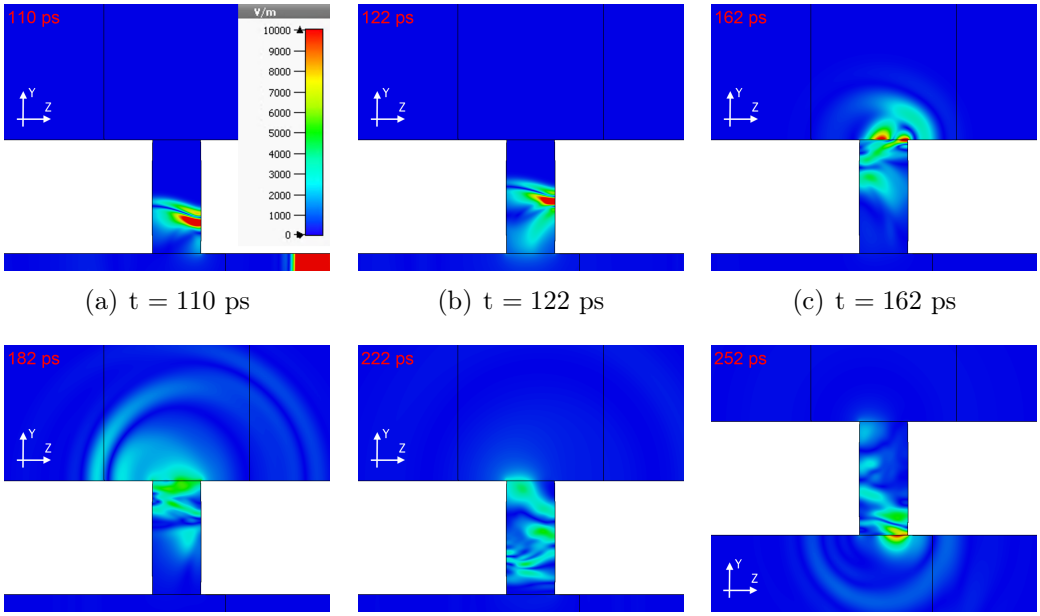

(a) t = 110 ps (b) t = 122 ps (c) t = 162 ps

(d) t = 182 ps (e) t = 222 ps (f) t = 252 ps

Figure 4.8: Absolute value of the electric field in the radiator and in the vacuum outside the vacuum pipe (on top). The field is displayed at different times. The internal reflection of the wavefronts can be seen in (b) and (c). At the exit of the radiator, two fronts propagating in different directions are visible in (d). Due to the medium change, a part of the radiation is also sent backwards to the beampipe as shown in (f).

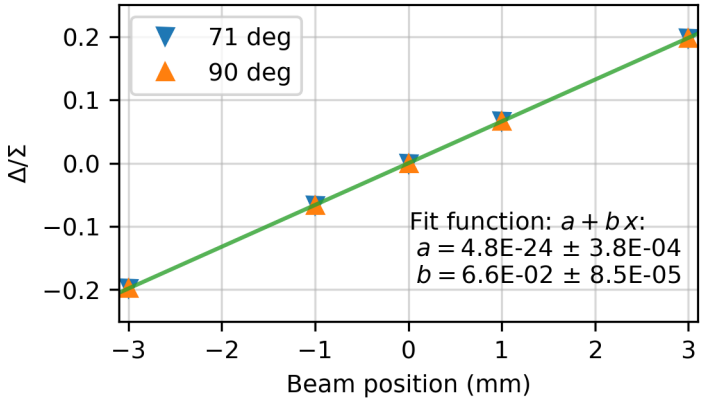

Figure 4.9: Comparison of the beam position sensitivity of radiators oriented at 71 and 90 degrees. The green line shows the linear fit, which exhibit the same response for both the orientations.

4.5.2 Experience with orthogonal waveguide coupling

The CLEAR facility is equipped with a device that is conceptually similar to an orthogonal ChDR pickup. Although this device was built with a different purpose and without considering the ChDR emission, it is instructive to consider the signal produced by such a device.

The BPRW [127] is an RF pickup that consist of a standard WR28 (Ka band) rectangular waveguide connected orthogonally to the beampipe. A vacuum tight connection between the vacuum pipe and the waveguide is obtained using an alumina window. This device was designed to perform a relative measurement of the bunch compression in the CTF3 facility [128] by producing a signal proportional to the bunch length [129]. The BPRW uses the fact that the high-frequency components of a shorter bunch are more intense than those of a longer bunch and therefore couple out more strongly through the waveguide.

Based on current understanding of Cherenkov Diffraction Radiation, it can be assumed that a ChDR front is produced in the BPRW alumina window when a beam passes in its proximity. Besides the ChDR front, there are also a number of DR fronts due to the electromagnetic discontinuities. To study the signals produced by the BPRW, the Ka-band RF detection system previously used to measure the beam-position sensitivity of the ChDR test device in the horizontal plane was employed. One of the diodes was left in place on the test device to detect its ChDR emission, while the other one was installed at the BPRW port after a short waveguide which provided some physical distance between the diode and the beam to avoid any radiation damage. The same attenuation of 30 dB was used in both cases. Figure 4.10 shows the BPRW port with one of the Ka-band detectors installed.

The signals from the BPRW and the ChDR test device are compared in Fig 4.11. The signals are arbitrarily scaled, as their ratio depends on a number of factors such as the beam position along the beamline, the signal-transmission efficiency and the alignment of the devices. It is nevertheless evident that the signals produced by the ChDR and the BPRW are different. The pulse produced by the ChDR test device is significantly shorter. Therefore, it can be speculated that the BPRW is not suitable for measurements of bunch trains. The allocated experimental beam time was not sufficient to test if a correlation between the BPRW signal and the beam position exists.

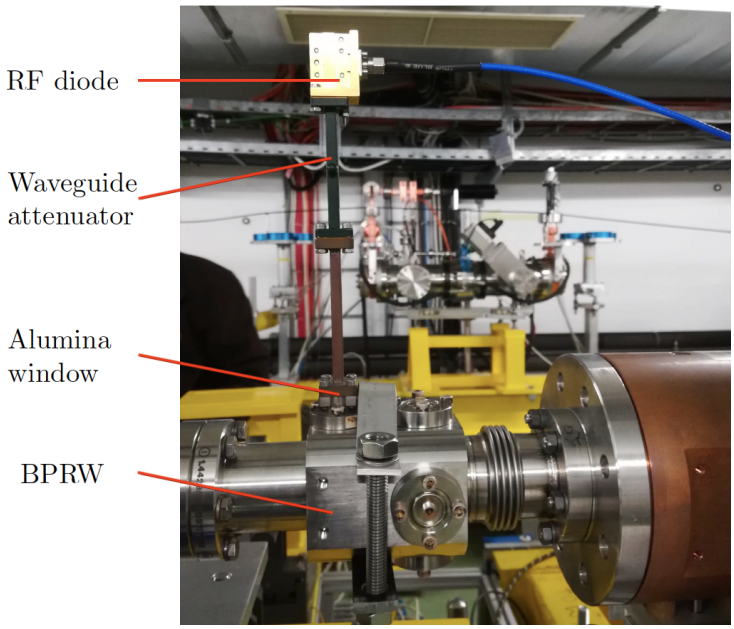

Figure 4.10: Diode detector installed on a BPRW port. In order from the beampipe: the alumina window assembly is the grey metallic part, then a copper waveguide straight section, a green 30 dB waveguide attenuator and the Schottky diode detector.

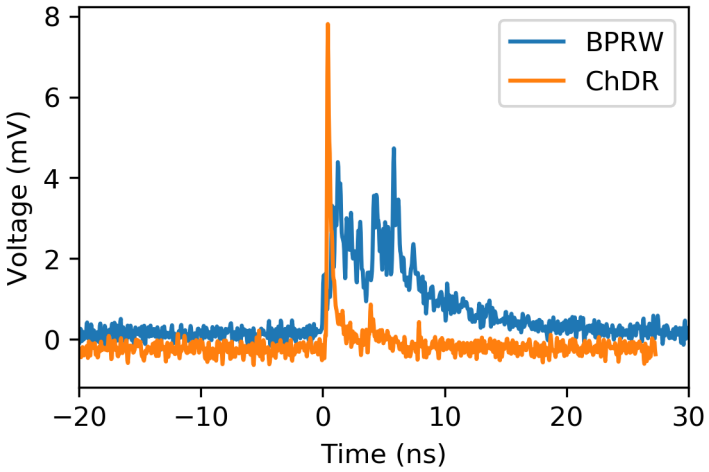

Figure 4.11: Diode detector output voltage for a BPRW and a ChDR radiator. The signals are arbitrarily scaled. The figure shows the different length of the two signals.

4.6 Future developments for ChDR BPMs

The ChDR emission is a very promising novel technique for beam position measurements. However, realising a vacuum-compatible device poses a number

of engineering challenges. In particular, the use of high permittivity materials results in radiators with diameters of the order of a few millimetres making the mechanical design challenging.

A preliminary vacuum-tight design is illustrated in Fig. 4.12. The radiator is inserted in a metal cylinder featuring a standard vacuum flange to be fixed to the BPM body. The radiator's beam-facing surface is flush with the beampipe. The radiator air-side surface is flat and orthogonal to the radiator axis. To assure vacuum tightness the radiator is brazed with a metal collar close to the output surface. The collar can then be welded to the metal housing.

A transition piece attached to the radiator output surface has to be designed to couple the device to a standard waveguide connected to a detection system operating at the desired frequency.

Extensive additional work is necessary to assess the impact of the internal reflections on the produced signals. Electromagnetic simulations can be improved using resistive metals and dispersive dielectrics in place of perfect materials. Some optimisation of the developed simulation models may be necessary to estimate the absolute power levels generated by the radiator.

4.7 The AWAKE ChDR BPM system

The present BPM layout in the AWAKE beamline is shown in Fig. 4.13 alongside a modified version with three ChDR BPMs installed. After the proposed modifications, the AWAKE beamline has to maintain an independent proton BPM system (pBPM) to measure the proton beam trajectory from the extraction in the SPS to the beam dump after the plasma cell. The existing electron

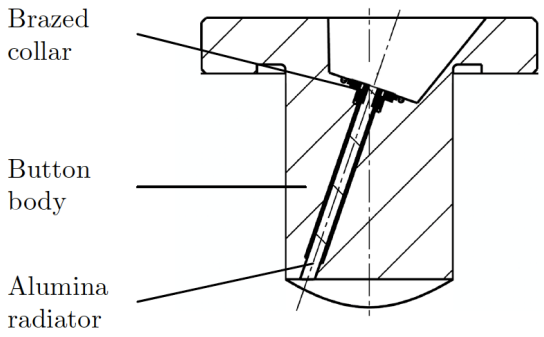

Figure 4.12: A preliminary design of a vacuum-tight dielectric insert for a ChDR BPM.

BPM system (eBPM) is also proposed to be maintained to measure the electron beam trajectory when no proton beam is present. The ChDR BPMs are added to measure the electron beam position when the proton beam is also present and their impact on the other systems should be minimised. Such integration is challenging due to the limited beamline space available in AWAKE. The AWAKE ChDR BPM mechanical design must take into account the beamline integration constraints. Moreover, the RF front-end and acquisition electronics would also need to be developed from scratch in order to deliver an operational system.

Two ChDR BPMs are foreseen for the common beamline, before the plasma cell. They are installed at the largest distance apart possible to increase the electron beam pointing resolution in the plasma cell. The first BPM is placed immediately after the merging point of the electron and proton beamlines. The second BPM replaces the standard pBPM closest to the plasma cell. The BPM conversion could be achieved by replacing the electrostatic buttons into ChDR buttons (See items number 1 and 3 in Fig. 4.13) if the ChDR buttons are designed to fit the existing pBPM body.

To retain the total number of pBPMs in the common beamline, the adjacent eBPM could be converted to measure both the proton and the electron beams (See item number 2 in Fig. 4.13), e.g. by splitting the eBPM output signal, sending the output signal to the eBPM electronics (to measure the electron position in absence of protons) and to the pBPM electronics that belonged to the converted pBPM (item 1 in Fig. 4.13). Such a modification may require some additional analogue signal conditioning. However, while this approach maintains the total number of proton BPM, it also reduces the resolution of the split eBPM, the impact of which has to be estimated.

One of the main design challenges described in Chapter 2 is the apparent non-reproducibility of the proton beam spectrum leading to shot-by-shot variations in the ratio of proton and electron bunch powers. As the streak camera measurements were not conclusive, additional measurements are necessary to estimate the the real proton beam spectrum. If the proton beam power in the ChDR BPMs detection band is significant compared to the electron beam power, and it is fluctuating shot-by-shot, it could be measured by using a dedicated device (item 4 in Fig. 4.13). This device, installed in the proton beamline, is a ChDR BPM in which the the four electrodes signals are used to estimate the proton bunch power in the detection band. To be independent from the beam position, the four signals can be summed. Such an approach is

commonly used in longitudinal profile monitors.

The described setup would make it possible to reconstruct the electron beam position in presence of a more intense proton beam. In case of an excessive proton beam signal fluctuation in the ChDR BPM detection band, the whole instrumentation pool can be used to correct the measurements for the proton beam position. However, the necessity for such correction has to be assessed with measurements once the proton beam is available during the next run.

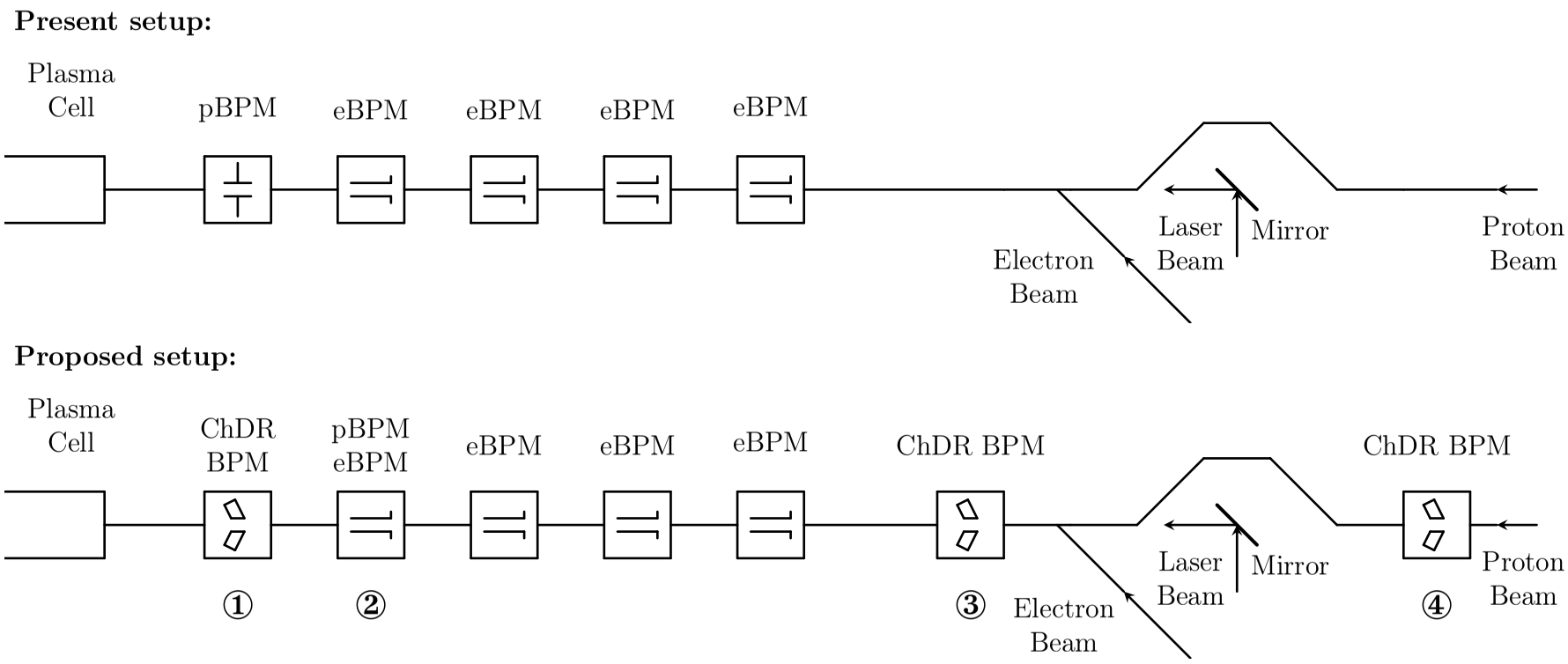

Figure 4.13: Layout of the present AWAKE BPM systems and the proposed modifications. The proton BPMs (pBPM) are electrostatic buttons, the electron BPMs (eBPM) are shorted striplines. The proposed modifications are: ①: convert the pBPM into a ChDR BPM, ②: use the eBPM to measure also the proton position by splitting its signal, ③: install a new ChDR BPM in a drift space, ④: install a ChDR BPM in the proton beamline to measure the proton beam power in the ChDR BPM detection band.

Chapter 5

Conclusions

Beam-driven novel acceleration schemes exploit various mechanisms to transfer the energy stored in a drive beam to accelerate a witness beam. The common denominator of these schemes is the large intensity difference between both beams, allowing the witness beam to be accelerated to a higher energy than that of the drive beam. Chapter 2 described a beam-diagnostics technique for a witness beam with bunches much shorter than those of the drive beam. This technique could be applied in the AWAKE experiment where a proton driver beam stores a large amount of energy used to accelerate an electron witness beam.

A proton-based electron-beam acceleration was demonstrated during the so-called AWAKE Run 1. The ultimate future goal of the AWAKE experiment is the production of beams for particle-physics research, requiring very precise control of beam energy and brilliance and repeatability of operational conditions. The concept is often referred in the the plasma-acceleration community as "moving from acceleration to accelerators".

For AWAKE Run 2, which aims to demonstrate emittance preservation of the accelerated beam, correct pointing of the electron beam in the plasma is crucial to control the acceleration process. The work documented in this thesis shows that this is possible but it requires a Beam Position Monitor working at frequencies of the order of tens of GHz.

This thesis work explored the possibility to build a high-frequency Beam Position Monitor based on the emission of ChDR from dielectric inserts in the beampipe. The produced signal can then be used to reconstruct the beam position. Beyond PWFA and beam-driven dielectric accelerators, the technique could be applied in any accelerator using short bunches, e.g. Free-Electron

Lasers.

Chapter 3 describes using the ChDR for beam position monitoring together with the simulations and the test results of a prototype monitor with PTFE radiators at the CLEAR facility at CERN. It was experimentally demonstrated that a beam position monitoring system working in the Ka-band can be realised. Due to its proof-of-principle nature, the prototype performance was limited and the produced radiation was detected in air using already available components. Nevertheless, those first tests proved that measuring the position of both single bunches and bunch trains is possible. The device was the first of its kind to integrate the radiators in the beampipe. Electromagnetic simulation demonstrated the importance of the diffraction radiation produced by the beampipe discontinuities.

A second test campaign was carried out with an improved narrow-band detection system to study in detail the prototype's response to beam position and charge variations. The ChDR emission was measured with a beam charge as low as 2 pC, despite the large attenuation of the transmission line. The results showed that ChDR is a valid tool for particle-beam diagnostics. Furthermore, the conducted experiments allowed experience with RF Schottky diode detectors and their use in the transient regime to be gained.

To use the ChDR BPM technology in an operational accelerator, a vacuum-tight monitor has to be developed. A preliminary design and simulations are presented in Chapter 4. Further steps required to fully develop a high-frequency BPM technology for short-bunch application are described in Section 4.6. For the specific case of AWAKE, where two particle beams are used, a BPM system architecture is proposed in Section 4.7. The installation of a vacuum-compatible prototype is foreseen in 2021.

Bibliography

[1] Paul Langacker. *The Standard Model and Beyond*. 2nd ed. Series in High Energy Physics, Cosmology and Gravitation. CRC Press, 2018. ISBN: 9781498763219.

[2] R. Aaij et al. "Observation of structure in the J/ψ-pair mass spectrum". preprint arXiv:2006.16957 (2020).

[3] R. Aaij et al. "Observation of $J/\psi p$ Resonances Consistent with Pentaquark States in $\Lambda_b^0 \to J/\psi K^- p$ Decays". In: *Phys. Rev. Lett.* 115 (2015), p. 072001.

[4] R. Aaij et al. "Observation of a Narrow Pentaquark State, $P_c(4312)^+$, and of the Two-Peak Structure of the $P_c(4450)^+$". In: *Phys. Rev. Lett.* 122 (2019), p. 222001.

[5] Peter W. Higgs. "Broken Symmetries and the Masses of Gauge Bosons". In: *Phys. Rev. Lett.* 13 (1964), pp. 508–509.

[6] Thomas Sven Pettersson and P Lefèvre. *The Large Hadron Collider: conceptual design*. Tech. rep. CERN-AC-95-05-LHC. 1995.

[7] Georges Aad et al. "Observation of a new particle in the search for the Standard Model Higgs boson with the ATLAS detector at the LHC". In: *Phys. Lett. B* 716 (2012).

[8] Serguei Chatrchyan et al. "Observation of a New Boson at a Mass of 125 GeV with the CMS Experiment at the LHC". In: *Phys. Lett. B* 716 (2012).

[9] Takaaki Kajita. "Nobel Lecture: Discovery of atmospheric neutrino oscillations". In: *Rev. Mod. Phys.* 88.3 (2016), p. 030501.

[10] P. J. E. Peebles and B. Ratra. "The cosmological constant and dark energy". In: *Rev. Mod. Phys.* 75 (2003).

[11] M. Casolino et al. “The JEM-EUSO instrument”. In: *Exper. Astron.* 40 (2015).

[12] A. Aab et al. “The Pierre Auger Cosmic Ray Observatory”. In: *Nucl. Instrum. Meth. A* 798 (2015).

[13] A. W. Chao, K. H. Mess, M. Tigner, et al. *Handbook of accelerator physics and engineering; 2nd ed.* Singapore: World Scientific, 2013.

[14] Massimo Ferrario. *Conventional Accelerators and their limits*. contribution to the CAS - CERN Accelerator School: High-Gradient Wakefield Accelerators, Sesimbra, Portugal, 11 - 22 March 2019, in preparation. preprint arXiv:2007.04075.

[15] Ralph Assman. *Beam propagation*. contribution to the CAS - CERN Accelerator School: High-Gradient Wakefield Accelerators, Sesimbra, Portugal, 11 - 22 March 2019, in preparation.

[16] G. Apollinari, I. Béjar Alonso, O. Brüning, et al. *High-Luminosity Large Hadron Collider (HL-LHC): Technical Design Report V. 0.1*. Tech. rep. CERN-2017-007-M. Geneva, 2017.

[17] L. Rossi and O.S. Brüning. “Progress with the High Luminosity LHC Project at CERN”. In: *Proc. 10th International Partile Accelerator Conference (IPAC’19), Melbourne, Australia, 19-24 May 2019*, paper MOYPLM3.

[18] A. Abada et al. “HE-LHC: The High-Energy Large Hadron Collider”. In: *Eur. Phys. J. ST* 228 (2019).

[19] A. Abada et al. “FCC-hh: The Hadron Collider”. In: *Eur. Phys. J. ST* 228 (2019).

[20] Klaus Wille. “Synchrotron Radiation”. Lecture series at Joint Universities Accelerator School (JUAS), in Archamps, France, unpublished. 2013.

[21] Peter D. Johnson. “2 - Synchrotron Radiation”. In: *Atomic, Molecular, and Optical Physics: Electromagnetic Radiation*. Vol. 29. Experimental Methods in the Physical Sciences. Academic Press, 1997.

[22] Carlo Wyss. *LEP design report, v.3: LEP2*. Tech. rep. CERN-AC-96-01-LEP-2. Geneva, 1996.

[23] Carlo Rubbia. “Further searches of the Higgs scalar sector at the ESS”. preprint arXiv:1908.05664. (2019).

[24] M-H. Wang, Y. Nosochkov, Y. Cai, et al. “Design of a 6 TeV muon collider”. In: *Journal of Instrumentation* 11 (2016).

[25] M. Bonesini. “Progress of the MICE experiment at RAL”. In: *Proceedings of the Neutrino Oscillation Workshop* (2013).

[26] M. Antonelli, M. Boscolo, R. Di Nardo, et al. “Novel proposal for a low emittance muon beam using positron beam on target”. In: *Nucl. Instrum. Meth. A* 807 (2016).

[27] A. Abada et al. “FCC-ee: The Lepton Collider”. In: *Eur. Phys. J. ST* 228 (2019).

[28] G. Aarons et al. *ILC Reference Design Report Volume 1 - Executive Summary*. Tech. rep. FERMILAB-PUB-07-794-E. 2007.

[29] M. Aicheler, P. Burrows, M. Draper, et al. *A Multi-TeV Linear Collider Based on CLIC Technology: CLIC Conceptual Design Report*. Tech. rep. CERN-2012-007. Geneva, 2012.

[30] W. D. Kilpatrick. “Criterion for Vacuum Sparking Designed to Include Both rf and dc”. In: *Review of Scientific Instruments* 28 (1957).

[31] V. Lebedev, A. Burov, and S. Nagaitsev. “Luminosity Limitations of Linear Colliders Based on Plasma Acceleration”. In: *Reviews of Accelerator Science and Technology* 09 (2016).

[32] I. Blumenfeld et al. “Energy doubling of 42 GeV electrons in a metre-scale plasma wakefield accelerator”. In: *Nature* 445 (2007).

[33] J. Osborne, A. Tudora and B. Swatton. “Tunneling for physics”. In: *CERN Courier* 59 (2019).

[34] Thomas P Wangler. *RF linear accelerators; 2nd rev. version*. Physics textbook. Weinheim: Wiley, 2008.

[35] D.B. Hopkins, A.M. Sessler, and J.S. Wurtele. “The two-beam accelerator”. In: *Nucl. Instr. and Meth. A: Accelerators, Spectrometers, Detectors and Associated Equipment* 228 (1984).

[36] Roberto Corsini. “Final Results From the Clic Test Facility (CTF3)”. In: *Proc., 8th International Particle Accelerator Conference (IPAC 2017): Copenhagen, Denmark, May 14-19, 2017, paper TUZB1*. 2017.

[37] T. Argyropoulos, N. Catalan-Lasheras, A. Grudiev, et al. "Design, fabrication, and high-gradient testing of an X-band, traveling-wave accelerating structure milled from copper halves". In: *Phys. Rev. Accel. Beams* 21 (2018).

[38] A. D. Cahill, J. B. Rosenzweig, V. A. Dolgashev, et al. "High gradient experiments with X-band cryogenic copper accelerating cavities". In: *Phys. Rev. Accel. Beams* 21 (2018).

[39] W. Gai, P. Schoessow, B. Cole, et al. "Experimental Demonstration of Wake-Field Effects in Dielectric Structures". In: *Phys. Rev. Lett.* 61 (1988).

[40] R. J. England, R. J. Noble, K. Bane, et al. "Dielectric laser accelerators". In: *Rev. Mod. Phys.* 86 (2014).

[41] E. A. Peralta et al. "Demonstration of electron acceleration in a laser-driven dielectric microstructure". In: *Nature* 503 (2013).

[42] B. O'Shea, G. Andonian, S. Barber, et al. "Observation of acceleration and deceleration in gigaelectron-volt-per-metre gradient dielectric wakefield accelerators". In: *Nature communications* 7 (2016).

[43] T. Tajima and J. M. Dawson. "Laser Electron Accelerator". In: *Phys. Rev. Lett.* 43 (1979).

[44] P. Chen, J. M. Dawson, R. W. Huff, et al. "Acceleration of Electrons by the Interaction of a Bunched Electron Beam With a Plasma". In: *Phys. Rev. Lett.* 54 (1985).

[45] S. P. D. Mangles et al. "Monoenergetic beams of relativistic electrons from intense laser-plasma interactions". In: *Nature* 431 (2004).

[46] J. Faure, Y. Glinec, A. Pukhov, et al. "A laser-plasma accelerator producing monoenergetic electron beams". In: *Nature* 431 (2004).

[47] M. Litos et al. "High-efficiency acceleration of an electron beam in a plasma wakefield accelerator". In: *Nature* 515 (2014).

[48] P. Muggli. *Beam-driven, Plasma-based Particle Accelerators*. contribution to the CAS - CERN Accelerator School: Plasma Wake Acceleration, CERN, Geneva, Switzerland, 23 - 29 Nov 2014 arXiv:1705.10537. 2017.

[49] W. Lu, C. Huang, M. M. Zhou, et al. "Limits of linear plasma wakefield theory for electron or positron beams". In: *Physics of Plasmas* 12 (2005).

[50] R.D. Ruth and Pisin Chen. "Plasma Accelerators". In: *13th SLAC Summer Institute on Particle Physics: Supersymmetry (Topical Conference last 3 days) (SSI 85) SLAC-PUB-3906*. 1986.

[51] E. Adli et al. "Acceleration of electrons in the plasma wakefield of a proton bunch". In: *Nature* 561 (2018).

[52] E. Esarey, C. B. Schroeder, and W. P. Leemans. "Physics of laser-driven plasma-based electron accelerators". In: *Rev. Mod. Phys.* 81 (2009).

[53] V. Malka, S. Fritzler, E. Lefebvre, et al. "Electron Acceleration by a Wake Field Forced by an Intense Ultrashort Laser Pulse". In: *Science* 298 (2002).

[54] B. Allen, V. Yakimenko, M. Babzien, et al. "Experimental Study of Current Filamentation Instability". In: *Phys. Rev. Lett.* 109 (2012).

[55] C. Bracco, B. Goddard, E. Gschwendtner, et al. "The Challenge of Interfacing the Primary Beam Lines for the AWAKE Project at CERN". In: *Proc., 5th International Particle Accelerator Conference (IPAC 2014): Dresden, Germany, June 15-20, 2014*.

[56] K. Elsener. *The CERN neutrino beam to Gran Sasso: General description of the CERN project for a neutrino beam to Gran Sasso (CNGS). Description générale du projet de faisceau de neutrinos du CERN vers le Gran Sasso (CNGS)*. Tech. rep. CERN-AC-Note-2000-03. Geneva: CERN, 2000.

[57] H. Damerau, A. Funken, R. Garoby, et al. *LHC Injectors Upgrade, Technical Design Report*. Tech. rep. CERN-ACC-2014-0337. 2014.

[58] Esma Mobs. CERN accelerator complex layout, OPEN-PHO-ACCEL-2018-005-1.

[59] Valentin Fedosseev et al. "Integration of a Terawatt Laser at the CERN SPS Beam for the AWAKE Experiment on Proton-Driven Plasma Wake Acceleration". In: *Proc., 7th International Particle Accelerator Conference (IPAC 2016): Busan, Korea, May 8-13, 2016*, paper WEPMY020.

[60] K. Pepitone et al. "The electron accelerators for the AWAKE experiment at CERN - Baseline and future developments". In: *Nucl. Instrum. Meth.* A 909 (2018).

[61] S. Y. Kim, S. Doebert, O. Apsimon, et al. "Commissioning of the electron injector for the AWAKE experiment". In: *Nucl. Instrum. Methods Phys. Res., A* 953 (2020).

[62] G. Plyushchev, R. Kersevan, A. Petrenko, et al. "A Rubidium Vapor Source for a Plasma Source for AWAKE". In: *J. Phys.* D 51 (2018).

[63] Patric Muggli. "AWAKE results on Self-modulation, Acceleration, Hosing and Future plans". Oral presentation in the AAC seminar series. 2020.

[64] K. V. Lotov. "Physics of beam self-modulation in plasma wakefield accelerators". In: *Physics of Plasmas* 22 (2015).

[65] N. Kumar, A. Pukhov, and K. Lotov. "Self-Modulation Instability of a Long Proton Bunch in Plasmas". In: *Phys. Rev. Lett.* 104 (2010).

[66] E. Adli et al. "Experimental Observation of Proton Bunch Modulation in a Plasma at Varying Plasma Densities". In: *Phys. Rev. Lett.* 122 (2019).

[67] S. Mazzoni et al. "Beam Instrumentation Developments for the Advanced Proton Driven Plasma Wakefield Acceleration Experiment at CERN". In: *Proc., 8th International Particle Accelerator Conference (IPAC 2017): Copenhagen, Denmark, May 14-19, 2017*, paper MOPAB119.

[68] I. Gorgisyan, C. Bracco, S. Burger, et al. "Commissioning of Beam Instrumentation at the CERN AWAKE Facility After Integration of the Electron Beam Line". In: *J. Phys. : Conf. Ser.* 1067 (2018), paper WEPAF070.

[69] C. Behrens, C. Gerth, G. Kube, et al. "Inorganic Scintillators for Particle Beam Profile Diagnostics of Highly Brilliant and Highly Energetic Electron Beams". In: *Conf. Proc. C* 1205201 (2012).

[70] C. P. Welsch, E. Bravin, and T. Lefevre. "Investigations of OTR screen surfaces and shapes". In: *Conf. Proc. C* 060626 (2006).

[71] M. Barros Marin, A. Boccardi, T. Bogey, et al. "Performance of the AWAKE Proton Beam Line Beam Position Measurement System at CERN". In: *Proc., 6th International Beam Instrumentation Conference, IBIC2017*. 2018, paper TUPCF06.

[72] S. Liu, V. Verzilov, W. Farabolini, et al. "Development of the AWAKE Stripline BPM Electronics". In: *Proceedings of International Conference on Technology and Instrumentation in Particle Physics 2017*. Springer Singapore, 2018.

[73] S. Liu, P. Dirksen, S. Gessner, et al. "The Installation and Commissioning of the AWAKE Stripline BPM". In: *Proc., 7th International Beam Instrumentation Conference (IBIC 2018): Shanghai, Cina, September 9-13, 2018*, paper TUPB01.

[74] John David Jackson. *Classical electrodynamics; 3rd ed.* New York, NY: Wiley, 1999.

[75] Robert E. Shafer. "Beam position monitoring". In: *AIP Conference Proceedings* 249 (1992).

[76] P. Forck, P. Kowina, and D. Liakin. *Beam position monitors.* contribution to the CAS - Course of beam diagnostics, Dourdan, France, 28 May - 6 June 2008.

[77] Y. Papaphilippou, H. Bartosik, G. Rumolo, et al. *Operational Beams for the LHC.* Tech. rep. CERN-2015-002.80. 2015.

[78] H. Timko, T. Argyropoulos, H. Bartosik, et al. "Short High-Intensity Bunches for Plasma Wakefield Experiment AWAKE in the CERN SPS". In: *Proc., 4th International Particle Accelerator Conference (IPAC 2013), Shanghai, China, 12 - 17 May 2013, pp.1820.*

[79] G. Papotti and F.M. Velotti. Private communication. February 2019.

[80] T. Bohl and J. F. Malo. *The APWL Wideband Wall Current Monitor.* Tech. rep. CERN-BE-2009-006. 2009.

[81] V. L. Ginzburg and V. N. Tsytovich. *Transition radiation and transition scattering. Perekhodnoe izluchenie i perekhodnoe rasseianie.* Adam Hilger series on plasma physics. 1990.

[82] A.-M. Bachmann and P. Muggli. "Determination of the Charge per Micro-Bunch of a Self-Modulated Proton Bunch using a Streak Camera". In: *EAAC2019 Conference Proceedings: La Biodola, Elba, Italy.* 2019.

[83] V. Wlotzko, W. Uhring, and P. Summ. "Impact of laser phase and amplitude noises on streak camera temporal resolution". In: *Review of Scientific Instruments* 86 (2015).

[84] Hamamtsu photonics, Streak Camera model C10910-05, 16-bit, 2048 x2048 pixel ORCA-Flash4.0 CMOS sensor, binned to 512 x 512 pixels for streak operation. URL: `https://www.hamamatsu.com/jp/en/product/type/C10910-05`.

[85] Steven Smith. *The Scientist and Engineer's Guide to Digital Signal Processing*.

[86] Courtesy of Dr. S. Mazzoni (CERN), measurement data from 1.11.2019.

[87] A. Angelovski, A. Kuhl, M. Hansli, et al. "High bandwidth pickup design for bunch arrival-time monitors for free-electron laser". In: *Phys. Rev. ST Accel. Beams* 15 (2012).

[88] Alves, D. and others. "Cherenkov Diffraction Radiation as a tool for beam diagnostics". In: *Proc., 8th International Beam Instrumentation Conference (IBIC2019): Malmo, Sweden, Sep 8-12, 2019*. 2019, paper THAO01.

[89] A. Curcio, M. Bergamaschi, R. Corsini, et al. "Noninvasive bunch length measurements exploiting Cherenkov diffraction radiation". In: *Phys. Rev. Accel. Beams* 23 (2020).

[90] P. A. Čerenkov. "Visible Radiation Produced by Electrons Moving in a Medium with Velocities Exceeding that of Light". In: *Phys. Rev.* 52 (1937).

[91] I. Tamm. "Radiation emitted by uniformly moving electrons". In: *J. Phys. (USSR)* 1 (1939).

[92] William R Leo. *Techniques for nuclear and particle physics experiments: a how-to approach; 2nd ed.* Berlin: Springer, 1994.

[93] Takaaki Kajita. "Nobel Lecture: Discovery of atmospheric neutrino oscillations". In: *Rev. Mod. Phys.* 88 (2016).

[94] A. Letessier-Selvon and T. Stanev. "Ultrahigh energy cosmic rays". In: *Rev. Mod. Phys.* 83 (2011).

[95] M. Bergamaschi, A. Aryshev, P. Karataev, et al. "Recent results using incoherent Cherenkov Diffraction Radiation for non-invasive beam diagnostics". In: *Proc., 10th International Particle Accelerator Conference (IPAC'19), Melbourne, Australia, May 19-24, 2019*. 2019, paper WEPGW077.

[96] A. M. Cook, R. Tikhoplav, S. Y. Tochitsky, et al. "Observation of Narrow-Band Terahertz Coherent Cherenkov Radiation from a Cylindrical Dielectric-Lined Waveguide". In: *Phys. Rev. Lett.* 103 (2009).

[97] A. Curcio, M. Bergamaschi, R. Corsini, et al. "Beam-based sub-THz source at the CERN linac electron accelerator for research facility". In: *Phys. Rev. Accel. Beams* 22 (2019).

[98] D.V. Karlovets and A.P. Potylitsyn. "Universal description for different types of polarization radiation". unpublished, arXiv 0908.2336. 2009.

[99] K.O. Kruchinin and D.V. Karlovets. "Development of the theory of diffraction radiation from surfaces with finite conductivity". In: *Russ. Phys. J* 55 (2012).

[100] M.V. Shevelev and A.S. Konkov. "Peculiarities of the generation of Vavilov-Cherenkov radiation induced by a charged particle moving past a dielectric target". In: *J. Exp. Theor. Phys.* 118 (2014).

[101] S. N. Galyamin and A. V. Tyukhtin. "Dielectric Concentrator for Cherenkov Radiation". In: *Phys. Rev. Lett.* 113 (2014).

[102] A.S. Konkov, J.S. Markova, A.P. Potylitsyn, et al. "Theoretical model for Incoherent Cherenkov Diffraction Radiation, Report II". Unpublished. 2018.

[103] Y. A. Brychkov. *Handbook of Special Functions: Derivatives, Integrals, Series and Other Formulas*. Hoboken, NJ: Taylor & Francis Ltd, 2008.

[104] H. Motz. "Applications of the Radiation from Fast Electron Beams". In: *Journal of Applied Physics* 22 (1951).

[105] Oliver Grimm and Peter Schmüser. *Principles of longitudinal beam diagnostics with coherent radiation*. Tech. rep. TESLA FEL 2006-03. 2006.

[106] CST Studio Suite, version 2018 and 2019. URL: `https://www.3ds.com/products-services/simulia/products/cst-studio-suite/`.

[107] M. Harrach. Private communication with the CST support. March 2019.

[108] R. A. Fonseca, L. O. Silva, F. S. Tsung, et al. "OSIRIS: A Three-Dimensional, Fully Relativistic Particle in Cell Code for Modeling Plasma Based Accelerators". In: *Computational Science — ICCS 2002*. Springer Berlin Heidelberg, 2002.

[109] A. Shishlo, S. Cousineau, J. Holmes, et al. "The Particle Accelerator Simulation Code PyORBIT". In: *Procedia Computer Science, ICCS 2015 conference* 51 (2015).

[110] A. D. Greenwood, K. L. Cartwright, J. W. Luginsland, et al. "On the elimination of numerical Cerenkov radiation in PIC simulations". In: *Journal of Computational Physics* 201 (2004).

[111] B. Goplen, L. Ludeking, D. Smith, et al. "User-configurable MAGIC for electromagnetic PIC calculations". In: *Computer Physics Communications* 87 (1995).

[112] N. Mounet, Impedance Wakefield 2D (IW2D) simulation code. URL: `https://twiki.cern.ch/twiki/bin/view/ABPComputing/ImpedanceWake2D`.

[113] Kyrre Sjobak et al. "Status of the CLEAR electron beam user facility at CERN". In: *Proc., 10th International Particle Accelerator Conference (IPAC2019): Melbourne, Australia, May 19-24, 2019*. 2019, paper MOPTS054.

[114] R. Corsini et al. "First Experiments at the CLEAR User Facility". In: *Proc., 9th International Particle Accelerator Conference (IPAC'18), Vancouver, BC, Canada, April 29-May 4, 2018*.

[115] Bergoz Integrating Current Transformer. URL: `https://gmw.com/product/ict/,%20Last%20Access:%2028%20April%202020`.

[116] GPIB protocol, IEEE 488 standard. See the industrial standard report IEC 60488. URL: `https://webstore.iec.ch/publication/2246`.

[117] LXI, LAN eXtension for instrumentation protocol. URL: `https://www.lxistandard.org/`.

[118] Agilent Technologies. *The Zero Bias Schottky Diode Detector at Temperature Extremes*. Application Note 1090.

[119] Millitech (now Smiths Interconnect). *General purpose DET detectors datasheet*. URL: `https://www.smithsinterconnect.com/SmithsInterconnect/files/e8/e841ad83-d6d6-4fc9-b7ea-f8d621aa684e.pdf`.

[120] Tom Levens et al. "Python tools for machine data analysis and equipment control". Unpublished. 2017.

[121] W. McKinney. "pandas: a foundational Python library for data analysis and statistics". In: *Python for High Performance and Scientific Computing* 14 (2011).

[122] A D'Elia, R Fandos, and L Søby. *High bandwidth wall current monitor*. Tech. rep. CERN-OPEN-2010-012. 2009.

[123] J. L. Rodgers and W. A. Nicewander. "Thirteen Ways to Look at the Correlation Coefficient". In: *The American Statistician* 42 (1988).

[124] Thibaut Lefevre. Private communication. November 2020.

[125] M. Tavlet and S. Ilie. *Behaviour of organic materials in radiation environment*. Tech. rep. CERN-TIS-TE-IR-99-08. 2000.

[126] M. N. Afsar and K. J. Button. "Precise Millimeter-Wave Measurements of Complex Refractive Index, Complex Dielectric Permittivity and Loss Tangent of GaAs, Si, SiO_2, $A1_2O_3$, BeO, Macor, and Glass". In: *IEEE Transactions on Microwave Theory and Techniques* 31.2 (1983).

[127] Anne Dabrowski et al. "Measuring the Longitudinal Bunch Profile at CTF3". In: *Proc., 25th International Linear Accelerator Conference, LINAC2010: Tsukuba, Japan, September 12-17, 2010*, paper TUP100.

[128] Günther Geschonke and A Ghigo. *CTF3 Design Report*. Tech. rep. CERN-PS-2002-008-RF. 2002.

[129] T. Lefevre. "The CLIC test facility 3 instrumentation". In: *Proc., 13th Beam Instrumentation Workshop, Tahoe City, California, USA, 4-8 May 2008*. 2008.